

**Analysis and Parametric Investigation of  
Active Open Cross Section  
Thin Wall Beams**

by

**James Griffiths, B.Eng.**

Carleton University

A thesis submitted to  
the Faculty of Graduate Studies and Research  
in partial fulfillment of  
the requirements for the degree of

**Master of Applied Science**

Ottawa-Carleton Institute for  
Mechanical and Aerospace Engineering

Department of  
Mechanical and Aerospace Engineering

Carleton University

Ottawa, Ontario

January 13, 2010

© Copyright

2010 - James Griffiths



Library and Archives  
Canada

Published Heritage  
Branch

395 Wellington Street  
Ottawa ON K1A 0N4  
Canada

Bibliothèque et  
Archives Canada

Direction du  
Patrimoine de l'édition

395, rue Wellington  
Ottawa ON K1A 0N4  
Canada

*Your file* *Votre référence*  
ISBN: 978-0-494-68627-0  
*Our file* *Notre référence*  
ISBN: 978-0-494-68627-0

**NOTICE:**

The author has granted a non-exclusive license allowing Library and Archives Canada to reproduce, publish, archive, preserve, conserve, communicate to the public by telecommunication or on the Internet, loan, distribute and sell theses worldwide, for commercial or non-commercial purposes, in microform, paper, electronic and/or any other formats.

The author retains copyright ownership and moral rights in this thesis. Neither the thesis nor substantial extracts from it may be printed or otherwise reproduced without the author's permission.

**AVIS:**

L'auteur a accordé une licence non exclusive permettant à la Bibliothèque et Archives Canada de reproduire, publier, archiver, sauvegarder, conserver, transmettre au public par télécommunication ou par l'Internet, prêter, distribuer et vendre des thèses partout dans le monde, à des fins commerciales ou autres, sur support microforme, papier, électronique et/ou autres formats.

L'auteur conserve la propriété du droit d'auteur et des droits moraux qui protègent cette thèse. Ni la thèse ni des extraits substantiels de celle-ci ne doivent être imprimés ou autrement reproduits sans son autorisation.

---

In compliance with the Canadian Privacy Act some supporting forms may have been removed from this thesis.

While these forms may be included in the document page count, their removal does not represent any loss of content from the thesis.

Conformément à la loi canadienne sur la protection de la vie privée, quelques formulaires secondaires ont été enlevés de cette thèse.

Bien que ces formulaires aient inclus dans la pagination, il n'y aura aucun contenu manquant.

  
**Canada**

Please note:

The acceptance form on page ii for this thesis has been removed. The removal of this information does not represent any loss of content from the thesis.

# Abstract

The static behaviour of active Open Cross Section Thin Wall Beams (OCSTWB) with embedded Active/Macro Fibre Composites (AFCs/MFCs) has been investigated for the purpose of advancing the fundamental theory needed in the development of advanced smart structures. An efficient code that can analyze active OCSTWB using analytical equations has been studied.

Various beam examples have been investigated in order to verify this recently developed analytical active OCSTWB analysis tool. The cross sectional stiffness constants and induced force, moments and bimoment predicted by this analytical code have been compared with those predicted by the 2-D finite element beam cross section analysis codes called the Variational Asymptotic Beam Sectional (VABS) analysis and the University of Michigan VABS (UM/VABS). Good agreement was observed between the results obtained from the analytical tool and VABS.

The calculated cross sectional stiffness constants and induced force/moments, the constitutive relation and the six intrinsic static equilibrium equations for OCSTWB were all used together in a first-order accurate forward difference scheme in order to determine the average twist and deflections along the beam span. In order to further verify the analytical code, the static behaviour of a number of beam examples was investigated using 3-D Finite Element Analysis (FEA). For a particular cross section, the rigid body twist and displacements were minimized with the displacements of all the nodes in the 3-D FEA model that compose the cross section. This was done for a number of cross sections along the beam span in order to recover the global beam twist and displacement profiles from the 3-D FEA results. The global twist and deflections predicted by the analytical code agreed closely with those predicted by UM/VABS and 3-D FEA.

The study was completed by a parametric investigation to determine the boundary conditions and the composite ply lay-ups of the active and passive plies that produce the greatest twist in an active I-beam spar using an induced bimoment. It was found that greater twist could be produced by distributing the active plies near the outer flange edges and towards the warping restrained beam root.

## Acknowledgements

I would like to thank my supervisor, Professor Fred F. Afagh for his support, guidance and encouragement. In particular, the generous amount of time he spent giving direction and feedback was highly valuable. I would also like to extend deep appreciation to my colleague, Dr. Fidel Khouli for his help and advice. His explanations on the underlying theory behind the active OCSTWB code he had developed, and suggestions and assistance in regards to verifying it were very useful.

Dr. Dewey H. Hodges of the School of Aerospace Engineering at the Georgia Institute of Technology, and Dr. Wenbin Yu of the Department of Mechanical and Aerospace Engineering at the University of Utah, both provided clarifications from their papers. I would also like to recognize the financial support from the Natural Sciences and Engineering Research Council (NSERC), which made this work possible.

# List of Abbreviations and Symbols

$(\cdot)$	Derivative with respect to (w.r.t.) $s$
$(\cdot)'$	Derivative w.r.t. $x_1$
$(\cdot)_{,1}$	Derivative w.r.t. $x_1$
$(\cdot)_{,2}$	Derivative w.r.t. $s$
$a$	Characteristic dimension of a beam cross section
$\aleph(E_1)$	Quadratic electromechanical field term
<i>AFC</i>	Active Fibre Composite
$b$	Half the width of an I-beam
$\mathbf{b}_i$	Local orthonormal undeformed unit vectors in the $x_i$ directions
$\mathbf{B}_i$	Local orthonormal deformed unit vectors in the $x_i$ directions
$\mathbf{C}$	Cross sectional stiffness matrix
$\check{\mathbf{C}}$	Stiffness matrix in the $x_{i-local}$ frame
$\mathbf{C}^{Bb}$	Rotation matrix that transforms the $\mathbf{b}_i$ basis to the $\mathbf{B}_i$ basis
$C_{ij}$	Cross sectional stiffness constants w.r.t. the $x_i$ coordinates
$\check{C}_{ij}$	Stiffness constants w.r.t. the $x_{i-local}$ coordinates
$D^{\alpha\beta\gamma\delta}$	Plane-stress reduced constants w.r.t. $x_1$ and $s$
$d_{kij}$	Electromechanical coupling tensor w.r.t. the $x_{i-local}$ coordinates
$\bar{d}_{kij}$	Electromechanical coupling tensor w.r.t. the $x_i$ coordinates
$\Delta x_1$	Node separation distance along the discretized beam reference line
$\epsilon$	Maximum strain in the beam
$\bar{\epsilon}$	Vector of the classical strain measures
$\eta$	Sectorial coordinate of a cross section
$E_{11}, E_{22}$	Young's moduli in the $x_{1-local}$ and $x_{2-local}$ directions, respectively
$\epsilon_{\alpha\beta}$	Total strain tensor of a shell w.r.t. the in-plane shell coordinates: $x_1$ and $s$

$\varepsilon_i^m$	Direct mechanical strain in the $x_{i-local}$ direction
$\varepsilon_{ij}^{(a)}$	Induced active strain tensor w.r.t. the $x_i$ coordinates
$\varepsilon_{ij}^{(a)}$	Induced active strain tensor w.r.t. the $x_{i-local}$ coordinates
$\varepsilon_{ij}^m$	Mechanical strain components w.r.t. the $x_i$ coordinates
$E^{ijkl}$	Elasticity, or Hookean tensor
$E_k$	Electric field in the $x_{i-local}$ direction
$\varepsilon_{kl}$	Total strain tensor
$F_1$	Axial extension force at the beam reference line in the $x_1$ direction
$F_i^{(a)}$	Active components of $F_i$
$F_2, F_3$	Transverse forces in the $x_2$ and $x_3$ directions, respectively
$FEA$	Finite Element Analysis
$g$	Half the height of an I-beam
$\gamma_{11}$	Extensional strain at the beam reference line in the $x_1$ direction
$G_{12}, G_{23}$	Orthotropic shear moduli w.r.t. the $x_{i-local}$ coordinates
$\gamma_{\alpha\beta}$	Strain measures corresponding to in-plane shell stretching
$\gamma_{ij}^m$	Mechanical shear strains w.r.t. the $x_{i-local}$ coordinates
$GT/VABS$	Georgia Institute of Technology VABS
$h$	Wall thickness
$\mathbf{H}, \mathbf{G}$	Laminate electromechanical matrices
$\kappa_1$	Twisting strain at the beam reference line about the $x_1$ axis
$\kappa_2, \kappa_3$	Curvature strains at the beam reference line about the $x_2$ and $x_3$ axes
$l$	Wavelength of elastic deformations
$L$	Beam length
$M_1$	Torsion about the $x_1$ axis
$M_i^{(a)}$	Active components of $M_i$
$M_2, M_3$	Bending moments about the $x_2$ and $x_3$ axes, respectively

$M_\omega$	Bimoment at the beam reference line
$M_\omega^{(a)}$	Active component of $M_\omega$
$MFC$	Macro Fibre Composite
$M_\omega^t$	Mechanical bimoment applied at a beam tip
$n$	Number of nodes along the discretized beam reference line
$\mathbf{n}$	Outward normal direction to the contour
$\nu_{12}, \nu_{23}$	Poisson's ratios w.r.t. the $x_{i-local}$ coordinates
$\omega$	Warping function
$OCSTWB$	Open Cross Section Thin Wall Beam
$\phi$	Vector of unknown shell strains
$\psi$	Vector of known shell strains
$\bar{\psi}, \bar{\phi}$	Vectors of the known and unknown $\mathcal{O}(\epsilon)$ strain terms, respectively
$\tilde{\psi}, \tilde{\phi}$	Vectors of the known and unknown $\mathcal{O}\left(\epsilon \left(\frac{a}{l}\right) \left(\frac{b}{a}\right)^{-1}\right)$ strain terms, respectively
$PZT$	Lead Zirconium Titanate
$\mathbf{Q}, \mathbf{S}, \mathbf{P}$	Laminate elastic matrices
$\mathbf{r}$	Vector from the origin of the $\mathbf{b}_i$ orthonormal triad to a point on the contour
$R$	Radius of curvature of the wall contour
$\rho_{\alpha\beta}$	Strain measures corresponding to shell bending/curvature
$r_n$	Component of $\mathbf{r}$ in the $\mathbf{n}$ direction
$r_\tau$	Component of $\mathbf{r}$ in the $\boldsymbol{\tau}$ direction
$\mathcal{R}(\vartheta)$	Rotation matrix that transforms the $x_{i-local}$ frame to the $x_i$ frame
$s$	Curvilinear contour coordinate
$\sigma_i$	Direct stress in the $x_{i-local}$ direction
$\sigma_{ij}$	Stress tensor
$S_{ij}$	Cross sectional flexibility constants w.r.t. the $x_i$ coordinates
$s_o$	Contour origin

$\sigma_{x_1}$	Applied stress in the $x_1$ direction
$\tau$	Contour direction
$\mathbf{T}$	Matrix that relates $\bar{\epsilon}$ to $\bar{\psi}$
$\tilde{\mathbf{T}}$	Matrix that relates $\bar{\epsilon}'$ to $\tilde{\psi}$
$t_{electrodes}$	Spacing between the interdigitated electrodes
$\theta$	Twist at the beam reference line about the $x_1$ axis
$\vartheta$	Angle from the $x_1$ axis to the $x_{1-local}$ axis
$\tau_{ij}$	Shear stresses w.r.t. the $x_{i-local}$ coordinates
$t_{ply}$	Ply thickness
$u_1, u_2, u_3$	Global displacements of the beam in the $x_i$ directions
$v_1, v_2, v_3$	Displacement of a contour point in the $x_1, s$ and $\xi$ directions, respectively
$\mathcal{U}^{(a)}$	Active component of $\mathcal{U}^{(m)}$
$\mathcal{U}_{Vlasov}^{(a)}$	Active Vlasov component of $\mathcal{U}_{refined}^{(m)}$
$\hat{u}_i$	Displacement of a contour point in the $x_i$ direction
$\mathcal{U}^{(m)}$	Strain energy density per unit length of $\mathcal{O}(\epsilon^2)$ accuracy
$\check{\mathcal{U}}^{(m)}$	Mechanical strain energy density per unit volume
$\hat{\mathcal{U}}^{(m)}$	Mechanical shell strain energy per unit volume
$\tilde{\mathcal{U}}^{(m)}$	Mechanical shell strain energy per unit length
$\mathcal{U}_{refined}^{(m)}$	Strain energy per unit length, including the Vlasov contribution
UM/VABS	University of Michigan VABS
$\mathcal{U}^{structural}$	Structural component of $\mathcal{U}^{(m)}$
$\mathcal{U}_{Vlasov}^{structural}$	Vlasov structural component of $\mathcal{U}_{refined}^{(m)}$
$V$	Applied voltage across the interdigitated electrodes
VABS	Variational Asymptotic Beam Sectional analysis
VAM	Variational Asymptotic Method
$W$	First derivative of $M_\omega$ w.r.t. $x_1$

$\hat{w}_1, \hat{w}_2, \hat{w}_3$	Unknown first perturbation warping terms in the $v_i$ directions
$w_1, w_2, w_3$	Unknown second perturbation warping terms in the $v_i$ directions
$\tilde{w}_1, \tilde{w}_2, \tilde{w}_3$	Unknown third perturbation warping terms in the $v_i$ directions
$\xi$	Curvilinear coordinate in the direction normal to the contour
$x_1, x_2, x_3$	Global Cartesian coordinates
$x_{i-local}$	Local Cartesian coordinates in the ply frame

# Contents

<b>Acceptance</b>	<b>ii</b>
<b>Abstract</b>	<b>iii</b>
<b>Acknowledgements</b>	<b>v</b>
<b>List of Abbreviations and Symbols</b>	<b>vi</b>
<b>Contents</b>	<b>xi</b>
<b>List of Figures</b>	<b>xv</b>
<b>List of Tables</b>	<b>xviii</b>
<b>1 Introduction</b>	<b>1</b>
1.1 Motivation . . . . .	1
1.2 Background . . . . .	5
1.2.1 Beam Theories . . . . .	5
1.2.2 Variational Asymptotic Method . . . . .	10
1.2.3 Fibre Composite Materials . . . . .	17
1.3 Thesis Objectives and Overview . . . . .	20

<b>2</b>	<b>Cross Sectional Analysis of Active OCSTWB</b>	<b>22</b>
2.1	Beam Geometry and Kinematics . . . . .	22
2.2	Beam Strain Energy . . . . .	26
2.3	Application of the VAM to Active OCSTWB . . . . .	33
2.3.1	Phantom Step . . . . .	33
2.3.2	First Perturbation . . . . .	38
2.3.3	Second Perturbation . . . . .	42
2.3.4	Third Perturbation . . . . .	48
2.3.5	Stiffness and Actuation Constants . . . . .	54
<b>3</b>	<b>Verification of the Active OCSTWB Analysis</b>	<b>59</b>
3.1	Cross Section Examples . . . . .	59
3.2	Preparation of Input Files . . . . .	63
3.2.1	UM/VABS . . . . .	63
3.2.2	Active OCSTWB Code . . . . .	67
3.3	Results and Discussion . . . . .	70
<b>4</b>	<b>Investigation of Beam Displacement and Twist</b>	<b>80</b>
4.1	Nonlinear 1-D Beam Problem Formulation . . . . .	80
4.2	Beam Examples . . . . .	87
4.3	Boundary Conditions and Applied Loading . . . . .	90
4.4	Beam Displacements . . . . .	94
4.5	3-D Finite Element Analysis . . . . .	99
4.6	Results and Discussion . . . . .	106
<b>5</b>	<b>Parametric Investigation of an Active I-beam</b>	<b>114</b>
5.1	I-beam Spar Configurations . . . . .	114
5.2	Results and Discussion . . . . .	119

<b>6</b>	<b>Conclusions and Recommendations</b>	<b>122</b>
6.1	Conclusions . . . . .	122
6.2	Recommendations . . . . .	123
	<b>References</b>	<b>125</b>
	<b>Appendices</b>	<b>132</b>
<b>A</b>		<b>133</b>
A.1	Shell Energy . . . . .	133
A.2	First Perturbed Strain Field . . . . .	138
<b>B</b>		<b>141</b>
B.1	GiD to UM/VABS Interface Code . . . . .	141
	B.1.1 Materials File: <code>.mat</code> . . . . .	141
	B.1.2 Output Instructions File: <code>.bas</code> . . . . .	141
B.2	Active OCSTWB Input and Output Files . . . . .	145
	B.2.1 I-Beam Contour Input File: <code>contour_input.m</code> . . . . .	145
	B.2.2 I-Beam Laminates Input File: <code>LaminatesInput.dat</code> . . . . .	146
	B.2.3 Bimoment I-Beam Output . . . . .	147
<b>C</b>		<b>149</b>
C.1	Nonlinear 1-D Beam Span Analysis Code . . . . .	149
	C.1.1 Input File: <code>beam_input.m</code> . . . . .	149
	C.1.2 Input Processing File: <code>process_input.m</code> . . . . .	150
	C.1.3 Main Analysis File: <code>beam_displacement_twist.m</code> . . . . .	153
	C.1.4 Equations Assembly File: <code>equations.m</code> . . . . .	155
	C.1.5 Jacobian Assembly File: <code>jacobian.m</code> . . . . .	157
	C.1.6 Newton-Raphson Equation Solver File: <code>newton_raphson.m</code> . . . . .	160

C.2	3-D FEA Displacement and Twist Post-processing Code . . . . .	162
C.2.1	Read 3-D FEA Output File: <code>read_ansys_results.m</code> . . . . .	162
C.2.2	Main Analysis File: <code>beam_displ_rot.m</code> . . . . .	163
C.2.3	Minimization Function File: <code>rigid_body_minimization.m</code> . . . . .	165

# List of Figures

1.1	The global Cartesian coordinates of a beam. . . . .	6
1.2	Bimoment generation in an I-beam. . . . .	9
1.3	Beam dimensions. . . . .	10
1.4	Beam end effects. . . . .	12
1.5	Deformation of the beam reference line. . . . .	14
1.6	Deformation of a piezoceramic block. . . . .	18
1.7	Components of an MFC laminate. . . . .	19
1.8	An MFC segment. . . . .	20
2.1	Beam geometry . . . . .	23
2.2	Orientation of an MFC ply . . . . .	27
2.3	Horizontal strip cross section . . . . .	46
3.1	Geometry of the example cross sections. . . . .	61
3.2	Modelled and meshed example cross sections. . . . .	65
3.3	Nodal connectivity orders for a cross section. . . . .	77
3.4	Material, ply angle and applied voltage assignments for the example cross sections. . . . .	78
3.5	Contours and paths of integration of the example cross sections. . . . .	79
3.6	Transition contour point between two laminates. . . . .	79

4.1	Discretized beam reference line. . . . .	84
4.2	Cross section of the isotropic I-beam from [1]. . . . .	88
4.3	3-D model of the isotropic I-beam example. . . . .	89
4.4	I-beam warping function parameters. . . . .	92
4.5	Angle of a deformed reference frame relative to the undeformed reference frame. . . . .	98
4.6	Front view of the lower laminate intersection of the 3-D FEA I-beam. . . .	100
4.7	Meshed 3-D FEA I-beam and channel beam models. . . . .	103
4.8	Front view of the deformed 3-D FEA I-beam and channel beam models. . .	104
4.9	Rigid body minimization with respect to a deformed cross section. . . . .	105
4.10	Twist profiles of the isotropic I-beam under various applied loading. . . .	107
4.11	Twist profiles of the strip and cruciform beams. . . . .	108
4.12	Axial extension of the active I-beam with uniform applied voltage. . . . .	109
4.13	Twist profiles of the root restrained active and passive I-beams. . . . .	110
4.14	Twist profiles of the free to warp root active and passive I-beams. . . . .	111
4.15	Twist profile of the active I-beam with the sign of the applied voltages reversed at the midspan. . . . .	112
4.16	Twist profile of the active I-beam with a free to warp root and a warping restrained tip. . . . .	113
5.1	I-beam spar embedded in a Boeing CH-47D helicopter rotor blade. . . . .	115
5.2	Cross sectional dimensions of the active I-beam spar. . . . .	115
5.3	I-beam laminate flange segments. . . . .	117
5.4	I-beam laminate span segments. . . . .	117
5.5	Twist profiles of the active I-beam spar with various flange-wise distribu- tions of carbon fibre plies. . . . .	119

5.6	Twist profiles of the active I-beam spar with various flange- and span-wise MFC ply distributions. . . . .	120
5.7	Twist profile of the optimized active I-beam spar with alternate boundary conditions. . . . .	121
5.8	Segmented airfoil. . . . .	121

# List of Tables

1.1	Outline of the three main steps of a static analysis of a prismatic beam using the VAM. . . . .	15
2.1	Voigt's condensed indice notation convention. . . . .	29
3.1	Summary of the cross section examples investigated. . . . .	60
3.2	Passive and active ply material properties. . . . .	62
3.3	Laminate lay-up and applied voltage of each branch. . . . .	62
3.4	Cross sectional stiffness constants for the isotropic channel example predicted by UM/VABS, GT/VABS and the active OCSTWB code. . . . .	71
3.5	Cross sectional stiffness and induced actuation constants of the strip and cruciform examples predicted by UM/VABS and the active OCSTWB code. . . . .	73
3.6	Cross sectional stiffness constants of the extensional and bimoment I-beam examples predicted by UM/VABS and the active OCSTWB code. . . . .	74
3.7	Cross sectional induced actuation constants of the extensional and bimoment I-beam examples predicted by UM/VABS and the active OCSTWB code. . . . .	74
3.8	Cross sectional stiffness and induced actuation constants of the channel example predicted by UM/VABS and the active OCSTWB code. . . . .	75
4.1	Summary of the beam examples investigated. . . . .	88

4.2	Applied mechanical loading and boundary conditions for the beam examples.	89
4.3	Warping functions and applied axial stresses for each branch of an I-beam cross section. . . . .	91
4.4	Applied mechanical bimoment values at the root and tip for the isotropic I-beam examples. . . . .	93
4.5	Beam equations applied to each node of a discretized beam reference line. .	95
5.1	Passive and active ply material properties. . . . .	116
5.2	Active I-beam spar configurations for the flange-wise distribution of carbon plies under constant induced bimoment. . . . .	118
5.3	Active I-beam spar configurations for the flange-wise distribution of MFC plies under constant stiffness. . . . .	118
5.4	Active I-beam spar configurations for the span-wise distribution of MFC plies under constant stiffness. . . . .	118

# Chapter 1

## Introduction

### 1.1 Motivation

The ability of a structure to change shape in a changing environment can confer many advantages. For both terrestrial and aerospace structures such as wind turbine blades, high-rise buildings, and aircraft wings and vertical tails, structural morphing provides the capability of actively controlling vibrations produced by the corresponding aeroelastic phenomena [2, 3, 4, 5]. In the case of helicopter rotor blades and tiltrotor propeller blades, morphing capabilities allow for additional possible applications including noise control [6], increased rotor blade efficiency [7] and reduction of the blade sailing phenomenon [8].

Active Fibre Composites (AFCs), as well as the more recently developed Macro Fibre Composites (MFCs) offer an alternative method of actuation to conventional linear hydraulic and electric actuators. These thin and flexible piezoelectric composite patches can be integrated into a composite lay-up of the skin of an airfoil structure, eliminating the need for internal moving parts, and providing actuating capabilities at frequencies up to 10 kHz [9]. A single 110 mm by 73 mm by 0.3 mm patch of MFC is strong enough to

actuate under resisting forces of up to 923 N [9]. Consequently, AFCs/MFCs may be particularly useful for helicopter rotor blades where the high centripetal acceleration requires low weight, the compact structure makes maintenance of internal parts difficult, and the aerodynamic forces require high frequency actuation to dampen vibrations and noise.

Another approach envisioned to achieve morphing rotor blades is to integrate MFCs into the flanges of a thin wall open section composite spar, which would be used in place of a conventional D-spar [10, 11]. The MFCs would be configured to induce twist in the thin wall open section spar, thereby causing the angle of attack and thus the aerodynamic behaviour of the rotor blade to change.

An active helicopter rotor blade prototype called the Active Twist Rotor (ATR) was developed by the National Aeronautics and Space Administration (NASA), the United States Army and the Massachusetts Institute of Technology (MIT) and used airfoil integrated AFCs to induce twist in a composite D-spar [12]. Experimental wind tunnel tests of the ATR demonstrated that it could achieve  $1.5^\circ$  twist at a frequency of 5 Hz and an applied voltage of 1000 V [12]. Numerical simulations of the ATR running at 687.5 Rotations Per Minute (RPM) and 1000 V predicted  $0.75^\circ$  tip twist at 0 Hz and a maximum of  $1.4^\circ$  at 6 Hz [13]. When MFCs were used instead of AFCs, the numerical results were  $1.3^\circ$  at 0 Hz and a maximum tip twist of  $2.8^\circ$  at 7 Hz [13]. A new variant of MFCs under development with greater actuation capability is called a single crystal MFC and uses single crystal  $\text{Pb}(\text{Mg}_{1/3}\text{Nb}_{2/3})\text{O}_3\text{-PbTiO}_3$  (PMN-PT) fibres instead of the conventional polycrystalline  $\text{Pb}(\text{ZrTi})\text{O}_3$  (PZT) fibres [14]. When single crystal MFCs were used in place of AFCs in the ATR, the numerical results were  $3.1^\circ$  tip twist at 0 Hz and a maximum of  $5.6^\circ$  at 6 Hz [13]. According to [13],  $\pm 2^\circ$  tip twist is enough to attenuate helicopter rotor blade vibrations.

There has been recent interest in using an I-beam spar to produce twist in tiltrotor and helicopter rotor blades by applying a mechanical moment couple to the I-beam spar root [1]. The goal of this research was to produce large rotor blade twist of  $2^{\circ}$ - $4^{\circ}$  at the outer 12-32% blade span for the purpose of increasing the lift produced at hover and cruise operating points for the V-22 Osprey [1]. In addition to increasing lift producing efficiency, large rotor blade twist may also be necessary to reduce the large bending deflections caused by the blade sailing phenomenon [8]. Helicopters are at risk of blade sailing during engaging/disengaging of rotors on ship decks in high wind and high sea conditions. The low rotor speeds during these phases reduce the centrifugal stiffening forces on the rotor blades and make them susceptible to large vertical bending deflections caused by the aerodynamic loads due to wind flowing over the ship and the motion of the ship in high sea conditions [8].

In the current approach to design a morphing rotor blade, MFCs are envisioned to be embedded in an I-beam spar and configured to induce a moment couple, which would result in twisting the I-beam spar. Optimization of an active rotor blade requires many iterations due to the vast design space involved. For example, optimization of a spar design may take numerous factors into consideration such as the spar and rotor blade geometry, ply lay-up, weight, strength, induced twist magnitude and spanwise location, actuation frequency response, and dynamic stability. A tool that can quickly and accurately analyse an active thin wall I-beam spar can be very useful for preliminary optimization and design studies of morphing rotor blades. Recently, a code has been developed by the Applied Dynamics Group at Carleton University that can quickly determine the cross sectional properties of active composite Open Cross Section Thin Wall Beams (OCSTWBs) [15]. This development, which will be presented in detail in Chapter 2, is based on analytical results obtained from variational asymptotic analysis of thin wall sections where the full

3-D elastic problem is reduced to a linear 2-D analytical shell problem over the cross section [15]. Alternative codes that can analyse active composite beams include standard 3-D Finite Element Analysis (FEA) codes and 2-D Finite Element (FE) cross sectional analysis codes called the Variational Asymptotic Beam Sectional (VABS) analysis and the University of Michigan VABS (UM/VABS) [16, 17].

For a 0.1 m by 0.1 m by 1 m active I-beam with a seven ply laminate, the approximate analysis times for each code on a computer with a dual core 2.2 GHz CPU are: 11 min using 3-D FEA with 44625 3-D FEs; 3 s using VABS with 616 2-D FEs; and 0.35 s using the analytical code with 600 1-D elements [18]. Neither the 3-D FEA nor the 2-D VABS analysis times include the required geometry modelling and meshing time [18]. Also, the 3-D FEA analysis time does not include the post-processing work. The minimal pre-processing work and the fast analysis times make the analytical based code an attractive alternative to FE codes for high-iteration analysis of active OCSTWB. An additional advantage of the active OCSTWB theory is that it gives physical insight into the beam mechanics, allowing one to see the stiffness and induced actuation terms that contribute to a particular deformation behaviour of a beam. The primary motivation for the development of a fast active OCSTWB analysis code is for the real-time analysis of a helicopter rotor blade with an embedded active I-beam spar [8]. This was done for the purpose of developing a dynamic control system for active rotor blades. Additionally, this analytical code has potential applications in the development of other morphing terrestrial and aerospace applications where large design spaces are present.

The goal of this research was to validate the active OCSTWB analytical code and use it to optimize the configuration of an active I-beam spar for maximum twist.

## 1.2 Background

### 1.2.1 Beam Theories

A beam is a geometrically slender structure where one dimension is much larger than the other two. When arbitrarily loaded, a highly complex set of deformations may be produced in a general beam. For special cases of beam geometry, boundary conditions, loading and materials, a small number of deformation modes become dominant, allowing these beams to be accurately analysed using simple beam theories. In general, beam theories begin by an analysis of a beam cross section, followed by an analysis along the beam span [19]. For classical beam theory, the constitutive relation derived from a cross sectional analysis has the form [19]

$$\begin{bmatrix} F_1 \\ M_1 \\ M_2 \\ M_3 \end{bmatrix} = \begin{bmatrix} EA & 0 & 0 & 0 \\ 0 & GJ & 0 & 0 \\ 0 & 0 & EI_2 & 0 \\ 0 & 0 & 0 & EI_3 \end{bmatrix} \begin{bmatrix} \gamma_{11} \\ \kappa_1 \\ \kappa_2 \\ \kappa_3 \end{bmatrix} \quad (1.1)$$

where  $F_1$  is the axial force along the  $x_1$  direction,  $M_1$  is the torque about the  $x_1$  axis, and  $M_2$  and  $M_3$  are the bending moments about the  $x_2$  and  $x_3$  axes, respectively;  $EA$  is the axial rigidity;  $GJ$  is the Saint-Venant torsional rigidity;  $EI_2$  and  $EI_3$  are the flexural rigidities about the transverse beam axes; and  $\gamma_{11}$  is the extensional strain in the  $x_1$  direction,  $\kappa_1$  is the torsional strain about the  $x_1$  axis, and  $\kappa_2$  and  $\kappa_3$  are the bending strains about the  $x_2$  and  $x_3$  axes, respectively. The global Cartesian coordinates  $x_i$  of a beam are shown in Figure 1.1. This form includes pure axial beam extension, Saint-Venant torsion theory and Euler-Bernoulli beam bending theory. These beam theories are called the classical beam theories and their four corresponding strains are called the classical strain measures [8, 20].

The ad-hoc assumptions associated with Saint-Venant torsion theory are: cross sections

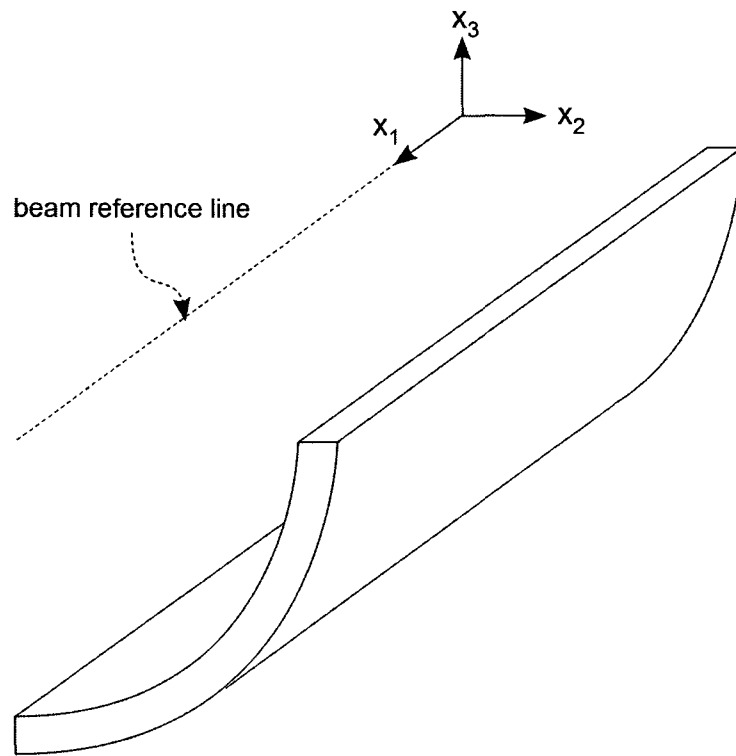


**Figure 1.1:** The global Cartesian coordinates  $x_i$  of a beam.

remain rigid in their own plane, the torsional stiffening end effects of restrained warping decay quickly from the beam ends and do not have a significant impact on the global behaviour of the beam, and the rate of twist is constant along the beam length [21]. For Euler-Bernoulli beam theory, the ad-hoc assumptions are: cross sections remain normal to the neutral surface after deformation and the axial strain varies linearly in the transverse direction [22]. Both theories assume that the beam is composed of a homogeneous, linearly elastic isotropic material and has no initial twist or curvature. Consequently, the classical beam model given by Eq. 1.1 is potentially accurate enough for the analysis of an isotropic, prismatic beam with a solid thick wall cross section [19].

One exception is the special case of an open cross section thin wall beam where the end effects of restrained warping decay slowly from the beam end and thus have a significant

effect on the global beam deformation behaviour [23]. In this case, an additional degree of freedom  $\kappa'_1$ , the change in rate of twist with respect to the axial coordinate corresponding to Vlasov beam theory must be incorporated into the beam constitutive model in order to account for this significant deformation mode [23]. Another exception is for beams that have a short length to cross sectional depth ratio, or when short wavelength vibrations, which are associated with high frequency vibration, must be captured where the transverse shear deformations become significant [20, 24]. In these cases, two additional degrees of freedom  $2\gamma_{12}$  and  $2\gamma_{13}$ , the transverse shear strains corresponding to Timoshenko beam theory must be captured [20]. Thus, in Vlasov beam theory, the Saint Venant assumption that cross sections remain rigid in their own plane after deformation is relaxed [23]; and in Timoshenko beam theory, the Euler-Bernoulli assumption that cross sections remain normal to the midplane after deformation is relaxed [22]. Higher order beam theories that further relax the assumptions of classical beam theory are available; however, the additional accuracy they provide is not large enough for most engineering applications [22].

Many beam theories have been developed in an attempt to accurately model beam deformations. These theories may be compared on bases such as mathematical rigour; complexity and ease of implementation; the ability to capture all nonlinearities and coupling phenomena; the ability to analyse anisotropic materials and complex beam structures; and the ability to recover the full 3-D displacement field from the 1-D spanwise solution [19]. Before the 1980's, most beam theories were developed to model isotropic beams; however, with the availability of advanced composite materials in the 1980s, subsequent research has mostly focused on the development of anisotropic beam theories [19]. For an anisotropic OCSTWB, the appropriate constitutive model must include, in addition to the classical beam constitutive model, off-diagonal terms in the stiffness matrix to account for the coupling phenomena present in anisotropic materials, and the extra Vlasov degree of freedom

$\kappa'_1$  to account for the significant restrained warping present in OCSTWB [8, 17, 19, 25], i.e.,

$$\begin{bmatrix} F_1 \\ M_1 \\ M_2 \\ M_3 \\ M_\omega \end{bmatrix} = \begin{bmatrix} C_{11} & C_{12} & C_{13} & C_{14} & C_{15} \\ C_{12} & C_{22} & C_{23} & C_{24} & C_{25} \\ C_{13} & C_{23} & C_{33} & C_{34} & C_{35} \\ C_{14} & C_{24} & C_{34} & C_{44} & C_{45} \\ C_{15} & C_{25} & C_{35} & C_{45} & C_{55} \end{bmatrix} \begin{bmatrix} \gamma_{11} \\ \kappa_1 \\ \kappa_2 \\ \kappa_3 \\ \kappa'_1 \end{bmatrix} \quad (1.2)$$

where  $C_{ij}$  are the terms of stiffness matrix  $\mathbf{C}$ , and  $M_\omega$  is a moment couple or *bimoment*, which is associated with the Vlasov refinement [26]. A bimoment can be caused on the cross section of a beam as the result of normal axial stresses; it causes no net force or moment in the beam. It produces beam twist, as shown in Figure 1.2 [26].

As rotor blades are relatively slender beams, the deformations due to shear are negligible and the Timoshenko-like model is not required; however, if high-frequency vibration modes must be captured or if the anisotropic OCSTWB is a relatively short and deep beam, a Timoshenko-like refinement should be considered [8].

In 1979, V.L. Berdichevskii published a paper describing a new mathematical approach to analysing reducible structures, such as shells, plates and beams, where one dimension is much smaller or larger than the other two [27]. This approach, called the Variational Asymptotic Method (VAM), is capable of rigorously reducing a full 3-D beam elasticity problem to a linear 2-D problem over the cross section and a nonlinear 1-D problem along the selected beam reference line [8, 27]. Anisotropic beam theories since then may be classified into two categories: those based on the VAM and those based on ad-hoc assumptions [19]. The advantage of the former is that they are rigorous and will consequently work on all beam geometries and ply lay-ups, unlike the latter [19, 17].

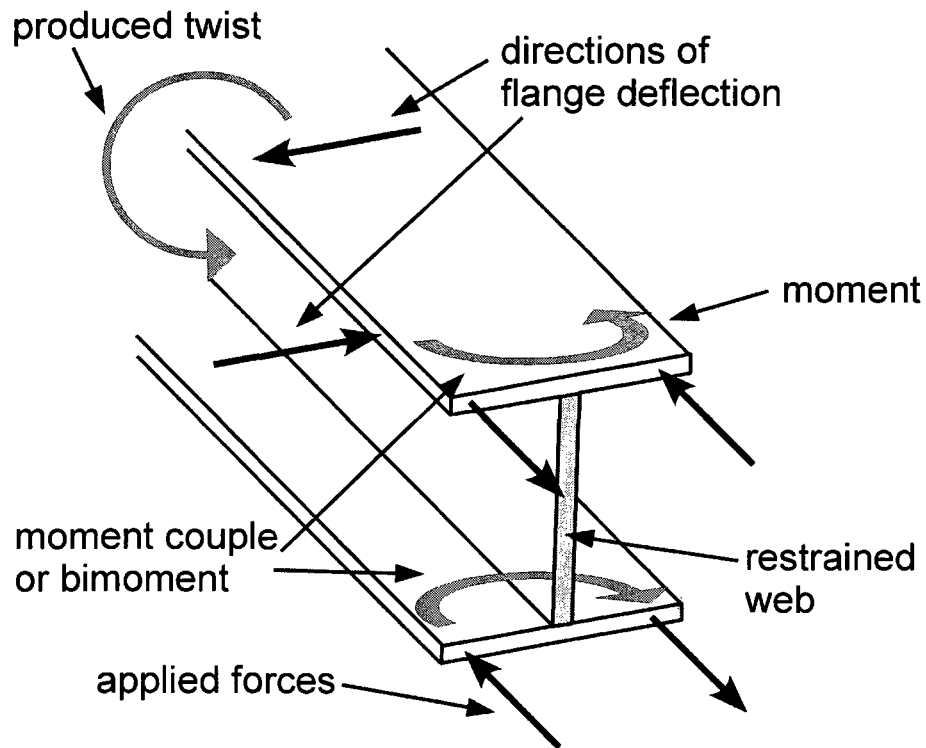


**Figure 1.2:** I-beam root with a fully restrained web and free-to-warp flanges. A set of forces applied to the flanges cause a bimoment and thereby produce twist in the I-beam.

A widely used numerical structural analysis tool that can analyse anisotropic beams is the 3-D Finite Element Method (FEM)—or Finite Element Analysis (FEA) [1, 7, 23, 25]. Excellent agreement has been shown between it and experimental results in predicting the deflection and twist behaviour of anisotropic beams under various loading and boundary conditions [28, 29]. The intensive pre-processing work involved in modelling and meshing a beam and the expensive computation time make this method uneconomical for high-iteration beam analysis; however, in the absence of any experimental validation, the results from a 3-D FEA analysis can be used to validate a new approach [1, 7, 19, 23, 25].

### 1.2.2 Variational Asymptotic Method

Reducible structures are those that have one or two dimensions that are much smaller or larger than the others, such as thin shells and plates, or slender beams. In the case of an OCSTWB, it is a reducible structure that has both the slenderness of a beam and the thinness of a shell, as shown in Figure 1.3.

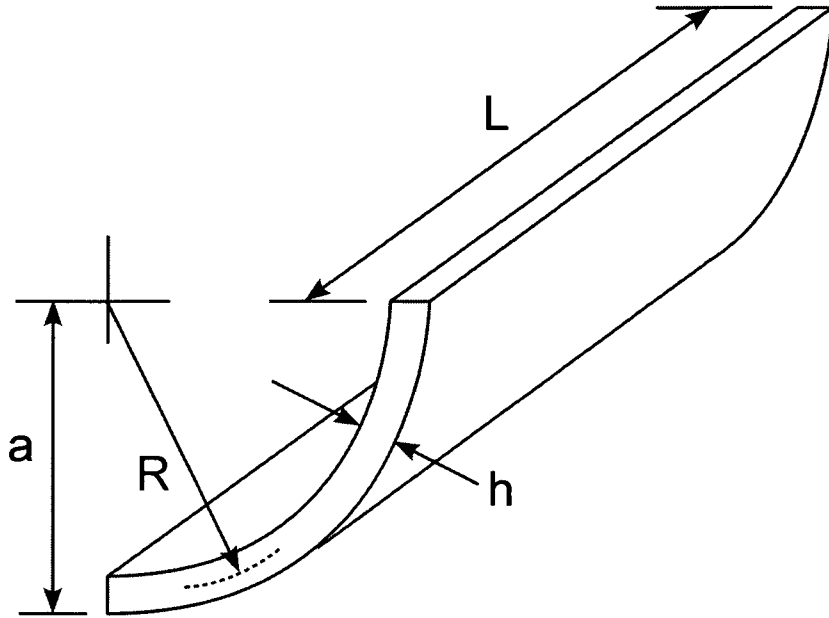


**Figure 1.3:** Beam dimensions that define the small parameters.

As seen in Figure 1.3,  $L$  is the beam length,  $a$  is the characteristic dimension of the cross section,  $h$  is the thickness of the walls, and  $R$  is the radius of curvature of the wall contour, which is of the same order as  $a$ , i.e.,  $\mathcal{O}(R) \approx \mathcal{O}(a)$ . These dimensions result in small parameters, shown in Eqs. 1.3, which are the basis for the dimensional reduction procedure of the VAM.

$$\mathcal{O}\left(\frac{a}{L}\right) \ll 1 \quad \text{and} \quad \mathcal{O}\left(\frac{h}{a}\right) \ll 1 \quad (1.3)$$

The VAM can be used to construct an asymptotically correct energy functional per unit

length and an approximate strain field along the reference line of the beam, by finding stationary points of the 3-D elastic energy functional [8, 17, 19, 27]. This results in an asymptotic series of terms of increasing order with respect to the small parameters for the energy functional. In the VAM, the order of all the terms are determined in comparison to the order of the maximum strain in the beam, where in the case of an OCSTWB,  $\epsilon = \max(|\gamma_{11}|, h|\kappa_1|, a|\kappa_2|, a|\kappa_3|)$  [8]. The order of the wavelength of most of the deformations in the axial direction  $l$  are assumed to be of the order of the beam length  $L$ ; however, some deformation modes exist only locally near a restrained end and have deformation lengths much less than the beam length  $L$ . Consequently, in reference to Eqs. 1.3, a more general form of the small parameters involves replacing the beam length  $L$  with the wavelength of elastic deformations  $l$  in the axial direction

$$\mathcal{O}\left(\frac{a}{l}\right) \ll 1 \quad \text{and} \quad \mathcal{O}\left(\frac{h}{a}\right) \ll 1 \quad (1.4)$$

This modified small parameter is generally satisfied for long wavelength static and low frequency dynamic deformations [19]. As an aside, the classical strain measures give the internal beam deformation modes, where the cross sections remain rigid during deformation [19]. Figure 1.4 conceptualizes the effect of various external end conditions on the twist profile along the length of a beam that is subjected to a mechanical torque at the tip. In this diagram, curve (a) shows pure Saint-Venant internal twist in the beam, which would occur for free-free root-tip boundary conditions. External deformation modes, such as the Vlasov and camber modes, are the result of restrained warping at the beam ends [19]. The fast decaying end condition near the root seen in curve (b), which would occur at a fixed root for a thick wall solid section or thin wall closed section, may be neglected since it does not have a significant effect on the global twist behaviour of the beam. In the case of an OCSTWB with a fixed root, the slow decaying Vlasov end condition, shown near the root of curve (c), will have a large effect on the global beam twist behaviour, and thus must be

considered in the beam model. The long wavelength of deformation  $l$  associated with the Vlasov deformation mode for OCSTWB will consequently satisfy the small parameters of Eqs. 1.4 when performing the Vlasov refinement in the dimensional reduction procedure.

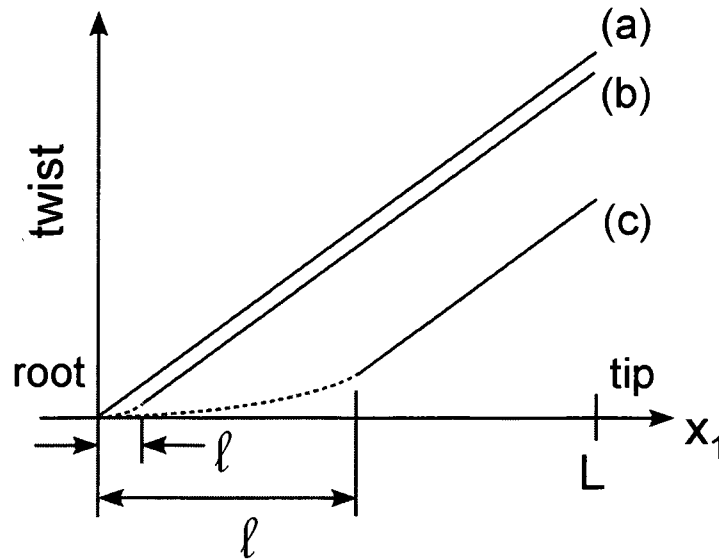


**Figure 1.4:** The effect of various external end conditions on the twist profile of a beam with a mechanical torque applied at the tip, a) Beam with a free to warp root, and thus no external end condition, resulting in pure Saint Venant internal twist, b) Fast decaying external end condition having negligible impact on the general twist behaviour, c) Slow decaying end condition having a large effect on the general twist behaviour. The value of twist has been referenced to zero at the root end.

As the wall thickness decreases, the wavelength of the Vlasov deformation mode will increase, causing the conditions given in Eqs. 1.4 to be better satisfied and the resultant solution to be more accurate [19]. According to the literature, a beam is classified as a thin wall beam when the thinness parameter  $\mathcal{O}(h/a)$  is less than  $1/15$ , and the slenderness parameter  $\mathcal{O}(a/L)$  is less than  $1/10$  [15, 17, 26].

The beam analysis process begins by obtaining the strain field from a linear 2-D analysis of the cross section using the VAM. These strains, that are functions of the axial coordinate  $x_1$  only, Figure 1.5, appear in the right-hand column in Eq. 1.2. The resultant energy

functional is a function of these strains only and has dimensions in the form of energy per unit length. These strains vary along a beam reference line, which defines the origin of the cross sectional coordinate system and the  $x_1$  coordinate [19]. Convenient choices for the reference line are the shear centre, as discussed in [23] and [17], and the area centroid, as used in [30] and [19]. For anisotropic beams, the shear centre can be found by first constructing a Timoshenko-like model, as discussed in [17]. Differentiation of the energy functional with respect to the strains gives the stiffness terms of the beam constitutive equation, as given in Eq. 1.2. Next, the constitutive relation is used together with a set of six nonlinear intrinsic static equilibrium equations, given by [19, 23], in order to find the strains and mechanical forces, moments and bimoment along the beam span. Using the computed strains and the geometric relations given in [19], the deformation of the reference line, and beam twist about it, may be found. The deformation of the beam reference line, shown in Figure 1.5, represents the global rigid-body deformation of the beam [19].

In Figure 1.5,  $x_1$  is the global beam axial coordinate;  $x_2$  and  $x_3$  are the global beam cross sectional coordinates in the horizontal and vertical directions, respectively;  $\mathbf{b}_i$  are the local orthonormal unit vectors corresponding to an undeformed cross section; and  $\mathbf{B}_i$  are the local orthonormal unit vectors corresponding to a deformed cross section that has undergone an arbitrary translation and rotation. The translation components in the  $x_1$ ,  $x_2$  and  $x_3$  directions from an undeformed local coordinate system to its corresponding deformed local coordinate system are designated as  $u_1$ ,  $u_2$  and  $u_3$ . Finally, the 3-D displacement, strain and stress fields are recovered using appropriate relations, as given in [19, 23]. The 3-D displacement field includes the cross sectional warping, which is referred to as the local deformation of the beam [19]. The above beam analysis procedure may be summarized into three general steps, as shown in Table 1.1.

Fundamental assumptions of the present OCSTWB theory include beam slenderness, long wavelength deformations, wall thinness, small strain, moderate local rotation, zero

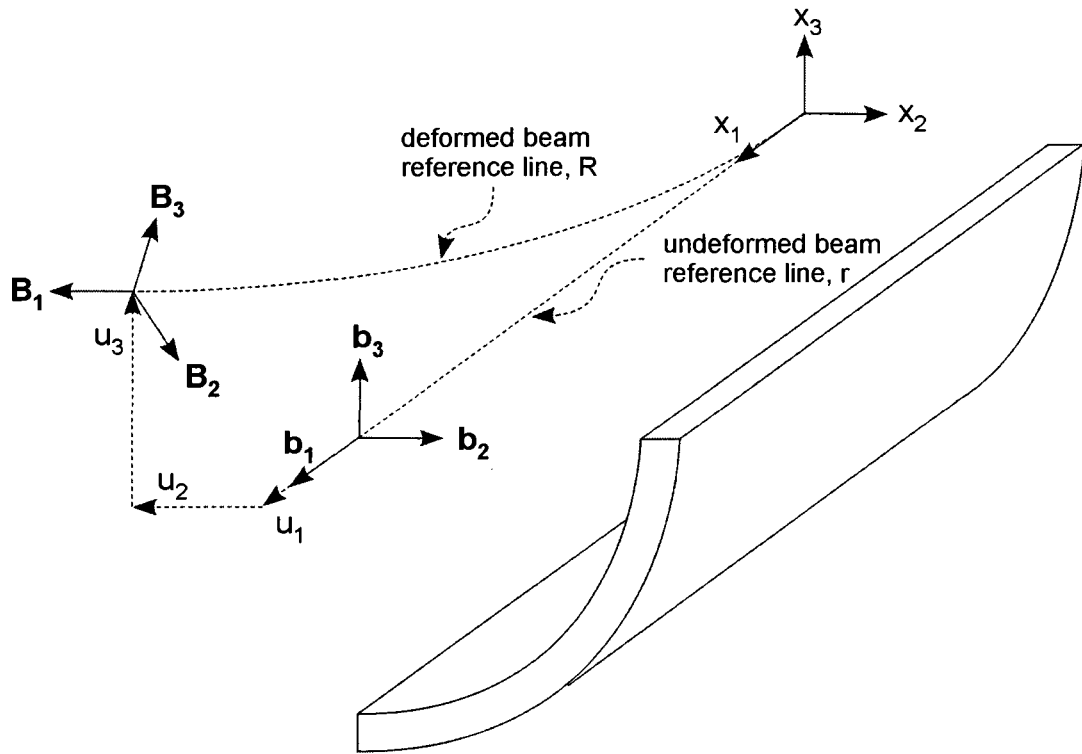


**Figure 1.5:** The deformation of the beam reference line from its undeformed state to its deformed state after an arbitrary translation and rotation.

initial twist and curvature, and linearly elastic materials [8, 19]. The VAM and its past applications to passive beams will be outlined in the remainder of this section, the recent application of the VAM to the cross sectional analysis of active OCSTWB is presented in Chapter 2, and the nonlinear 1-D analysis is described in Chapter 4. Full 3-D recovery is beyond the scope of this work.

The VAM is an iterative method designed to approximate the 3-D elastic or shell energy as an asymptotic series of terms of increasing order with respect to the small parameters, given in Eqs. 1.4. As previously mentioned, the largest strain measure in the beam is of  $\mathcal{O}(\epsilon)$  [8]. The objective of the VAM is to identify all terms in the strain field of  $\mathcal{O}(\epsilon)$ , resulting in a solution of  $\mathcal{O}(\epsilon)$  accuracy. In other words, the VAM is a

**Table 1.1:** Outline of the three main steps of a static analysis of a prismatic beam using the VAM.

	Input	Output
1. Linear 2-D cross sectional analysis using the VAM.	<ul style="list-style-type: none"> <li>• Beam geometry</li> <li>• Material properties</li> </ul>	<ul style="list-style-type: none"> <li>• <i>Cross sectional stiffness constants</i></li> <li>• <i>Warping functions</i></li> </ul>
2. Nonlinear 1-D analysis along the beam span.	<ul style="list-style-type: none"> <li>• <i>Cross sectional stiffness constants</i></li> <li>• Boundary conditions</li> <li>• Applied loading</li> </ul>	<ul style="list-style-type: none"> <li>• <i>Global twist and displacement of the beam</i></li> <li>• <i>Strains, forces, moments and bimoments along the beam span</i></li> </ul>
3. Full 3-D recovery.	<ul style="list-style-type: none"> <li>• <i>Global twist and displacement of the beam</i></li> <li>• <i>Strains along the beam span</i></li> <li>• <i>Warping functions</i></li> </ul>	<ul style="list-style-type: none"> <li>• Local displacement, strain and stress fields</li> </ul>

method that rigorously transforms an exact 3-D elastic or shell analysis problem to a linear 2-D problem. Before beginning the VAM analysis, the 3-D elastic or shell strain energy functional is symbolically transformed to an exact energy functional per unit length, composed of unknown strains at the beam reference line. There are two main parts to a VAM cross sectional analysis:

1. In the zeroth approximation, a general strain field, in terms of unknown displacements, is substituted into the energy functional and excessively large terms with respect to  $\mathcal{O}(\epsilon^2)$ , such as  $\mathcal{O}(\epsilon^2(a/l)^{-2})$  and  $\mathcal{O}(\epsilon^2(a/l)^{-4})$ , are eliminated. In the existing literature, this elimination is referred to as “killing” or “annihilating,” as these excessively large terms, called “phantom” terms, are fictitious terms that cannot physically exist since they would violate the assumption that the classical strains

are the largest strains present in the beam [8, 19].

- As the energy functional is quadratic with respect to the strains, the corresponding order of the strains in the above energy terms are  $\mathcal{O}(\epsilon)$ ,  $\mathcal{O}(\epsilon(a/l)^{-2})$  and  $\mathcal{O}(\epsilon(a/l)^{-1})$ .
  - The zeroth approximation may require up to two steps: where the first step gives the rigid-body displacement field, and the second step, if necessary, would involve perturbing the strain field and using the perturbation terms to eliminate any remaining excessively large terms [19].
2. Each subsequent step involves iteratively perturbing the strain field and minimizing the energy functional, in order to produce additional strain terms of  $\mathcal{O}(\epsilon)$  [19].
- These iterations continue until no new strain terms of  $\mathcal{O}(\epsilon)$  are produced, where usually one or two iterations are required. At this point, the resultant energy functional is considered to have converged to  $\mathcal{O}(\epsilon^2)$  accuracy [19].
  - Unlike for the case of thin wall closed cross section beams, no constraint equations need to be applied to the energy functional for OCSTWB [8].

The above beam analysis approach using the VAM has been applied to general passive and active beam cross sections using the 2-D cross sectional beam analysis codes, VABS, developed originally at the Georgia Institute of Technology and will be referred to as GT/VABS in this thesis. A similar development at the University of Michigan is known as the University of Michigan VABS (UM/VABS) [16, 31, 32, 33]. These codes have been verified against 3-D FEA and experimental data [16, 17, 23, 25]. The VAM has additionally been applied to and verified for passive open and closed cross section thin wall beams, yielding analytical solutions for the cross sectional stiffness constants and warping functions [19, 34, 35]. Recently, the VAM has been applied to active open and

closed cross section thin wall beams, yielding analytical solutions for the cross sectional stiffness constants, warping functions, and induced force/moments and in the open section case, bimoment [8, 15, 18, 36, 37]. This thesis focuses on the verification of the active OCSTWB code developed by the Applied Dynamics Group at Carleton University.

### 1.2.3 Fibre Composite Materials

Modern aerospace structures are being manufactured with an increasingly larger percentage of advanced composite materials, such as carbon fibre composites [38]. A fibre composite material consists of a thin aligned sheet of flexible strong fibres, such as carbon, kevlar or E-glass, which are embedded in a matrix material, such as epoxy. These highly anisotropic materials are consequently very strong in the fibre direction, while being highly resistant to corrosion and fatigue due to the polymer matrix that protects the fibres from mechanical and chemical damage. A stacking, or “lay-up” of fibre composite sheets, also called “plies” or “lamina,” forms a laminate shell structure, whose strength may be tailored in specific directions by varying the orientation of the plies. The primary advantages of fibre composite materials, as compared to the traditional aluminium alloys used in aerospace structures, include fatigue resistance and weight savings. Fibre composite materials are also used in high performance terrestrial applications such as wind turbines, watercraft, land vehicles and sports equipment.

Materials that change shape in the presence of an electric field, or conversely generate an electric field when mechanically deformed are called piezoelectric materials [39]. There are both ceramic and polymer piezoelectric materials; however, piezoceramics have far greater actuation capability than piezopolymers—on the order of 300 times greater [39]. A piezoceramic material is one whose asymmetrical crystal structure has its electric dipoles oriented in a net average direction [39]. A piezoceramic block in its deformed and undeformed state, polarized in the  $x_{1-local}$  direction, is shown in Figure 1.6. The local ply

coordinates  $x_{i-local}$  are related to the undeformed beam and laminate coordinates  $x_i$  by the ply angle  $\vartheta$ , as shown in Figure 2.2.

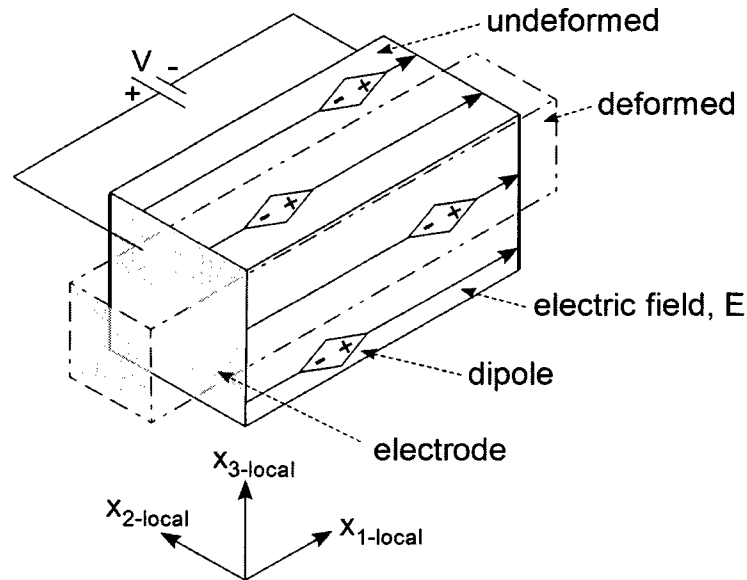


**Figure 1.6:** Deformation of a piezoceramic block by an applied electric field.

The most common type of piezoceramic is lead zirconium titanate (PZT) [39]. In 1997, the concept of a piezoelectric fiber composite was proposed where PZT fibres are embedded in an epoxy matrix and sandwiched between two thin polyimide films with interdigitated copper electrodes etched onto them [40, 41, 42]. The first implementation of this technology was called an Active Fibre Composite (AFC) [41]. PZT fibres with a circular cross section were extruded and laid across a bottom sheet of interdigitated electrodes coated with a layer of epoxy. Another coating of epoxy was applied to the top of the PZT fibres, the top sheet of interdigitated electrodes was added, and the laminate was pressed and heated in a mold with a vacuum port to eliminate voids. Finally, the laminate was heated above the PZT's Curie temperature and a high electric voltage of about 3000 V was applied to the interdigitated electrodes for about a minute in order to polarize the dipoles [41]. Various types of PZT materials have been manufactured by “doping” them with other atoms, such as lanthanum, lithium, sodium, potassium and bismuth, or by altering their

manufacturing processes, in order to modify their mechanical and electrical properties, such as their actuation capabilities and Curie temperatures [43, 44]. The second and more recent variant of a piezoelectric fibre composite is called a Macro Fibre Composite (MFC) [41]. Instead of extruding PZT fibres, as was done for AFCs, the PZT fibres are produced by sawing PZT wafers into strips [41]. This innovation results in PZT fibres that have a rectangular cross section rather than a circular one, leading to improved contact between the PZT fibres and electrodes, increased surface area between the fibres and epoxy matrix, and a higher fiber volume fraction. Consequently, the advantages of MFCs over AFCs include lower required applied voltages, improved actuation efficiency and performance, less susceptibility to fibre pull-out, and reduced manufacturing costs [45]. An MFC laminate with exposed components is shown in Figure 1.7.

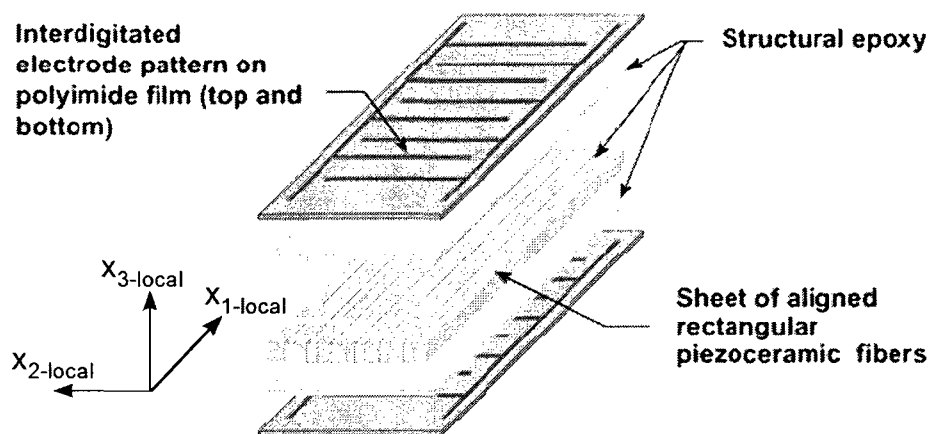


**Figure 1.7:** Exploded view of an MFC laminate, courtesy of [9].

The PZT dipole orientations alternate between the electrodes, as do the electric field directions, as shown in Figure 1.8. This configuration will result in tensile strain—positive strain—in the  $x_{1-local}$  fibre direction. When initially polarized, only the PZT fibre segments in between the electrodes will be oriented in the  $x_{1-local}$  direction, and hence, only the PZT fibre segments in between the electrodes will contribute to the laminate strain, as shown in Figure 1.8 [46]. There have been various forms of research into improving the

properties of piezoelectric fibre composites, such as by optimizing the MFC geometry to minimize the inactive fibre segments called “dead zones” under the electrodes; manufacturing hollow PZT fibres to reduce the voltage requirements; developing new resins with improved mechanical and dielectric properties to minimize fibre pullout and maximize voltage transfer to the fibres; and using single crystal  $\text{Pb}(\text{Mg}_{1/3}\text{Nb}_{2/3})\text{O}_3\text{-PbTiO}_3$  (PMN-PT) fibres instead of the polycrystalline  $\text{Pb}(\text{ZrTi})\text{O}_3$  (PZT) fibres to increase actuation performance [41, 45, 46].

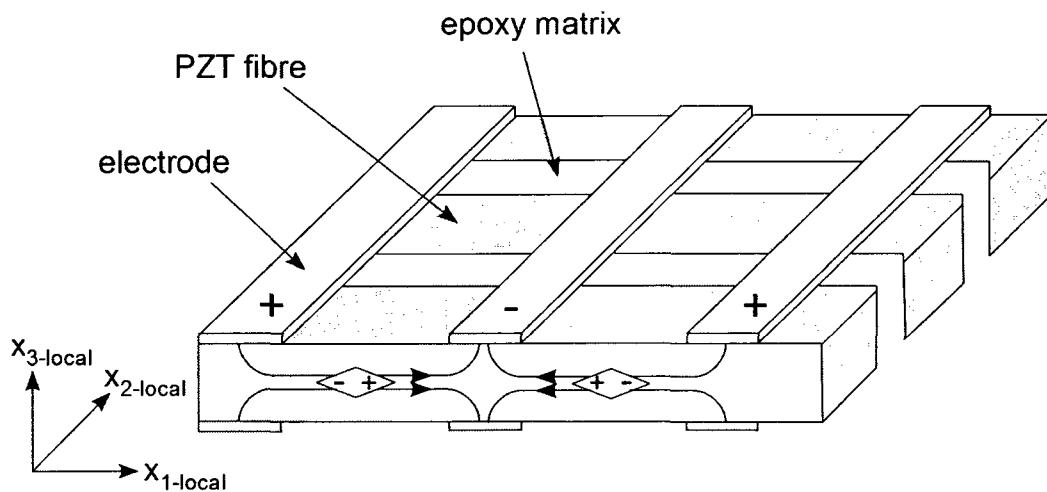


**Figure 1.8:** A segment of an MFC with an applied electric field inducing positive strain in the  $x_{1\text{-local}}$  direction, courtesy of [9].

### 1.3 Thesis Objectives and Overview

The objectives of this thesis were to validate the analytical model and the corresponding code that was developed by earlier studies to obtain cross sectional constants and activation forces, moments and bimoment for an active OCSTWB. This required a thorough investigation of the underlying mathematical development, the outline of which is presented in the thesis. Finally, the code was used to perform a parametric investigation of

an open section thin wall I-beam spar for maximum induced twist.

In order to accomplish these objectives, a detailed derivation of the active OCSTWB theory is presented first in Chapter 2, including a derivation of the beam kinematics, the mechanical shell strain energy functional and the analytical expressions for the cross sectional stiffness constants and induced force/moments/bimoment. Next, the active OCSTWB analysis code is verified against the 2-D FEA codes: UM/VABS and GT/VABS using various beam examples in Chapter 3. The cross sectional analysis results are subsequently verified against 3-D FEA solutions by using them in a nonlinear 1-D problem along the beam length to calculate the average beam displacement and twist profiles in Chapter 4. In Chapter 5, a parametric investigation of an I-beam spar for maximum twist was performed using the analytical active OCSTWB code. Finally, the conclusions and recommendations from this research work are given in Chapter 6.

# Chapter 2

## Cross Sectional Analysis of Active OCSTWB

The development in this chapter follows the analytical active OCSTWB theory given in [8, 15, 18], which was an extension of the analytical OCSTWB theory found in [19]. The contribution of the work presented in this chapter is to outline the development of this theory in comprehensive detail.

### 2.1 Beam Geometry and Kinematics

Rather than analysing an arbitrary active OCSTWB cross section using full 3-D elasticity theory, the analysis may be simplified by beginning from shell theory instead. In shell theory, a beam is more conveniently described by a curvilinear coordinate system rather than a Cartesian coordinate system, as shown in Figure 2.1 for an arbitrary OCSTWB.

In Figure 2.1,  $x_i$  represents the global Cartesian coordinate system, whose origin is at the beam root, and  $u_i$  are the displacements of the beam reference line at a particular axial position  $x_1$  in the corresponding  $x_i$  directions. At any particular axial position  $x_1$ ,

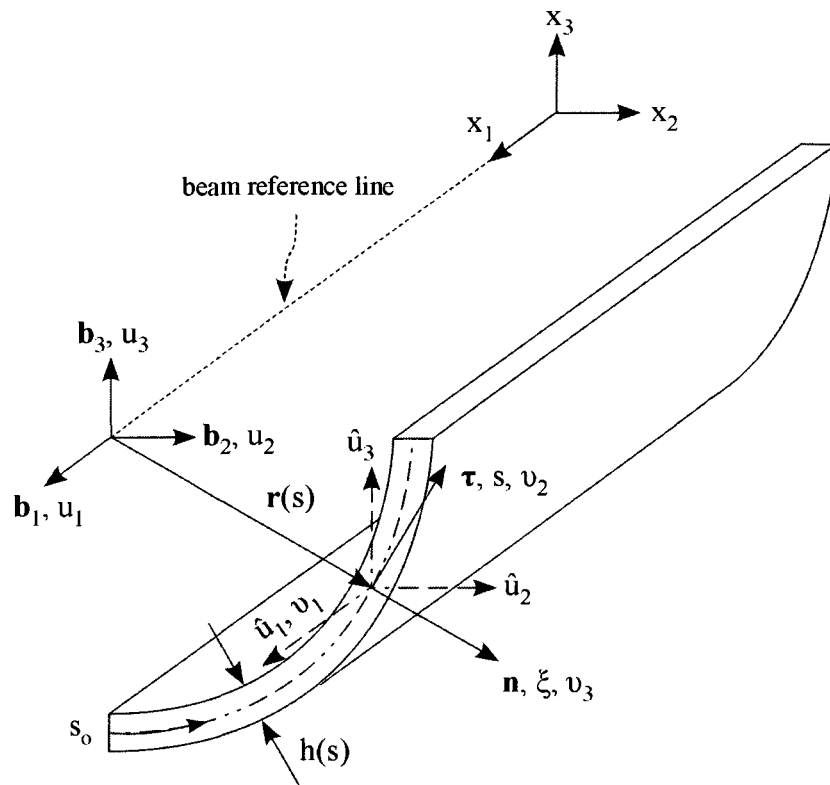


**Figure 2.1:** An arbitrary OCSTWB's geometry described by a curvilinear coordinate system.

$\mathbf{b}_i$  are a set of local unit vectors in the  $x_i$  directions. The curvilinear coordinate system is described by  $x_1$ ,  $s$  and  $\xi$ , where  $s$  is the contour coordinate and  $\xi$  is the shell thickness coordinate, in the outward normal direction  $\mathbf{n}$  to the contour. A beam contour is a line in the cross sectional plane that traces the points of mid-thickness along the shell walls; the contour coordinate  $s$  is always tangent to the contour direction  $\boldsymbol{\tau}$  and has an arbitrary point of origin  $s_0$ . Moreover,  $v_i$ , are the beam thin wall displacements in the corresponding curvilinear directions:  $x_1$ ,  $s$  and  $\xi$ . The vector,  $\mathbf{r}(s)$  in Figure 2.1 relates the origin of the  $\mathbf{b}_i$  orthonormal triad to a point on the contour of the corresponding cross section. In the global Cartesian coordinate system,  $\mathbf{r}$ ,  $\boldsymbol{\tau}$  and  $\mathbf{n}$  satisfy the following relations:

$$\begin{aligned}
\mathbf{r} &= x_2 \mathbf{b}_2 + x_3 \mathbf{b}_3 \\
\boldsymbol{\tau} &= \dot{\mathbf{r}} = \dot{x}_2 \mathbf{b}_2 + \dot{x}_3 \mathbf{b}_3 \\
\mathbf{n} &= \boldsymbol{\tau} \times \mathbf{b}_1 = \dot{x}_3 \mathbf{b}_2 - \dot{x}_2 \mathbf{b}_3
\end{aligned} \tag{2.1}$$

where the dot above the  $x_i$  terms signifies partial differentiation with respect to the contour coordinate  $s$ ,  $\dot{x} = \frac{\partial x}{\partial s}$ . The components of  $\mathbf{r}$  in the  $\boldsymbol{\tau}$  and  $\mathbf{n}$  directions are

$$r_\tau = \boldsymbol{\tau} \cdot \mathbf{r} = \dot{x}_2 x_2 + \dot{x}_3 x_3 \tag{2.2}$$

$$r_n = \mathbf{n} \cdot \mathbf{r} = \dot{x}_3 x_2 - \dot{x}_2 x_3 \tag{2.3}$$

The Frenet-Serret relations may be used to find expressions for the radius of curvature of the contour [47]

$$\begin{aligned}
R &= \frac{-\mathbf{n}}{\dot{\boldsymbol{\tau}}} \\
R &= \frac{-\dot{x}_3 \mathbf{b}_2 + \dot{x}_2 \mathbf{b}_3}{\ddot{x}_2 \mathbf{b}_2 + \ddot{x}_3 \mathbf{b}_3}
\end{aligned} \tag{2.4}$$

As the direction of  $\dot{\boldsymbol{\tau}}$  is parallel to  $\mathbf{n}$ , the ratio of their components must be equal:

$$\frac{-\dot{x}_3}{\ddot{x}_2} = \frac{\dot{x}_2}{\ddot{x}_3} \tag{2.5}$$

Using Eq. 2.5 to eliminate one of the variables from Eq. 2.4, the radius of curvature of the contour at any point  $s$  is found to be

$$R = \frac{-\dot{x}_3}{\ddot{x}_2} = \frac{\dot{x}_2}{\ddot{x}_3} \quad (2.6)$$

Curvilinear displacements relative to the Cartesian displacements at an arbitrary point on the shell are

$$\begin{aligned} v_1 &= \hat{u}_1 \\ v_2 &= \boldsymbol{\tau} \cdot (\hat{u}_2 \mathbf{b}_2 + \hat{u}_3 \mathbf{b}_3) = \hat{u}_2 \dot{x}_2 + \hat{u}_3 \dot{x}_3 \\ v_3 &= \mathbf{n} \cdot (\hat{u}_2 \mathbf{b}_2 + \hat{u}_3 \mathbf{b}_3) = \hat{u}_2 \dot{x}_3 - \hat{u}_3 \dot{x}_2 \end{aligned} \quad (2.7)$$

where  $\hat{u}_i$  denotes a displacement of a point on the cross section in the  $x_i$  direction at a contour position  $s$ , as shown in Figure 2.1.

The total strain tensor of a shell structure can be described by the generalized shell strain measures  $\gamma_{\alpha\beta}$  and  $\rho_{\alpha\beta}$  such that [48, 49]

$$\varepsilon_{\alpha\beta} = \gamma_{\alpha\beta} + \xi \rho_{\alpha\beta} \quad (2.8)$$

where  $\gamma_{\alpha\beta}$  are the strain measures that correspond to in-plane shell stretching, and  $\rho_{\alpha\beta}$  are the strain measures that correspond to shell bending/curvature, and  $\xi$  is the outward normal coordinate to the shell midplane. In this chapter, Greek indices vary from 1 to 2, while Latin indices vary from 1 to 3. These generalized strain measures may be written in terms of the curvilinear displacements, Eqs. 2.7, for cylindrical shells, as was proposed by Koiter and Sanders [34, 49]

$$\begin{aligned}
\gamma_{11} &= v_{1,1} \\
\rho_{11} &= v_{3,11} \\
2\gamma_{12} &= v_{1,2} + v_{2,1} \\
\rho_{12} &= v_{3,12} + \frac{1}{4R}(v_{1,2} - 3v_{2,1}) \\
\gamma_{22} &= v_{2,2} + \frac{v_3}{R} \\
\rho_{22} &= v_{3,22} - \left(\frac{v_2}{R}\right)_{,2}
\end{aligned} \tag{2.9}$$

where  $(\cdot)_{,1} = \frac{\partial(\cdot)}{\partial x_1}$ ,  $(\cdot)_{,11} = \frac{\partial^2(\cdot)}{\partial x_1^2}$  and  $(\cdot)_{,2} = \frac{\partial(\cdot)}{\partial s}$ . The strains along the beam reference line, shown in Eq. 1.2, are related to the displacements of the beam reference line  $u_i$  and twist about the reference line  $\theta$  as

$$\hat{\epsilon} = \begin{bmatrix} \gamma_{11} \\ \kappa_1 \\ \kappa_2 \\ \kappa_3 \\ \kappa'_1 \end{bmatrix} = \begin{bmatrix} u'_1 \\ \theta' \\ -u''_3 \\ u''_2 \\ \theta'' \end{bmatrix} \tag{2.10}$$

where  $(\cdot)' = \frac{\partial(\cdot)}{\partial x_1}$ ; positive bending about the  $x_2$  axis,  $\kappa_2 > 0$ , results in vertical deflection in the negative  $x_3$  direction due to the right hand sign convention; and positive bending about the  $x_3$  axis,  $\kappa_3 > 0$ , results in horizontal deflection in the positive  $x_2$  direction.

## 2.2 Beam Strain Energy

For a piezoelectric material, the converse effect that gives the induced piezoelectric strain tensor from the application of a constant electric field under no mechanical stress is [50]

$$\varepsilon_{ij}^{(a)} = d_{kij} E_k \quad (2.11)$$

where  $\varepsilon_{ij}^{(a)}$  is the induced strain tensor in the piezoelectric materials' local frame of reference,  $d_{kij}$  is the electromechanical coupling tensor of the material and  $E_k$  is the applied electric field in the  $x_{i-local}$  direction. As it was discussed in Section 1.2.3, in the interdigitated MFC laminates, the piezoelectric fibres are polarized along their longitudinal direction. Therefore, when the electric field is applied in the fibre direction only,  $E_2 = E_3 = 0$ , and therefore

$$\varepsilon_{ij}^{(a)} = d_{1ij} E_1 \quad (2.12)$$

Only the in-plane strain tensor components,  $\varepsilon_{11}^{(a)}$ ,  $\varepsilon_{22}^{(a)}$  and  $\varepsilon_{12}^{(a)}$ , are significant due to the thinness of the shell.

The piezoelectric composite plies can have arbitrary orientations  $\vartheta$  in the laminate plane, as shown in Figure 2.2 [18].

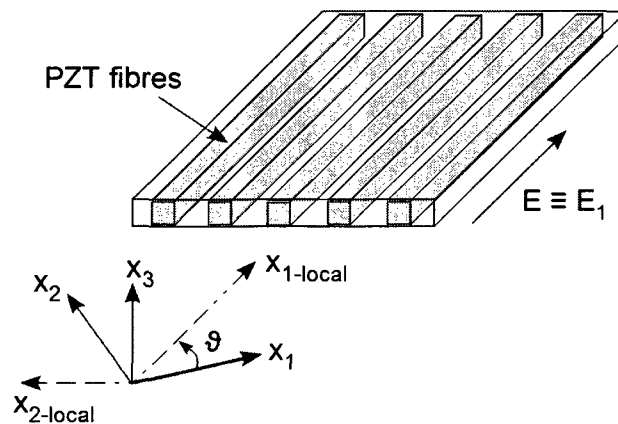


**Figure 2.2:** An MFC ply at an arbitrary orientation  $\vartheta$  from the global  $x_1$  axis with an electric field  $E$  applied in the fibre direction.

Rotating the resultant strain tensor components from the local ply reference frame to

the global Cartesian coordinate system, results in

$$\begin{bmatrix} \varepsilon_{11}^{(a)} \\ \varepsilon_{22}^{(a)} \\ \varepsilon_{12}^{(a)} \end{bmatrix} = \mathcal{R}(\vartheta) \begin{bmatrix} d_{111}E \\ d_{122}E \\ d_{112}E \end{bmatrix} = \begin{bmatrix} \bar{d}_{111}E \\ \bar{d}_{122}E \\ \bar{d}_{112}E \end{bmatrix} \quad (2.13)$$

where  $\vartheta$  is the ply angle, relative to the  $x_1$  global beam axis coordinate;  $\bar{d}_{1\alpha\beta}$  are the rotated electromechanical coupling terms;  $E$  designates the electrical field along the fibres; and  $\mathcal{R}(\vartheta)$  is the rotation matrix given by

$$\mathcal{R}(\vartheta) = \begin{bmatrix} \cos^2(\vartheta) & \sin^2(\vartheta) & -2\cos(\vartheta)\sin(\vartheta) \\ \sin^2(\vartheta) & \cos^2(\vartheta) & 2\cos(\vartheta)\sin(\vartheta) \\ \cos(\vartheta)\sin(\vartheta) & -\cos(\vartheta)\sin(\vartheta) & \cos^2(\vartheta) - \sin^2(\vartheta) \end{bmatrix} \quad (2.14)$$

The constitutive law for a general material is [51]

$$\sigma_{ij} = E^{ijkl} \varepsilon_{kl}^m \quad (2.15)$$

where  $\sigma_{ij}$  is the stress tensor,  $E^{ijkl}$  is the elasticity or Hookean tensor and  $\varepsilon_{kl}^m$  is the mechanical strain tensor. Material symmetries due to equilibrium requirements,  $\sigma_{ij} = \sigma_{ji}$  and  $\varepsilon_{kl}^m = \varepsilon_{lk}^m$ , cause  $E^{ijkl} = E^{jikl}$  and  $E^{ijkl} = E^{ijlk}$ , and result in only 36 independent constants in the elasticity tensor [52]. Consequently, the elasticity tensor may be reduced to a  $6 \times 6$  stiffness matrix  $\check{C}$  using Voigt's convention, shown in Table 2.1 [51].

The first and last two indices of  $E^{ijkl}$  are replaced by the corresponding indices given in Table 2.1, such that  $ij = m$  and  $lk = n$ , to form  $\check{C}_{mn}$ . For example,  $E^{1122} = E^{2211} = \check{C}_{12} = \check{C}_{21}$ ,  $E^{1132} = \check{C}_{14}$  and  $E^{2312} = \check{C}_{46}$ . The resulting reduced constitutive law is

$$\sigma_i = \check{C}_{ij} \varepsilon_j^m \quad (2.16)$$

**Table 2.1:** Voigt's condensed indice notation convention.

Tensor Indices	Matrix Indices
11	1
22	2
33	3
23 and 32	4
31 and 13	5
12 and 21	6

or in the expanded form,

$$\begin{bmatrix} \sigma_1 \\ \sigma_2 \\ \sigma_3 \\ \tau_{23} \\ \tau_{31} \\ \tau_{12} \end{bmatrix} = \begin{bmatrix} \check{C}_{11} & \check{C}_{12} & \check{C}_{13} & \check{C}_{14} & \check{C}_{15} & \check{C}_{16} \\ \check{C}_{12} & \check{C}_{22} & \check{C}_{23} & \check{C}_{24} & \check{C}_{25} & \check{C}_{26} \\ \check{C}_{13} & \check{C}_{23} & \check{C}_{33} & \check{C}_{34} & \check{C}_{35} & \check{C}_{36} \\ \check{C}_{14} & \check{C}_{24} & \check{C}_{34} & \check{C}_{44} & \check{C}_{45} & \check{C}_{46} \\ \check{C}_{15} & \check{C}_{25} & \check{C}_{35} & \check{C}_{45} & \check{C}_{55} & \check{C}_{56} \\ \check{C}_{16} & \check{C}_{26} & \check{C}_{36} & \check{C}_{46} & \check{C}_{56} & \check{C}_{66} \end{bmatrix} \begin{bmatrix} \varepsilon_1^m \\ \varepsilon_2^m \\ \varepsilon_3^m \\ \gamma_{23}^m \\ \gamma_{31}^m \\ \gamma_{12}^m \end{bmatrix} \quad (2.17)$$

where  $\sigma_i$  is the direct stresses in the  $x_{i-local}$  direction,  $\tau_{ij}$  are the shear stresses with respect to the  $x_{i-local}$  coordinates,  $\varepsilon_i^m$  is the direct mechanical strain in the  $x_{i-local}$  direction, and  $\gamma_{ij}^m$  are the mechanical shear strains w.r.t. the  $x_{i-local}$  coordinates.

For a general anisotropic linearly elastic 3-D body, the 3-D mechanical strain energy density per unit volume, in terms of mechanical strains  $\varepsilon_{ij}^m$  can be expressed as [52]

$$2\check{\mathcal{U}}^{(m)} = E^{ijkl} \varepsilon_{ij}^m \varepsilon_{kl}^m \quad (2.18)$$

where in the presence of mechanical strains  $\varepsilon_{ij}^m$ , and induced strains  $\varepsilon_{ij}^a$ , the total strain  $\varepsilon_{ij}$  is

$$\varepsilon_{ij} = \varepsilon_{ij}^m + \varepsilon_{ij}^a \quad (2.19)$$

Substituting Eq. 2.19 into 2.18, one gets

$$2\check{\mathcal{U}}^{(m)} = E^{ijkl}(\varepsilon_{ij} - \varepsilon_{ij}^{(a)})(\varepsilon_{kl} - \varepsilon_{kl}^{(a)}) \quad (2.20)$$

According to shell theory, the thickness stress components of a shell are much smaller than the planar stress components,  $\sigma_{i3} \approx 0$  [52]. Consequently, the 3-D mechanical strain energy can be transformed to a reduced mechanical shell energy per unit volume by minimizing the 3-D mechanical strain energy with respect to the strain component  $\varepsilon_{i3}$  in the shell thickness direction  $\xi$  as [52]

$$2\hat{\mathcal{U}}^{(m)} = D^{\alpha\beta\gamma\delta}(\varepsilon_{\alpha\beta} - \varepsilon_{\alpha\beta}^{(a)})(\varepsilon_{\gamma\delta} - \varepsilon_{\gamma\delta}^{(a)}) \quad (2.21)$$

where  $\varepsilon_{\alpha\beta}$  is the total strain tensor from Eq. 2.8,  $\varepsilon_{\alpha\beta}^{(a)}$  is the active strain tensor in the global Cartesian reference frame from Eq. 2.13, and  $D^{\alpha\beta\gamma\delta}$  are the 2-D plane-stress reduced constants given by [34, 49, 52]

$$D^{\alpha\beta\gamma\delta} = E^{\alpha\beta\gamma\delta} - \frac{E^{\alpha\beta 33} E^{\gamma\delta 33}}{E^{3333}} - H_{\mu\lambda} G^{\alpha\beta\mu} G^{\gamma\delta\lambda} \quad (2.22)$$

where

$$\begin{aligned} H_{\mu\lambda}^{-1} &= E^{\mu 3\lambda 3} - \frac{E^{\mu 333} E^{\lambda 333}}{E^{3333}} \\ G^{\alpha\beta\mu} &= E^{\alpha\beta\mu 3} - \frac{E^{\alpha\beta 33} E^{\mu 333}}{E^{3333}} \end{aligned} \quad (2.23)$$

The 2-D plane-stress reduced constants  $D^{\alpha\beta\gamma\delta}$  may be alternatively constructed from

the ply stiffness matrix  $\check{\mathbf{C}}$ . Rotating the ply stiffness matrix  $\check{\mathbf{C}}$  from the local ply reference frame to the global Cartesian coordinate system

$$\bar{\mathbf{C}} = \mathcal{R}_\sigma^{-1}(\vartheta) \check{\mathbf{C}} \mathcal{R}_\varepsilon(\vartheta) \quad (2.24)$$

where the expanded rotation matrices  $\mathcal{R}_\sigma$  and  $\mathcal{R}_\varepsilon$  are given in [38] as

$$\mathcal{R}_\sigma(\vartheta) = \begin{bmatrix} \cos^2(\vartheta) & \sin^2(\vartheta) & 0 & 0 & 0 & 2 \cos(\vartheta) \sin(\vartheta) \\ \sin^2(\vartheta) & \cos^2(\vartheta) & 0 & 0 & 0 & -2 \cos(\vartheta) \sin(\vartheta) \\ 0 & 0 & 1 & 0 & 0 & 0 \\ 0 & 0 & 0 & \cos(\vartheta) & -\sin(\vartheta) & 0 \\ 0 & 0 & 0 & \sin(\vartheta) & \cos(\vartheta) & 0 \\ -\cos(\vartheta) \sin(\vartheta) & \cos(\vartheta) \sin(\vartheta) & 0 & 0 & 0 & \cos^2(\vartheta) - \sin^2(\vartheta) \end{bmatrix}$$

$$\mathcal{R}_\varepsilon(\vartheta) = \begin{bmatrix} \cos^2(\vartheta) & \sin^2(\vartheta) & 0 & 0 & 0 & \cos(\vartheta) \sin(\vartheta) \\ \sin^2(\vartheta) & \cos^2(\vartheta) & 0 & 0 & 0 & -\cos(\vartheta) \sin(\vartheta) \\ 0 & 0 & 1 & 0 & 0 & 0 \\ 0 & 0 & 0 & \cos(\vartheta) & -\sin(\vartheta) & 0 \\ 0 & 0 & 0 & \sin(\vartheta) & \cos(\vartheta) & 0 \\ -2 \cos(\vartheta) \sin(\vartheta) & 2 \cos(\vartheta) \sin(\vartheta) & 0 & 0 & 0 & \cos^2(\vartheta) - \sin^2(\vartheta) \end{bmatrix}$$

Finally, the 2-D plane-stress reduced constants  $D^{\alpha\beta\gamma\delta}$  may be found from the relation

$$\mathbf{D} = \hat{\mathbf{C}}_1 - 2\hat{\mathbf{C}}_2\hat{\mathbf{C}}_3^{-1}\hat{\mathbf{C}}_4 + \hat{\mathbf{C}}_4^T\hat{\mathbf{C}}_3^{-1}\hat{\mathbf{C}}_4 \quad (2.25)$$

where the  $\hat{\mathbf{C}}_i$  matrices are constructed from the components of the rotated ply stiffness matrix  $\bar{\mathbf{C}}$  as

$$\begin{aligned}
\hat{\mathbf{C}}_1 &= \begin{bmatrix} \bar{C}_{11} & \bar{C}_{12} & \bar{C}_{16} \\ \bar{C}_{12} & \bar{C}_{22} & \bar{C}_{26} \\ \bar{C}_{16} & \bar{C}_{26} & \bar{C}_{66} \end{bmatrix} \\
\hat{\mathbf{C}}_2 &= \begin{bmatrix} \bar{C}_{13} & \bar{C}_{15} & \bar{C}_{14} \\ \bar{C}_{23} & \bar{C}_{25} & \bar{C}_{24} \\ \bar{C}_{36} & \bar{C}_{56} & \bar{C}_{46} \end{bmatrix} \\
\hat{\mathbf{C}}_3 &= \begin{bmatrix} \bar{C}_{33} & \bar{C}_{35} & \bar{C}_{36} \\ \bar{C}_{35} & \bar{C}_{55} & \bar{C}_{45} \\ \bar{C}_{36} & \bar{C}_{45} & \bar{C}_{44} \end{bmatrix} \\
\hat{\mathbf{C}}_4 &= \begin{bmatrix} \bar{C}_{13} & \bar{C}_{23} & \bar{C}_{36} \\ \bar{C}_{15} & \bar{C}_{25} & \bar{C}_{56} \\ \bar{C}_{14} & \bar{C}_{24} & \bar{C}_{46} \end{bmatrix}
\end{aligned} \tag{2.26}$$

The 2-D plane-stress reduced constants  $D^{\alpha\beta\gamma\delta}$  have the following resultant matrix form

$$\mathbf{D} = \begin{bmatrix} D^{1111} & D^{1122} & D^{1112} \\ D^{1122} & D^{2222} & D^{1222} \\ D^{1112} & D^{1222} & D^{1212} \end{bmatrix} \tag{2.27}$$

Substituting Eq. 2.8 into Eq. 2.21 and integrating through the thickness  $h$  and along the entire cross section contour  $s$  gives the mechanical shell strain energy per unit length of the beam as

$$2\tilde{\mathcal{U}}^{(m)} = \int_{\Sigma} \int_{-\frac{h}{2}}^{\frac{h}{2}} D^{\alpha\beta\gamma\delta} (\gamma_{\alpha\beta} + \xi\rho_{\alpha\beta} - \varepsilon_{\alpha\beta}^{(a)}) (\gamma_{\gamma\delta} + \xi\rho_{\gamma\delta} - \varepsilon_{\gamma\delta}^{(a)}) d\xi ds \tag{2.28}$$

Substituting Eq. 2.13 into Eq. 2.28 yields

$$2\tilde{\mathcal{U}}^{(m)} = \int_{\Sigma_s} \int_{-\frac{h}{2}}^{\frac{h}{2}} D^{\alpha\beta\gamma\delta} (\gamma_{\alpha\beta} + \xi\rho_{\alpha\beta} - \bar{d}_{1\alpha\beta}E) (\gamma_{\gamma\delta} + \xi\rho_{\gamma\delta} - \bar{d}_{1\gamma\delta}E) d\xi ds \quad (2.29)$$

Expanding the integrand of Eq. 2.29, grouping the shell strain terms into two vectors,  $\boldsymbol{\psi}^T = \begin{bmatrix} \gamma_{11} & h\rho_{11} & h\rho_{12} \end{bmatrix}$  and  $\boldsymbol{\phi}^T = \begin{bmatrix} 2\gamma_{12} & \gamma_{22} & h\rho_{22} \end{bmatrix}$ , and integrating through the shell thickness, as done in Appendix A.1, gives

$$2\mathcal{U}^{(m)} = \int_{\Sigma_s} (\boldsymbol{\psi}^T \mathbf{Q} \boldsymbol{\psi} + 2\boldsymbol{\phi}^T \mathbf{S} \boldsymbol{\psi} + \boldsymbol{\phi}^T \mathbf{P} \boldsymbol{\phi} - 2\boldsymbol{\psi}^T \mathbf{H} - 2\boldsymbol{\phi}^T \mathbf{G} + \aleph(E)) ds \quad (2.30)$$

where the  $\mathbf{Q}$ ,  $\mathbf{S}$  and  $\mathbf{P}$  laminate elastic matrices, the  $\mathbf{H}$  and  $\mathbf{G}$  laminate electromechanical coupling matrices, and the  $\aleph(E)$  quadratic electromechanical field expression are given in Appendix A.1.

## 2.3 Application of the VAM to Active OCSTWB

### 2.3.1 Phantom Step

As discussed in Section 1.2.2, the goal of the VAM is to construct an energy functional of  $\mathcal{O}(\epsilon^2)$  in terms of the displacements at the beam reference line, Eq. 2.10. The phantom step begins by dropping all terms differentiated with respect to the axial coordinate in the general strain field, Eqs. 2.9. The remaining non-zero strain terms are

$$\begin{aligned}
2\gamma_{12} &= v_{1,2} \\
\rho_{12} &= \frac{v_{1,2}}{4R} \\
\gamma_{22} &= v_{2,2} + \frac{v_3}{R} \\
\rho_{22} &= v_{3,22} - \left(\frac{v_2}{R}\right)_{,2}
\end{aligned} \tag{2.31}$$

Strain terms differentiated with respect to the axial coordinate  $x_1$  are much smaller than strain terms differentiated with respect to the transverse coordinate  $s$  since

$$\mathcal{O}((\cdot)_{,1} = (\cdot)') \approx \mathcal{O}\left(\frac{(\cdot)}{l}\right) \quad \text{and} \quad \mathcal{O}((\cdot)_{,2} = (\cdot)') \approx \mathcal{O}\left(\frac{(\cdot)}{a}\right) \tag{2.32}$$

and  $\mathcal{O}(a/l) \ll 1$  (Eqs. 1.4). Substitution of the reduced strain field, Eqs. 2.31, into the mechanical shell strain energy functional, Eq. 2.30, results in an energy functional whose minimum occurs when all the strains are zero,  $\gamma_{12} = \rho_{12} = \gamma_{22} = \rho_{22} = 0$ . Alternatively, this result may be found by substituting the curvilinear displacements, Eqs. 2.7 into the reduced strain field, Eqs. 2.31 and determining the order of the strain terms with respect to the small parameters of Eqs. 1.4, yielding

$$\begin{aligned}
2\gamma_{12} &= \underbrace{\hat{u}_{1,2}}_{\mathcal{O}\left(\epsilon\left(\frac{a}{l}\right)^{-1}\right)} \\
h\rho_{12} &= \underbrace{\frac{h\hat{u}_{1,2}}{4R}}_{\mathcal{O}\left(\epsilon\left(\frac{a}{l}\right)^{-1}\left(\frac{h}{a}\right)\right)} \\
\gamma_{22} &= \underbrace{(\hat{u}_2\dot{x}_2 + \hat{u}_3\dot{x}_3)_{,2} + \frac{\hat{u}_2\dot{x}_3 - \hat{u}_3\dot{x}_2}{R}}_{\mathcal{O}\left(\epsilon\left(\frac{a}{l}\right)^{-2}\right)} \\
h\rho_{22} &= \underbrace{h(\hat{u}_2\dot{x}_3 - \hat{u}_3\dot{x}_2)_{,22} - h\left(\frac{(\hat{u}_2\dot{x}_2 + \hat{u}_3\dot{x}_3)}{R}\right)_{,2}}_{\mathcal{O}\left(\epsilon\left(\frac{a}{l}\right)^{-2}\left(\frac{h}{a}\right)\right)} \tag{2.33}
\end{aligned}$$

where the classical strain measures, introduced in Eq. 1.2, are assumed to be the largest strains present in the beam and of the same order, such that

$$\mathcal{O}(u'_1) \approx \mathcal{O}(h\theta') \approx \mathcal{O}(-au''_3) \approx \mathcal{O}(au''_2) \approx \mathcal{O}(\epsilon) \tag{2.34}$$

This assumption gives a general solution since if some strain terms are of higher order than the others, there will exist unnecessary, negligible terms in the energy solution of order higher than  $\mathcal{O}(\epsilon^2)$ . Additionally, the radius of curvature  $R$ , the characteristic cross sectional dimension  $a$ , and the two Cartesian cross sectional coordinates  $x_2$  and  $x_3$  are assumed to be of the same order, such that

$$\mathcal{O}(R) \approx \mathcal{O}(a) \approx \mathcal{O}(x_2) \approx \mathcal{O}(x_3). \tag{2.35}$$

To determine the order of the terms in Eqs. 2.33,  $\mathcal{O}(\hat{u}_1) \approx \mathcal{O}(u_1)$ ,  $\mathcal{O}(\hat{u}_2) \approx \mathcal{O}(u_2)$  and  $\mathcal{O}(\hat{u}_3) \approx \mathcal{O}(u_3)$  are assumed, and Eqs. 2.32, 2.34 and 2.35 may subsequently be used. For example, the order of the  $h\rho_{12}$  strain term is found by

$$u'_1 \approx \mathcal{O}(\epsilon) \rightarrow u_1 \approx \mathcal{O}(\epsilon l) \rightarrow u_{1,2} \approx \mathcal{O}\left(\epsilon \frac{l}{a}\right) \rightarrow \frac{h\hat{u}_{1,2}}{4R} \approx \mathcal{O}\left(\epsilon \left(\frac{a}{l}\right)^{-1} \frac{h}{a}\right) \quad (2.36)$$

As seen in Eqs. 2.33, all of the terms have order greater than  $\mathcal{O}(\epsilon)$  with respect to the small parameters and are consequently “phantom” terms that must be eliminated by setting the strain terms to zero, such that

$$0 = v_{1,2} \quad (2.37)$$

$$0 = \frac{v_{1,2}}{4R} \quad (2.38)$$

$$0 = v_{2,2} + \frac{v_3}{R} \quad (2.39)$$

$$0 = v_{3,22} - \left(\frac{v_2}{R}\right)_{,2} \quad (2.40)$$

Integrating Eq. 2.37 or 2.38 with respect to  $s$  and comparing with the first curvilinear relation of Eqs. 2.7, gives

$$v_1 = C(x_1) = u_1 \quad (2.41)$$

Also, integrating Eq. 2.40 with respect to  $s$ , yields

$$v_{3,2} - \left(\frac{v_2}{R}\right) = -\theta(x_1) \quad (2.42)$$

where  $C$  and  $\theta$  are constants of integration with respect to  $s$  only.

Rearranging Eq. 2.39 to isolate  $v_3$  and substituting the expression for  $v_3$  into Eq. 2.42, gives

$$-(Rv_{2,2})_{,2} - \left(\frac{v_2}{R}\right) = -\theta(x_1) \quad (2.43)$$

Using Eqs. 2.3 and 2.6, it can be verified that the solution of Eq. 2.43 is given by

$$v_2 = u_2\dot{x}_2 + u_3\dot{x}_3 + \theta r_n \quad (2.44)$$

Substitution of Eq. 2.44 into Eq. 2.39 gives the solution for  $v_3$  as

$$v_3 = u_2\dot{x}_3 - u_3\dot{x}_2 - \theta r_\tau \quad (2.45)$$

Eqs. 2.41, 2.44 and 2.45 describe the rigid body displacement of the cross section and are repeated here as

$$\begin{aligned} v_1 &= u_1 \\ v_2 &= u_2\dot{x}_2 + u_3\dot{x}_3 + \theta r_n \\ v_3 &= u_2\dot{x}_3 - u_3\dot{x}_2 - \theta r_\tau \end{aligned} \quad (2.46)$$

Using Eqs. 2.7, the rigid body displacement field can be expressed in Cartesian coordinates as

$$\begin{aligned} \hat{u}_1 &= u_1 \\ \hat{u}_2 &= u_2 - x_3\theta \\ \hat{u}_3 &= u_3 + x_2\theta \end{aligned} \quad (2.47)$$

This completes the phantom step of the VAM and gives the first iteration of a displace-

ment field, and thus a strain field and energy functional as Eqs. 2.9 and 2.30, respectively, in terms of the displacements and twist at the beam reference line:  $u_1$ ,  $u_2$ ,  $u_3$  and  $\theta$ . Subsequent iterations of the VAM will identify cross sectional warping terms in the displacement field.

### 2.3.2 First Perturbation

Perturbing the rigid body displacement field by unknown warping terms  $\hat{w}_1$ ,  $\hat{w}_2$  and  $\hat{w}_3$  yields

$$\begin{aligned} v_1 &= u_1 + \hat{w}_1 \\ v_2 &= u_\alpha \dot{x}_\alpha + \theta r_n + \hat{w}_2 \\ v_3 &= u_2 \dot{x}_3 - u_3 \dot{x}_2 - \theta r_\tau + \hat{w}_3 \end{aligned} \tag{2.48}$$

Substituting the perturbed displacement field, Eqs. 2.48 into the general strain field, Eqs. 2.9 and using the relations given in Eqs. 2.3 and 2.6, as done in Appendix A.2, yields

$$\begin{aligned}
\gamma_{11} &= \underbrace{u'_1}_{\mathcal{O}(\epsilon)} + \underbrace{\hat{w}_{1,1}}_{\mathcal{O}(\epsilon)} \\
2\gamma_{12} &= \underbrace{\dot{x}_2 u'_2}_{\mathcal{O}(\epsilon(\frac{a}{l})^{-1})} + \underbrace{\dot{x}_3 u'_3}_{\mathcal{O}(\epsilon(\frac{a}{l})^{-1})} + \underbrace{r_n \theta'}_{\mathcal{O}(\epsilon(\frac{h}{a})^{-1})} + \underbrace{\hat{w}_{1,2}}_{\mathcal{O}(\epsilon(\frac{a}{l})^{-1})} + \underbrace{\hat{w}_{2,1}}_{\mathcal{O}(\epsilon(\frac{a}{l})^{-1})(\frac{h}{a})^{-1}} \\
\gamma_{22} &= \underbrace{\hat{w}_{2,2}}_{\mathcal{O}(\epsilon(\frac{h}{a})^{-1})} + \underbrace{\frac{\hat{w}_3}{R}}_{\mathcal{O}(\epsilon(\frac{h}{a})^{-1})} \\
h\rho_{11} &= h \left( \underbrace{\dot{x}_3 u''_2}_{\mathcal{O}(\epsilon(\frac{h}{a}))} - \underbrace{\dot{x}_2 u''_3}_{\mathcal{O}(\epsilon(\frac{h}{a}))} - \underbrace{r_\tau \theta''}_{\mathcal{O}(\epsilon(\frac{a}{l}))} + \underbrace{\hat{w}_{3,11}}_{\mathcal{O}(\epsilon(\frac{a}{l})^2)} \right) \\
h\rho_{12} &= h \left( \frac{1}{4R} \left( \underbrace{\dot{x}_\alpha u'_\alpha}_{\mathcal{O}(\epsilon(\frac{h}{a})(\frac{a}{l})^{-1})} + \underbrace{r_n \theta'}_{\mathcal{O}(\epsilon)} - \underbrace{\hat{w}_{1,2}}_{\mathcal{O}(\epsilon(\frac{a}{l})^{-1})(\frac{h}{a}))} \right) - \underbrace{\theta'}_{\mathcal{O}(\epsilon)} + \underbrace{\hat{w}_{3,12}}_{\mathcal{O}(\epsilon(\frac{a}{l}))} - \underbrace{\frac{3}{4R} \hat{w}_{2,1}}_{\mathcal{O}(\epsilon(\frac{a}{l}))} \right) \\
h\rho_{22} &= h \left( \underbrace{\hat{w}_{3,2}}_{\mathcal{O}(\epsilon)} - \underbrace{\frac{\hat{w}_2}{R}}_{\mathcal{O}(\epsilon)} \right),_2 \tag{2.49}
\end{aligned}$$

where the orders given below the terms include the contributions of the coefficients; the orders of the terms with the orders given in regular font are determined directly using Eqs. 2.32, 2.34 and 2.35; and the orders of the terms with the orders given in bold font are determined during the following minimization of the energy functional.

The perturbed strain field, Eqs. 2.49, is substituted into the mechanical strain energy functional, Eq. 2.30, which is subsequently minimized with respect to the perturbation terms  $\hat{w}_1$ ,  $\hat{w}_2$  and  $\hat{w}_3$ . The minimization is done by taking the variation of the energy functional and setting it to zero, as

$$\delta (\mathcal{U}^{(m)}) = \int_{\Sigma} \left( \left( \hat{F} \right)_{,\hat{w}_1} \delta \hat{w}_1 + \left( \hat{F} \right)_{,\hat{w}_2} \delta \hat{w}_2 + \left( \hat{F} \right)_{,\hat{w}_3} \delta \hat{w}_3 \right) ds = 0 \quad (2.50)$$

where  $\hat{F}$  is the integrand of the energy functional, which contains quadratic strain terms, i.e.  $\gamma_{12}^2$ , and cross strain terms, i.e.  $\gamma_{12}\rho_{11}$ , such that

$$\begin{aligned} \hat{F} = \hat{F} & (\gamma_{11}^2, \gamma_{12}^2, \gamma_{22}^2, \rho_{11}^2, \rho_{12}^2, \rho_{22}^2, \gamma_{11}\gamma_{12}, \gamma_{11}\gamma_{22}, \\ & \gamma_{11}\rho_{11}, \gamma_{11}\rho_{12}, \gamma_{11}\rho_{22}, \gamma_{12}\gamma_{22}, \gamma_{12}\rho_{11}, \gamma_{12}\rho_{12}, \\ & \gamma_{12}\rho_{22}, \gamma_{22}\rho_{11}, \gamma_{22}\rho_{12}, \gamma_{22}\rho_{22}, \rho_{11}\rho_{12}, \rho_{11}\rho_{22}, \rho_{12}\rho_{22}) \end{aligned} \quad (2.51)$$

The perturbation terms must be chosen such that they minimize the energy functional, Eq. 2.50, as follows. In the expression for  $2\gamma_{12}$  in Eqs. 2.49, the three excessively large phantom terms  $\dot{x}_2 u'_2$ ,  $\dot{x}_3 u'_3$  and  $r_n \theta'$  must be eliminated by a perturbation term. Of the two perturbation terms present in the  $2\gamma_{12}$  expression,  $\hat{w}_{1,2}$  is the appropriate one to use since  $\hat{w}_{2,1}$  must be of a higher order than  $\hat{w}_{1,2}$  as terms differentiated with respect to the axial coordinate  $x_1$  are smaller than terms differentiated with respect to the contour coordinate  $s$ . Additionally, if  $\hat{w}_{2,1}$  was used to eliminate the phantom terms, it would produce excessively large terms in other strain expressions, in which case the energy functional could not be minimized. For the  $\hat{w}_{1,2}$  term to eliminate the excessively large terms in the expression for  $2\gamma_{12}$ , it must be set to

$$\hat{w}_{1,2} = -u'_\alpha \dot{x}_\alpha - r_n \theta' \quad (2.52)$$

Defining a quantity called the sectorial coordinate as [26, 53]

$$\eta = \int_{s_0}^s r_n ds \quad (2.53)$$

where  $s_0$  is the origin of the contour, allows the  $\hat{w}_{1,1}$  term in the  $\gamma_{11}$  expression to be written as

$$\hat{w}_{1,1} = -u''_{\alpha} x_{\alpha} - \eta \theta'' \quad (2.54)$$

There are no other known phantom terms that need to be eliminated. At this point, it is sufficient to determine only the orders of the remaining perturbation terms. Once the strain field has been constructed to  $\mathcal{O}(\epsilon)$  accuracy, the values of the unknown strain terms, containing the unknown perturbation terms, will be found in a single minimization of the energy functional with respect to the unknown strain terms. The lowest order—or leading order—perturbation terms remaining are found in the expression for  $\gamma_{22}$  in Eqs. 2.49. Comparing the order of the perturbation terms found in  $\gamma_{22}$  and  $h\rho_{22}$ , it can be seen that  $\gamma_{22}$  is excessively large relative to  $h\rho_{22}$ , such that

$$\gamma_{22} = \left(\frac{h}{a}\right)^{-1} h\rho_{22} \quad (2.55)$$

As all the remaining unknown perturbation terms are of higher order than those found in the expression for  $\gamma_{22}$  in Eqs. 2.49, the only way to minimize the energy functional is to set the  $\gamma_{22}$  strain term to zero, such that

$$\gamma_{22} = \hat{w}_{2,2} + \frac{\hat{w}_3}{R} = 0 \quad (2.56)$$

where  $\hat{w}_2$  and  $\hat{w}_3$  must consequently be of the same order. Of the remaining perturbation terms, the two leading order ones are found in the  $h\rho_{22}$  strain expression of Eqs. 2.49. During the minimization, these leading order terms will produce terms in the energy functional that are quadratic in them, i.e.  $(\dots)(h\hat{w}_{3,22})^2$ , and terms that are a cross between them and other terms, i.e.  $(\dots)(h\hat{w}_{3,22})(h\theta')$ , as seen in Eq. 2.51. In order to minimize the energy functional, the order of the terms quadratic in the leading order

perturbation terms must be of the same order as those that are a cross between the leading order perturbation terms and the lowest order known terms that have not been eliminated. Consequently, the leading order perturbation terms must be of the same order as the largest non-phantom known terms in the strain field, Eqs. 2.49, such that

$$\mathcal{O}(h\hat{w}_{3,22}) = \mathcal{O}\left(-h\left(\frac{\hat{w}_2}{R}\right)_{,2}\right) = \mathcal{O}(u'_1) = \mathcal{O}\left(\frac{h}{4R}r_n\theta'\right) = \mathcal{O}(h\theta') = \mathcal{O}(\epsilon) \quad (2.57)$$

The orders of the remaining perturbation terms are found using the relations given in Eqs. 2.32, 2.34 and 2.35. As will be seen, additional perturbations of the displacement field will not produce any more phantom terms in the strain field; consequently, the zeroth approximation is now complete.

### 2.3.3 Second Perturbation

Perturbing the previous displacement field by a second set of unknown warping terms  $w_1$ ,  $w_2$  and  $w_3$ , yields

$$\begin{aligned} v_1 &= u_1 + \hat{w}_1 + w_1 \\ v_2 &= u_\alpha \dot{x}_\alpha + \theta r_n + \hat{w}_2 + w_2 \\ v_3 &= u_2 \dot{x}_3 - u_3 \dot{x}_2 - \theta r_\tau + \hat{w}_3 + w_3 \end{aligned} \quad (2.58)$$

Substituting the perturbed displacement field, Eqs. 2.58 into the general strain field, Eqs. 2.9, and using the relations given in Eqs. 2.3 and 2.6, as done similarly for the first perturbation in Appendix A.2, yields

$$\begin{aligned}
\gamma_{11} &= \underbrace{u_1'}_{\mathcal{O}(\epsilon)} - \underbrace{x_\alpha u_\alpha''}_{\mathcal{O}(\epsilon)} - \underbrace{\eta\theta'}_{\mathcal{O}\left(\epsilon\left(\frac{a}{l}\right)\left(\frac{h}{a}\right)^{-1}\right)} + \underbrace{w_{1,1}}_{\mathcal{O}\left(\epsilon\left(\frac{a}{l}\right)\right)} \\
2\gamma_{12} &= \underbrace{\hat{w}_{2,1}}_{\mathcal{O}\left(\epsilon\left(\frac{a}{l}\right)\left(\frac{h}{a}\right)^{-1}\right)} + \underbrace{w_{1,2}}_{\mathcal{O}(\epsilon)} + \underbrace{w_{2,1}}_{\mathcal{O}\left(\epsilon\left(\frac{a}{l}\right)\right)} \\
\gamma_{22} &= \underbrace{w_{2,2}}_{\mathcal{O}(\epsilon)} + \underbrace{\frac{w_3}{R}}_{\mathcal{O}(\epsilon)} \\
h\rho_{11} &= h \left( \underbrace{\dot{x}_3 u_2''}_{\mathcal{O}\left(\epsilon\left(\frac{h}{a}\right)\right)} - \underbrace{\dot{x}_2 u_3''}_{\mathcal{O}\left(\epsilon\left(\frac{h}{a}\right)\right)} - \underbrace{r_\tau \theta''}_{\mathcal{O}\left(\epsilon\left(\frac{a}{l}\right)\right)} + \underbrace{\hat{w}_{3,11}}_{\mathcal{O}\left(\epsilon\left(\frac{a}{l}\right)^2\right)} + \underbrace{w_{3,11}}_{\mathcal{O}\left(\epsilon\left(\frac{a}{l}\right)^2\left(\frac{h}{a}\right)\right)} \right) \\
h\rho_{12} &= h \left[ \underbrace{\frac{w_{1,2}}{4R}}_{\mathcal{O}\left(\epsilon\left(\frac{h}{a}\right)\right)} - \underbrace{\theta'}_{\mathcal{O}(\epsilon)} + \underbrace{\hat{w}_{3,12}}_{\mathcal{O}\left(\epsilon\left(\frac{a}{l}\right)\right)} + \underbrace{w_{3,12}}_{\mathcal{O}\left(\epsilon\left(\frac{a}{l}\right)\left(\frac{h}{a}\right)\right)} - \frac{3}{4R} \left( \underbrace{\hat{w}_{2,1}}_{\mathcal{O}\left(\epsilon\left(\frac{a}{l}\right)\right)} + \underbrace{w_{2,1}}_{\mathcal{O}\left(\epsilon\left(\frac{a}{l}\right)\left(\frac{h}{a}\right)\right)} \right) \right] \\
h\rho_{22} &= h \left[ \underbrace{\hat{w}_{3,2}}_{\mathcal{O}(\epsilon)} + \underbrace{w_{3,2}}_{\mathcal{O}\left(\epsilon\left(\frac{h}{a}\right)\right)} - \frac{1}{R} \left( \underbrace{\hat{w}_2}_{\mathcal{O}(\epsilon)} + \underbrace{w_2}_{\mathcal{O}\left(\epsilon\left(\frac{h}{a}\right)\right)} \right) \right]_{,2} \tag{2.59}
\end{aligned}$$

Unlike in the case of the first perturbation of the strain field, none of the terms of known order are phantom terms. Consequently, this indicates that the first perturbation completed the zeroth order approximation, and the present, second perturbation corresponds to the first order approximation. By inspection of Eqs. 2.59, the leading order perturbation terms of unknown order are  $w_{1,2}$ ,  $w_{2,2}$  and  $\frac{w_3}{R}$ , which are found in the expressions for  $2\gamma_{12}$  and  $\gamma_{22}$ . These terms must have the same order as the largest known order terms in the strain field, Eqs. 2.59, such that

$$\begin{aligned}
\mathcal{O}(w_{1,2}) &= \mathcal{O}(w_{2,2}) = \mathcal{O}\left(\frac{w_3}{R}\right) = \mathcal{O}(u'_1) = \mathcal{O}(x_\alpha u''_\alpha) \\
&= \mathcal{O}(h\theta') = \mathcal{O}(h\hat{w}_{3,22}) = \mathcal{O}\left(\left(\frac{h\hat{w}_2}{R}\right)_{,2}\right) = \mathcal{O}(\epsilon)
\end{aligned} \tag{2.60}$$

As done before, the orders of the remaining perturbation terms are found using the relations given in Eqs. 2.32, 2.34 and 2.35. As will be seen, additional perturbations of the displacement field will not produce any more terms in the strain field of  $\mathcal{O}(\epsilon)$ ; consequently, the strain field given in Eqs. 2.59 has asymptotically converged to  $\mathcal{O}(\epsilon)$  accuracy. A beam energy functional of  $\mathcal{O}(\epsilon^2)$  accuracy can now be found using the present strain field. For a linear cross-sectional theory, the terms of  $\mathcal{O}(\epsilon)$  in the strain field, Eqs. 2.59, are retained, yielding

$$\begin{aligned}
\bar{\gamma}_{11} &= u'_1 - x_\alpha u''_\alpha \\
2\bar{\gamma}_{12} &= w_{1,2} \\
\bar{\gamma}_{22} &= w_{2,2} + \frac{w_3}{R} \\
h\bar{\rho}_{11} &= 0 \\
h\bar{\rho}_{12} &= -h\theta' \\
h\bar{\rho}_{22} &= h\left(\hat{w}_{3,2} - \frac{\hat{w}_2}{R}\right)_{,2}
\end{aligned} \tag{2.61}$$

where  $\bar{\gamma}_{11}$ ,  $\bar{\gamma}_{12}$ ,  $\bar{\gamma}_{22}$ ,  $\bar{\rho}_{11}$ ,  $\bar{\rho}_{12}$  and  $\bar{\rho}_{22}$  are the strains containing the  $\mathcal{O}(\epsilon)$  accurate terms. The corresponding strain term vectors, used in Eq. 2.30, become  $\bar{\psi}^T = \begin{bmatrix} \bar{\gamma}_{11} & h\bar{\rho}_{11} & h\bar{\rho}_{12} \end{bmatrix}$  and  $\bar{\phi}^T = \begin{bmatrix} 2\bar{\gamma}_{12} & \bar{\gamma}_{22} & h\bar{\rho}_{22} \end{bmatrix}$ , where  $\bar{\psi}$  contains all the known  $\mathcal{O}(\epsilon)$  strain terms and  $\bar{\phi}$  contains all the unknown  $\mathcal{O}(\epsilon)$  strain terms. Substituting the  $\mathcal{O}(\epsilon)$  accurate strains into

Eq. 2.30, yields

$$2\mathcal{U}^{(m)} = \int_{\Sigma_s} (\bar{\psi}^T \mathbf{Q} \bar{\psi} + 2\bar{\phi}^T \mathbf{S} \bar{\psi} + \bar{\phi}^T \mathbf{P} \bar{\phi} - 2\bar{\psi}^T \mathbf{H} - 2\bar{\phi}^T \mathbf{G} + \aleph(E)) \, ds \quad (2.62)$$

Starting with the classical strains due to axial, torsional and bending actions, the vector of strains given in Eq. 2.10, becomes

$$\bar{\epsilon} = \begin{bmatrix} u'_1 \\ \theta' \\ -u''_3 \\ u''_2 \end{bmatrix} \quad (2.63)$$

The vector of known strains  $\bar{\psi}$  can be expressed in terms of  $\bar{\epsilon}$ , Eq. 2.63, as

$$\bar{\psi} = \mathbf{T} \bar{\epsilon} \quad (2.64)$$

where

$$\bar{\psi} = \begin{bmatrix} \bar{\gamma}_{11} \\ h\bar{\rho}_{11} \\ h\bar{\rho}_{12} \end{bmatrix} = \begin{bmatrix} u'_1 - x_2 u''_2 - x_3 u''_3 \\ 0 \\ -h\theta' \end{bmatrix} = \begin{bmatrix} 1 & 0 & x_3 & -x_2 \\ 0 & 0 & 0 & 0 \\ 0 & -h & 0 & 0 \end{bmatrix} \begin{bmatrix} u'_1 \\ \theta' \\ -u''_3 \\ u''_2 \end{bmatrix} \quad (2.65)$$

and consequently,

$$\mathbf{T}_{general} = \begin{bmatrix} 1 & 0 & x_3 & -x_2 \\ 0 & 0 & 0 & 0 \\ 0 & -h & 0 & 0 \end{bmatrix} \quad (2.66)$$

In the special case of a horizontal strip, shown in Figure 2.3,  $x_3 \approx 0$  due to the thinness in the  $x_3$  direction, causing the  $-x_3 u_3''$  term of  $\gamma_{11}$  to become less than  $\mathcal{O}(\epsilon)$  [19]. In addition, the previously higher order  $-h x_2 u_3''$  term of  $\rho_{11}$  becomes  $\mathcal{O}(\epsilon)$  since  $u_3''$  is large for a strip, yielding

$$\mathbf{T}_{horiz. strip} = \begin{bmatrix} 1 & 0 & 0 & -x_2 \\ 0 & 0 & \dot{x}_2 h & 0 \\ 0 & -h & 0 & 0 \end{bmatrix} \quad (2.67)$$

where  $|\dot{x}_2| = 1$  since the contour  $s$  is parallel to the  $x_2$  axis. A similar derivation may be used to find  $\mathbf{T}$  for a vertical strip.

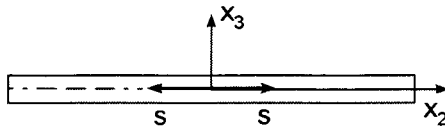


**Figure 2.3:** Cross section of a horizontal strip with reference axes  $x_2$  and  $x_3$ , and the contour coordinate  $s$ .

Substituting Eq. 2.64 into Eq. 2.62 yields,

$$2\mathcal{U}^{(m)} = \int_{\Sigma_s} (\bar{\epsilon}^T \mathbf{T}^T \mathbf{Q} \mathbf{T} \bar{\epsilon} + 2\bar{\phi}^T \mathbf{S} \mathbf{T} \bar{\epsilon} + \bar{\phi}^T \mathbf{P} \bar{\phi} - 2\bar{\epsilon}^T \mathbf{T}^T \mathbf{H} - 2\bar{\phi}^T \mathbf{G} + \mathfrak{N}(E)) ds \quad (2.68)$$

Next, the energy functional, Eq. 2.68, is minimized with respect to the unknown strains  $\bar{\phi}$ , as

$$\begin{aligned}
\delta (2\mathcal{U}^{(m)}) &= 0 \\
(2\mathbf{S}\mathbf{T}\bar{\boldsymbol{\epsilon}} + 2\mathbf{P}\bar{\boldsymbol{\phi}} - 2\mathbf{G}) \delta\bar{\boldsymbol{\phi}} &= 0 \\
\bar{\boldsymbol{\phi}} &= -\mathbf{P}^{-1}\mathbf{S}\mathbf{T}\bar{\boldsymbol{\epsilon}} + \mathbf{P}^{-1}\mathbf{G}
\end{aligned} \tag{2.69}$$

Unlike for the case of closed cross section thin wall beams, there are no constraints that need to be applied to the warping perturbation terms for OCSTWB when minimizing the above beam energy functional. Substituting Eq. 2.69 into Eq. 2.68 and simplifying, yields

$$\begin{aligned}
2\mathcal{U}^{(m)} &= \int_{\Sigma_s} \left[ \bar{\boldsymbol{\epsilon}}^T \mathbf{T}^T \mathbf{Q} \mathbf{T} \bar{\boldsymbol{\epsilon}} - \bar{\boldsymbol{\epsilon}}^T \mathbf{T}^T \mathbf{S}^T \mathbf{P}^{-1} \mathbf{S} \mathbf{T} \bar{\boldsymbol{\epsilon}} + 2 (\mathbf{G}^T \mathbf{P}^{-1} \mathbf{S} \mathbf{T} \bar{\boldsymbol{\epsilon}})^T \right. \\
&\quad \left. - 2 (\mathbf{H}^T \mathbf{T} \bar{\boldsymbol{\epsilon}})^T - \mathbf{G}^T \mathbf{P}^{-1} \mathbf{G} + \mathfrak{N}(E) \right] ds
\end{aligned} \tag{2.70}$$

where the relation  $\mathbf{P} = \mathbf{P}^T$ , inferred from Eqs. A.8, has been used, and  $(\mathbf{G}^T \mathbf{P}^{-1} \mathbf{S} \mathbf{T} \bar{\boldsymbol{\epsilon}})^T = \mathbf{G}^T \mathbf{P}^{-1} \mathbf{S} \mathbf{T} \bar{\boldsymbol{\epsilon}}$  since it is a scalar quantity. Terms involving mechanical strains  $\mathbf{T}\bar{\boldsymbol{\epsilon}}$  only, constitute the non-active structural component of the beam energy, whereas terms involving the electromechanical coupling matrices  $\mathbf{G}$  and  $\mathbf{H}$ , constitute the active component of the beam energy due to piezoelectric actuation. The final strain energy of  $\mathcal{O}(\epsilon^2)$  accuracy has the form,

$$2\mathcal{U}^{(m)} = 2\mathcal{U}^{structural} + 2\mathcal{U}^{(a)} + 2\mathcal{U}^{quadratic\ E\text{-field}} \tag{2.71}$$

where

$$\begin{aligned}
2\mathcal{U}^{structural} &= \int_{\Sigma_s} [\bar{\boldsymbol{\epsilon}}^T \mathbf{T}^T (\mathbf{Q} - \mathbf{S}^T \mathbf{P}^{-1} \mathbf{S}) \mathbf{T} \bar{\boldsymbol{\epsilon}}] \, ds \\
2\mathcal{U}^{(a)} &= \int_{\Sigma_s} \left[ 2 (\mathbf{G}^T \mathbf{P}^{-1} \mathbf{S} \mathbf{T} \bar{\boldsymbol{\epsilon}})^T - 2 (\mathbf{H}^T \mathbf{T} \bar{\boldsymbol{\epsilon}})^T \right] \, ds \\
2\mathcal{U}^{quadratic \, E\text{-field}} &= \int_{\Sigma_s} [-\mathbf{G}^T \mathbf{P}^{-1} \mathbf{G} + \aleph(E)] \, ds \tag{2.72}
\end{aligned}$$

The current, second perturbation of the displacement field gives the first order approximation to both the strain field and energy functional. As seen in the strain field, Eqs. 2.59, there are two terms,  $\eta\theta'$  and  $\hat{w}_{2,1}$ , in the expressions for  $\gamma_{11}$  and  $2\gamma_{12}$ , respectively, that are  $\mathcal{O}\left(\epsilon \left(\frac{a}{l}\right) \left(\frac{h}{a}\right)^{-1}\right)$ . These terms correspond to the Vlasov deformation mode and can be significant for OCSTWB. A third perturbation of the displacement field will identify additional terms of  $\mathcal{O}\left(\epsilon \left(\frac{a}{l}\right) \left(\frac{h}{a}\right)^{-1}\right)$  in the strain field, and by repeating the minimization procedure above, energy terms of  $\mathcal{O}\left(\epsilon^2 \left(\frac{a}{l}\right) \left(\frac{h}{a}\right)^{-1}\right)$  and  $\mathcal{O}\left(\epsilon^2 \left(\frac{a}{l}\right)^2 \left(\frac{h}{a}\right)^{-2}\right)$  will be found and added to the beam energy.

### 2.3.4 Third Perturbation

Perturbing the previous displacement field by a third set of unknown warping terms  $\tilde{w}_1$ ,  $\tilde{w}_2$  and  $\tilde{w}_3$ , yields

$$\begin{aligned}
v_1 &= \underbrace{u_1}_{\mathcal{O}(\epsilon l)} + \underbrace{\hat{w}_1}_{\mathcal{O}(\epsilon l)} + \underbrace{w_1}_{\mathcal{O}(\epsilon a)} + \underbrace{\tilde{w}_1}_{\mathcal{O}\left(\epsilon a \left(\frac{a}{l}\right) \left(\frac{h}{a}\right)^{-1}\right)} \\
v_2 &= \underbrace{u_\alpha \dot{x}_\alpha}_{\mathcal{O}\left(\epsilon l \left(\frac{a}{l}\right)^{-1}\right)} + \underbrace{\theta r_n}_{\mathcal{O}\left(\epsilon l \left(\frac{h}{a}\right)^{-1}\right)} + \underbrace{\hat{w}_2}_{\mathcal{O}\left(\epsilon a \left(\frac{h}{a}\right)^{-1}\right)} + \underbrace{w_2}_{\mathcal{O}(\epsilon a)} + \underbrace{\tilde{w}_2}_{\mathcal{O}\left(\epsilon a \left(\frac{a}{l}\right) \left(\frac{h}{a}\right)^{-1}\right)} \\
v_3 &= \underbrace{u_2 \dot{x}_3}_{\mathcal{O}\left(\epsilon l \left(\frac{a}{l}\right)^{-1}\right)} - \underbrace{u_3 \dot{x}_2}_{\mathcal{O}\left(\epsilon l \left(\frac{a}{l}\right)^{-1}\right)} - \underbrace{\theta r_\tau}_{\mathcal{O}\left(\epsilon l \left(\frac{h}{a}\right)^{-1}\right)} + \underbrace{\hat{w}_3}_{\mathcal{O}\left(\epsilon a \left(\frac{h}{a}\right)^{-1}\right)} + \underbrace{w_3}_{\mathcal{O}(\epsilon a)} + \underbrace{\tilde{w}_3}_{\mathcal{O}\left(\epsilon a \left(\frac{a}{l}\right) \left(\frac{h}{a}\right)^{-1}\right)} \tag{2.73}
\end{aligned}$$

where successive perturbation terms must be of a higher-order than their previous counterparts [19]. Substituting the perturbed displacement field, Eqs. 2.73 into the general strain field, Eqs. 2.9 and using the relations given in Eqs. 2.3 and 2.6, as done similarly for the first perturbation in Appendix A.2, yields

$$\begin{aligned}
\gamma_{11} &= \underbrace{u_1'}_{\mathcal{O}(\epsilon)} - \underbrace{x_\alpha u_\alpha''}_{\mathcal{O}(\epsilon)} - \underbrace{\eta\theta''}_{\mathcal{O}(\epsilon(\frac{a}{l})(\frac{h}{a})^{-1})} + \underbrace{w_{1,1}}_{\mathcal{O}(\epsilon(\frac{a}{l}))} + \underbrace{\tilde{w}_{1,1}}_{\mathcal{O}(\epsilon(\frac{a}{l})^2(\frac{h}{a})^{-1})} \\
2\gamma_{12} &= \underbrace{\hat{w}_{2,1}}_{\mathcal{O}(\epsilon(\frac{a}{l})(\frac{h}{a})^{-1})} + \underbrace{w_{1,2}}_{\mathcal{O}(\epsilon)} + \underbrace{w_{2,1}}_{\mathcal{O}(\epsilon(\frac{a}{l}))} + \underbrace{\hat{w}_{1,2}}_{\mathcal{O}(\epsilon(\frac{a}{l})(\frac{h}{a})^{-1})} + \underbrace{\tilde{w}_{2,1}}_{\mathcal{O}(\epsilon(\frac{a}{l})^2(\frac{h}{a})^{-1})} \\
\gamma_{22} &= \underbrace{w_{2,2}}_{\mathcal{O}(\epsilon)} + \underbrace{\frac{w_3}{R}}_{\mathcal{O}(\epsilon)} + \underbrace{\tilde{w}_{2,2}}_{\mathcal{O}(\epsilon(\frac{a}{l})(\frac{h}{a})^{-1})} + \underbrace{\frac{\tilde{w}_3}{R}}_{\mathcal{O}(\epsilon(\frac{a}{l})(\frac{h}{a})^{-1})} \\
h\rho_{11} &= h \left( \underbrace{\hat{x}_3 u_2''}_{\mathcal{O}(\epsilon(\frac{h}{a}))} - \underbrace{\hat{x}_2 u_3''}_{\mathcal{O}(\epsilon(\frac{h}{a}))} - \underbrace{r_\tau \theta''}_{\mathcal{O}(\epsilon(\frac{a}{l}))} + \underbrace{\hat{w}_{3,11}}_{\mathcal{O}(\epsilon(\frac{a}{l})^2)} + \underbrace{w_{3,11}}_{\mathcal{O}(\epsilon(\frac{a}{l})^2(\frac{h}{a}))} + \underbrace{\tilde{w}_{3,11}}_{\mathcal{O}(\epsilon(\frac{a}{l})^3)} \right) \\
h\rho_{12} &= h \left[ \underbrace{\frac{w_{1,2}}{4R}}_{\mathcal{O}(\epsilon(\frac{h}{a}))} - \underbrace{\theta'}_{\mathcal{O}(\epsilon)} + \underbrace{\hat{w}_{3,12}}_{\mathcal{O}(\epsilon(\frac{a}{l}))} + \underbrace{w_{3,12}}_{\mathcal{O}(\epsilon(\frac{a}{l})(\frac{h}{a}))} - \frac{3}{4R} \left( \underbrace{\hat{w}_{2,1}}_{\mathcal{O}(\epsilon(\frac{a}{l}))} + \underbrace{w_{2,1}}_{\mathcal{O}(\epsilon(\frac{a}{l})(\frac{h}{a}))} \right) \right] \\
&\quad + h \left[ \underbrace{\tilde{w}_{3,12}}_{\mathcal{O}(\epsilon(\frac{a}{l})^2)} + \frac{1}{4R} \left( \underbrace{\tilde{w}_{1,2}}_{\mathcal{O}(\epsilon(\frac{a}{l}))} - \underbrace{3\tilde{w}_{2,1}}_{\mathcal{O}(\epsilon(\frac{a}{l})^2)} \right) \right] \\
h\rho_{22} &= h \left[ \underbrace{\hat{w}_{3,2}}_{\mathcal{O}(\epsilon)} + \underbrace{w_{3,2}}_{\mathcal{O}(\epsilon(\frac{h}{a}))} + \underbrace{\tilde{w}_{3,2}}_{\mathcal{O}(\epsilon(\frac{a}{l}))} - \frac{1}{R} \left( \underbrace{\hat{w}_2}_{\mathcal{O}(\epsilon)} + \underbrace{w_2}_{\mathcal{O}(\epsilon(\frac{h}{a}))} + \underbrace{\tilde{w}_2}_{\mathcal{O}(\epsilon(\frac{a}{l}))} \right) \right]_{,2} \quad (2.74)
\end{aligned}$$

By inspection of Eqs. 2.74, the leading order perturbation terms of unknown order are  $\tilde{w}_{1,2}$ ,  $\tilde{w}_{2,2}$  and  $\frac{\tilde{w}_3}{R}$ , found in the expressions for  $2\gamma_{12}$  and  $\gamma_{22}$ . As the previous perturbation

has minimized the terms of  $\mathcal{O}(\epsilon^2)$  in the beam energy functional, the current perturbation must minimize terms of  $\mathcal{O}\left(\epsilon^2 \left(\frac{a}{l}\right) \left(\frac{h}{a}\right)^{-1}\right)$  and  $\mathcal{O}\left(\epsilon^2 \left(\frac{a}{l}\right)^2 \left(\frac{h}{a}\right)^{-2}\right)$ . Consequently, the leading order terms must have the same order as the largest known order terms that are not of  $\mathcal{O}(\epsilon)$  in the strain field, Eqs. 2.74, such that

$$\mathcal{O}(\tilde{w}_{1,2}) = \mathcal{O}(\tilde{w}_{2,2}) = \mathcal{O}\left(\frac{\tilde{w}_3}{R}\right) = \mathcal{O}(\eta\theta'') = \mathcal{O}(\hat{w}_{2,1}) = \mathcal{O}\left(\epsilon \left(\frac{a}{l}\right) \left(\frac{h}{a}\right)^{-1}\right) \quad (2.75)$$

As done before, the orders of the remaining perturbation terms are found using the relations given in Eqs. 2.32, 2.34 and 2.35. No new terms of  $\mathcal{O}(\epsilon)$  have been produced in the strain field given in Eqs. 2.74 by the third perturbation of the displacement field, as given in Eqs. 2.73. Consequently, the previous strain field, Eqs. 2.59 has converged to  $\mathcal{O}(\epsilon)$  accuracy. If the displacement field was perturbed a fourth time, it would be seen that no new terms of  $\mathcal{O}\left(\epsilon \left(\frac{a}{l}\right) \left(\frac{h}{a}\right)^{-1}\right)$  would be produced; consequently, the strain field given in Eqs. 2.74 has asymptotically converged to  $\mathcal{O}\left(\epsilon \left(\frac{a}{l}\right) \left(\frac{h}{a}\right)^{-1}\right)$  accuracy. A beam energy functional of  $\mathcal{O}\left(\epsilon^2 \left(\frac{a}{l}\right) \left(\frac{h}{a}\right)^{-1}\right)$  and  $\mathcal{O}\left(\epsilon^2 \left(\frac{a}{l}\right)^2 \left(\frac{h}{a}\right)^{-2}\right)$  accuracy can now be found using the present strain field. Retaining terms of  $\mathcal{O}\left(\epsilon \left(\frac{a}{l}\right) \left(\frac{h}{a}\right)^{-1}\right)$  in the strain field, Eqs. 2.74, yields

$$\begin{aligned} \tilde{\gamma}_{11} &= -\eta\theta'' \\ 2\tilde{\gamma}_{12} &= \hat{w}_{2,1} + \tilde{w}_{1,2} \\ \tilde{\gamma}_{22} &= \tilde{w}_{2,2} + \frac{\tilde{w}_3}{R} \\ h\tilde{\rho}_{11} &= 0 \\ h\tilde{\rho}_{12} &= 0 \\ h\tilde{\rho}_{22} &= 0 \end{aligned} \quad (2.76)$$

where  $\tilde{\gamma}_{11}$ ,  $\tilde{\gamma}_{12}$ ,  $\tilde{\gamma}_{22}$ ,  $\tilde{\rho}_{11}$ ,  $\tilde{\rho}_{12}$  and  $\tilde{\rho}_{22}$  are the strains containing the  $\mathcal{O}\left(\epsilon\left(\frac{a}{l}\right)\left(\frac{h}{a}\right)^{-1}\right)$  accurate terms. The corresponding strain term vectors, used in Eq. 2.30, become  $\tilde{\boldsymbol{\psi}}^T = \begin{bmatrix} \tilde{\gamma}_{11} & h\tilde{\rho}_{11} & h\tilde{\rho}_{12} \end{bmatrix}$  and  $\tilde{\boldsymbol{\phi}}^T = \begin{bmatrix} 2\tilde{\gamma}_{12} & \tilde{\gamma}_{22} & h\tilde{\rho}_{22} \end{bmatrix}$ , where  $\tilde{\boldsymbol{\psi}}$  contains all the known  $\mathcal{O}\left(\epsilon\left(\frac{a}{l}\right)\left(\frac{h}{a}\right)^{-1}\right)$  strain terms and  $\tilde{\boldsymbol{\phi}}$  contains all the unknown  $\mathcal{O}\left(\epsilon\left(\frac{a}{l}\right)\left(\frac{h}{a}\right)^{-1}\right)$  strain terms.

The vector of known strains  $\tilde{\boldsymbol{\psi}}$  can be expressed in terms of  $\bar{\boldsymbol{\epsilon}}$ , Eq. 2.63, as

$$\tilde{\boldsymbol{\psi}} = \tilde{\mathbf{T}}\bar{\boldsymbol{\epsilon}}' \quad (2.77)$$

where

$$\tilde{\boldsymbol{\psi}} = \begin{bmatrix} \tilde{\gamma}_{11} \\ h\tilde{\rho}_{11} \\ h\tilde{\rho}_{12} \end{bmatrix} = \begin{bmatrix} -\eta\theta'' \\ 0 \\ 0 \end{bmatrix} = \begin{bmatrix} 0 & -\eta & 0 & 0 \\ 0 & 0 & 0 & 0 \\ 0 & 0 & 0 & 0 \end{bmatrix} \begin{bmatrix} u_1'' \\ \theta'' \\ -u_3''' \\ u_2''' \end{bmatrix} \quad (2.78)$$

and consequently,

$$\tilde{\mathbf{T}} = \begin{bmatrix} 0 & -\eta & 0 & 0 \\ 0 & 0 & 0 & 0 \\ 0 & 0 & 0 & 0 \end{bmatrix} \quad (2.79)$$

The known and unknown strain vectors,  $\boldsymbol{\psi}$  and  $\boldsymbol{\phi}$ , respectively, can be expressed as an asymptotic expansion in terms of  $\bar{\boldsymbol{\psi}}$  and  $\tilde{\boldsymbol{\psi}}$ , and  $\bar{\boldsymbol{\phi}}$  and  $\tilde{\boldsymbol{\phi}}$ , respectively, as

$$\begin{aligned} \boldsymbol{\psi} &= \underbrace{\bar{\boldsymbol{\psi}}}_{\mathcal{O}(\epsilon)} + \underbrace{\tilde{\boldsymbol{\psi}}}_{\mathcal{O}\left(\epsilon\left(\frac{a}{l}\right)\left(\frac{h}{a}\right)^{-1}\right)} + \mathcal{O}\left(\epsilon\left(\frac{a}{l}\right)^2\left(\frac{h}{a}\right)^{-1} \text{ or } \epsilon\left(\frac{a}{l}\right)\right) \\ \boldsymbol{\phi} &= \underbrace{\bar{\boldsymbol{\phi}}}_{\mathcal{O}(\epsilon)} + \underbrace{\tilde{\boldsymbol{\phi}}}_{\mathcal{O}\left(\epsilon\left(\frac{a}{l}\right)\left(\frac{h}{a}\right)^{-1}\right)} + \mathcal{O}\left(\epsilon\left(\frac{a}{l}\right)^2\left(\frac{h}{a}\right)^{-1} \text{ or } \epsilon\left(\frac{a}{l}\right)\right) \end{aligned} \quad (2.80)$$

Dropping the higher-order terms from Eqs. 2.80, and substituting the expressions for  $\psi$  and  $\phi$  into Eq. 2.30, yields

$$\begin{aligned} 2\mathcal{U}_{refined}^{(m)} = & 2\mathcal{U}^{(m)} + \int_{\Sigma_s} \left( \bar{\psi}^T \mathbf{Q} \tilde{\psi} + \tilde{\psi}^T \mathbf{Q} \bar{\psi} + \tilde{\psi}^T \mathbf{Q} \tilde{\psi} + 2\tilde{\phi}^T \mathbf{S} \tilde{\psi} + \tilde{\phi}^T \mathbf{P} \tilde{\phi} \right. \\ & \left. - 2\tilde{\psi}^T \mathbf{H} - 2\tilde{\phi}^T \mathbf{G} + 2\tilde{\phi}^T \mathbf{S} \bar{\psi} + 2\bar{\phi}^T \mathbf{S} \tilde{\psi} + \bar{\phi}^T \mathbf{P} \tilde{\phi} + \tilde{\phi}^T \mathbf{P} \bar{\phi} \right) ds \end{aligned} \quad (2.81)$$

where the lower-order terms of  $\mathcal{O}(\epsilon^2)$  have been grouped into the  $2\mathcal{U}^{(m)}$  term that is given in Eq. 2.62.

As the unknown strain vector  $\bar{\phi}$  was determined in the previous minimization, resulting in Eq. 2.69, another expression for  $\bar{\phi}$  cannot be calculated during this minimization. Consequently,  $\bar{\phi}\tilde{\psi}$  and  $\bar{\phi}\bar{\phi}$  cross terms must vanish in the refined energy functional, Eq. 2.81 [8, 18, 54]. Similarly,  $\tilde{\phi}\bar{\psi}$  cross terms cannot exist since  $\bar{\psi}$  only contributes to the minimization of the previous refined energy functional with respect to  $\bar{\phi}$  [54]. In other words, these cross terms are linearly independent, and thus are orthogonal. Discarding the  $\bar{\phi}\tilde{\psi}$ ,  $\bar{\phi}\bar{\phi}$  and  $\tilde{\phi}\bar{\psi}$  cross terms from Eq. 2.81, and substituting Eqs. 2.64 and 2.77 into Eq. 2.81, yields

$$\begin{aligned} 2\mathcal{U}_{refined}^{(m)} = & \underbrace{2\mathcal{U}^{(m)}}_{\mathcal{O}(\epsilon)} + \int_{\Sigma_s} \left( \underbrace{2\bar{\epsilon}^T \tilde{\mathbf{T}}^T \mathbf{Q} \tilde{\mathbf{T}} \bar{\epsilon}}_{\mathcal{O}(\epsilon^2 (\frac{a}{l}) (\frac{h}{a})^{-1})} + \underbrace{\bar{\epsilon}^T \tilde{\mathbf{T}}^T \mathbf{Q} \tilde{\mathbf{T}} \bar{\epsilon} + 2\tilde{\phi}^T \mathbf{S} \tilde{\mathbf{T}} \bar{\epsilon}}_{\mathcal{O}(\epsilon^2 (\frac{a}{l})^2 (\frac{h}{a})^{-2})} \right. \\ & \left. + \underbrace{\tilde{\phi}^T \mathbf{P} \tilde{\phi}}_{\mathcal{O}(\epsilon^2 (\frac{a}{l})^2 (\frac{h}{a})^{-2})} - \underbrace{2\bar{\epsilon}^T \tilde{\mathbf{T}}^T \mathbf{H} - 2\tilde{\phi}^T \mathbf{G}}_{\mathcal{O}(\epsilon^2 (\frac{a}{l}) (\frac{h}{a})^{-1}) \text{ or } \mathcal{O}(\epsilon^2 (\frac{a}{l})^2 (\frac{h}{a})^{-2})} \right) ds \end{aligned} \quad (2.82)$$

where  $\bar{\epsilon}^T \mathbf{T}^T \mathbf{Q} \tilde{\mathbf{T}} \bar{\epsilon}' = \left( \bar{\epsilon}'^T \tilde{\mathbf{T}}^T \mathbf{Q} \mathbf{T} \bar{\epsilon} \right)^T = \bar{\epsilon}'^T \tilde{\mathbf{T}}^T \mathbf{Q} \mathbf{T} \bar{\epsilon}$  since the terms of Eq. 2.82 are scalar quantities. For the terms in Eq. 2.82 containing the electromechanical matrices  $\mathbf{H}$  and  $\mathbf{G}$ , their orders can be either  $\mathcal{O} \left( \epsilon^2 \left( \frac{a}{l} \right) \left( \frac{h}{a} \right)^{-1} \right)$  or  $\mathcal{O} \left( \epsilon^2 \left( \frac{a}{l} \right)^2 \left( \frac{h}{a} \right)^{-2} \right)$  since the electromechanical matrices  $\mathbf{H}$  and  $\mathbf{G}$ , which contain the prescribed strain field  $\epsilon_{\alpha\beta}^{(a)}$ , can be up to  $\mathcal{O}(\epsilon)$ , but still produce terms of higher-order.

Next, the energy functional, Eq. 2.82, is minimized with respect to the unknown strains  $\tilde{\phi}$ , as

$$\begin{aligned} \delta \left( 2\mathcal{U}_{refined}^{(m)} \right) &= 0 \\ \left( 2\mathbf{S} \tilde{\mathbf{T}} \bar{\epsilon}' + 2\mathbf{P} \tilde{\phi} - 2\mathbf{G} \right) \delta \tilde{\phi} &= 0 \\ \tilde{\phi} &= -\mathbf{P}^{-1} \mathbf{S} \tilde{\mathbf{T}} \bar{\epsilon}' + \mathbf{P}^{-1} \mathbf{G} \end{aligned} \quad (2.83)$$

Substituting Eq. 2.83 into Eq. 2.82 and simplifying, yields

$$\begin{aligned} 2\mathcal{U}_{refined}^{(m)} &= 2\mathcal{U}^{(m)} + \int_{\Sigma_s} \left[ \tilde{\psi}^T \mathbf{Q} \tilde{\psi} - \tilde{\psi}^T \mathbf{S}^T \mathbf{P}^{-1} \mathbf{S} \tilde{\psi} \right. \\ &\quad \left. + 2\tilde{\psi}^T \mathbf{Q} \mathbf{T} \bar{\epsilon} - 2\tilde{\psi}^T \mathbf{H} + 2\tilde{\psi}^T \mathbf{S}^{-1} \mathbf{P}^{-1} \mathbf{G} \right] ds \end{aligned} \quad (2.84)$$

where the relation  $\mathbf{P} = \mathbf{P}^T$ , inferred from Eqs. A.8, has been used, and the transpose of any term must be equal to itself since they are scalar quantities. The refined strain energy has the form,

$$2\mathcal{U}_{refined}^{(m)} = 2\mathcal{U}^{(m)} + 2\mathcal{U}_{Vlasov}^{structural} + 2\mathcal{U}_{Vlasov}^{(a)} \quad (2.85)$$

where

$$\begin{aligned}
2\mathcal{U}_{Vlasov}^{structural} &= \int_{\Sigma^s} \left[ \tilde{\psi}^T \mathbf{Q} \tilde{\psi} - \tilde{\psi}^T \mathbf{S}^T \mathbf{P}^{-1} \mathbf{S} \tilde{\psi} + 2\tilde{\psi}^T \mathbf{Q} \mathbf{T} \bar{\epsilon} \right] ds \\
2\mathcal{U}_{Vlasov}^{(a)} &= \int_{\Sigma^s} \left[ -2\tilde{\psi}^T \mathbf{H} + 2\tilde{\psi}^T \mathbf{S}^{-1} \mathbf{P}^{-1} \mathbf{G} \right] ds
\end{aligned} \tag{2.86}$$

and  $2\mathcal{U}^{(m)}$  has been given in Eq. 2.71.

The current, third perturbation of the displacement field gives the second order approximation to both the strain field and energy functional. Using the refined energy functional, Eq. 2.85, analytical expressions will be found for the cross sectional stiffness constants and induced force/moments/bimoment actuation constants at the beam reference line in the next section.

### 2.3.5 Stiffness and Actuation Constants

Only the energy terms that contain mechanical strains will contribute to the expressions for the cross sectional stiffness constants and induced force/moments/bimoment actuation constants. Consequently, the quadratic electric field terms of the refined beam energy functional in Eq. 2.85 will not contribute to the actuation constants. The portion of the refined energy that contributes to the cross sectional stiffness and actuation constants has the form

$$\begin{aligned}
2\mathcal{U}_{refined} &= \bar{\epsilon}^T \mathbf{C}_{classical} \bar{\epsilon} + 2\bar{\epsilon}^T \mathbf{C}_{Vlasov/classical} \bar{\epsilon}' + \bar{\epsilon}'^T \mathbf{C}_{Vlasov} \bar{\epsilon}' \\
&\quad + 2\mathcal{U}(\bar{\epsilon})_{classical}^{(a)} + 2\mathcal{U}(\bar{\epsilon}')_{refined}^{(a)}
\end{aligned} \tag{2.87}$$

The cross sectional stiffness and actuation constants can be found by differentiation of

each individual term in Eq. 2.87 by the vectors of strains at the beam reference line,  $\bar{\epsilon}$  and  $\bar{\epsilon}'$ , as follows. Grouping the terms of Eqs. 2.72 and 2.86 with the terms given in Eq. 2.87, and differentiating the terms by  $\bar{\epsilon}$  and  $\bar{\epsilon}'$ , as appropriate:

$$\begin{aligned}
\mathbf{C}_{\text{classical (4x4)}} &= \frac{1}{2} \frac{\partial}{\partial \bar{\epsilon}} \frac{\partial}{\partial \bar{\epsilon}} [\bar{\epsilon}'^T \mathbf{C}_{\text{classical}} \bar{\epsilon}] \\
&= \frac{1}{2} \frac{\partial}{\partial \bar{\epsilon}} \frac{\partial}{\partial \bar{\epsilon}} \int_{\Sigma_s} [\bar{\epsilon}'^T \mathbf{T}^T (\mathbf{Q} - \mathbf{S}^T \mathbf{P}^{-1} \mathbf{S}) \mathbf{T} \bar{\epsilon}] \, ds \\
&= \int_{\Sigma_s} [\mathbf{T}^T (\mathbf{Q} - \mathbf{S}^T \mathbf{P}^{-1} \mathbf{S}) \mathbf{T}] \, ds \tag{2.88}
\end{aligned}$$

$$\begin{aligned}
\mathbf{C}_{\text{Vlasov/classical (4x1)}} &= \frac{1}{2} \frac{\partial}{\partial \bar{\epsilon}} \frac{\partial}{\partial \bar{\epsilon}'} [2\bar{\epsilon}'^T \mathbf{C}_{\text{Vlasov/classical}} \bar{\epsilon}'] \\
&= \frac{1}{2} \frac{\partial}{\partial \bar{\epsilon}} \frac{\partial}{\partial \bar{\epsilon}'} \int_{\Sigma_s} [2\tilde{\psi}^T \mathbf{Q} \mathbf{T} \bar{\epsilon}] \, ds \\
&= \int_{\Sigma_s} \left( \begin{bmatrix} -\eta & 0 & 0 \end{bmatrix} \mathbf{Q} \mathbf{T} \right) \, ds \tag{2.89}
\end{aligned}$$

$$\begin{aligned}
\mathbf{C}_{\text{Vlasov}} &= \frac{1}{2} \frac{\partial}{\partial \bar{\epsilon}'} \frac{\partial}{\partial \bar{\epsilon}'} [\bar{\epsilon}'^T \mathbf{C}_{\text{Vlasov}} \bar{\epsilon}'] \\
&= \frac{1}{2} \frac{\partial}{\partial \bar{\epsilon}'} \frac{\partial}{\partial \bar{\epsilon}'} \int_{\Sigma_s} [\tilde{\psi}^T \mathbf{Q} \tilde{\psi} - \tilde{\psi}^T \mathbf{S}^T \mathbf{P}^{-1} \mathbf{S} \tilde{\psi}] \, ds \\
&= \int_{\Sigma_s} \left( \begin{bmatrix} -\eta & 0 & 0 \end{bmatrix} \mathbf{Q} \begin{bmatrix} -\eta \\ 0 \\ 0 \end{bmatrix} \right. \\
&\quad \left. - \begin{bmatrix} -\eta & 0 & 0 \end{bmatrix} \mathbf{S}^T \mathbf{P}^{-1} \mathbf{S} \begin{bmatrix} -\eta \\ 0 \\ 0 \end{bmatrix} \right) \, ds \tag{2.90}
\end{aligned}$$

$$\begin{aligned}
\begin{bmatrix} F_1^{(a)} \\ M_1^{(a)} \\ M_2^{(a)} \\ M_3^{(a)} \end{bmatrix} &= \frac{1}{2} \frac{\partial}{\partial \bar{\epsilon}} 2\mathcal{U}(\bar{\epsilon})_{classical}^{(a)} \\
&= \frac{1}{2} \frac{\partial}{\partial \bar{\epsilon}} \int_{\Sigma_s} \left[ 2(\mathbf{G}^T \mathbf{P}^{-1} \mathbf{S} \mathbf{T} \bar{\epsilon})^T - 2(\mathbf{H}^T \mathbf{T} \bar{\epsilon})^T \right] ds \\
&= \int_{\Sigma_s} \left[ (\mathbf{G}^T \mathbf{P}^{-1} \mathbf{S} \mathbf{T})^T - (\mathbf{H}^T \mathbf{T})^T \right] ds \tag{2.91}
\end{aligned}$$

$$\begin{aligned}
M_\omega^{(a)} &= \frac{1}{2} \frac{\partial}{\partial \bar{\epsilon}'} 2\mathcal{U}(\bar{\epsilon}')_{refined}^{(a)} \\
&= \frac{1}{2} \frac{\partial}{\partial \bar{\epsilon}'} \int_{\Sigma_s} \left[ -2\tilde{\psi}^T \mathbf{H} + 2\tilde{\psi}^T \mathbf{S}^{-1} \mathbf{P}^{-1} \mathbf{G} \right] ds \\
&= \int_{\Sigma_s} \left( - \begin{bmatrix} -\eta & 0 & 0 \end{bmatrix} \mathbf{H} + \begin{bmatrix} -\eta & 0 & 0 \end{bmatrix} \mathbf{S}^{-1} \mathbf{P}^{-1} \mathbf{G} \right) ds \tag{2.92}
\end{aligned}$$

where  $\mathbf{C}_{classical}$  is the stiffness matrix corresponding to the classical degrees of freedom  $\bar{\epsilon}$ ;  $\mathbf{C}_{Vlasov/classical}$  is a stiffness vector that contains the coupling terms between the classical degrees of freedom  $\bar{\epsilon}$  and the Vlasov degree of freedom  $\theta''$ , which is associated with  $\bar{\epsilon}'$ ;  $\mathbf{C}_{Vlasov}$  is the Vlasov stiffness term corresponding to the Vlasov degree of freedom  $\theta''$ ;  $F_1^{(a)}$ ,  $M_1^{(a)}$ ,  $M_2^{(a)}$ ,  $M_3^{(a)}$  and  $M_\omega^{(a)}$  are the induced extensional force along the  $x_1$  axis, torsion about the  $x_1$  axis, bending moments about the  $x_2$  and  $x_3$  axes, and bimoment, respectively, on the cross section due to actuation of the piezoelectric materials. The above analytical expressions, Eqs. 2.88, 2.89, 2.90, 2.91 and 2.92, can be solved over an OCSTWB cross section by first numerically integrating through each laminate thickness to compute the material matrices  $\mathbf{Q}$ ,  $\mathbf{S}$  and  $\mathbf{P}$ , and electromechanical matrices  $\mathbf{H}$  and  $\mathbf{G}$  of each laminate. Finally, the analytical expressions can be numerically integrated along the entire cross

sectional contour, where the contour can be divided into segments—called “branches”—to simplify integration by identifying segments of the contour that have similar geometry and laminate configuration, such as a straight horizontal contour segment with a constant laminate lay-up. The cross sectional stiffness constants, given by Eqs. 2.88, 2.89 and 2.90, are the components of the cross sectional stiffness matrix given in Eq. 1.2, such that

$$\begin{bmatrix} C_{11} & C_{12} & C_{13} & C_{14} & C_{15} \\ C_{12} & C_{22} & C_{23} & C_{24} & C_{25} \\ C_{13} & C_{23} & C_{33} & C_{34} & C_{35} \\ C_{14} & C_{24} & C_{34} & C_{44} & C_{45} \\ C_{15} & C_{25} & C_{35} & C_{45} & C_{55} \end{bmatrix} = \begin{bmatrix} \begin{bmatrix} C_{classical} \\ (C_{Vlasov/classical})^T \end{bmatrix} \\ \begin{bmatrix} C_{Vlasov/classical} \\ C_{Vlasov} \end{bmatrix} \end{bmatrix} \quad (2.93)$$

The beam constitutive model for OCSTWB, given in Eq. 1.2, can be extended to active OCSTWB using the induced force/moments/bimoment actuation constants at the beam reference line, Eqs. 2.91 and 2.92, such that

$$\begin{bmatrix} F_1 \\ M_1 \\ M_2 \\ M_3 \\ M_\omega \end{bmatrix} = \begin{bmatrix} C_{11} & C_{12} & C_{13} & C_{14} & C_{15} \\ C_{12} & C_{22} & C_{23} & C_{24} & C_{25} \\ C_{13} & C_{23} & C_{33} & C_{34} & C_{35} \\ C_{14} & C_{24} & C_{34} & C_{44} & C_{45} \\ C_{15} & C_{25} & C_{35} & C_{45} & C_{55} \end{bmatrix} \begin{bmatrix} \gamma_{11} \\ \kappa_1 \\ \kappa_2 \\ \kappa_3 \\ \kappa'_1 \end{bmatrix} + \begin{bmatrix} F_1^{(a)} \\ M_1^{(a)} \\ M_2^{(a)} \\ M_3^{(a)} \\ M_\omega^{(a)} \end{bmatrix} \quad (2.94)$$

where the vector on the left-hand side gives the total force/moments/bimoment at the beam reference line, the first term on the right-hand side gives the force/moments/bimoment due to mechanical strain, and the second term on the right-hand side gives the force-/moments/bimoment due to piezoelectric actuation. In the next chapter, the above active

OCSTWB cross sectional analysis approach is compared against UM/VABS and GT/V-ABS using various example cross sections.

# Chapter 3

## Verification of the Active OCSTWB Analysis

In this chapter, the active OCSTWB analysis approach that is outlined in Chapter 2 is compared against UM/VABS and GT/VABS using various cross sections. The example cross sections will be presented, the preparation of input files for UM/VABS and the active OCSTWB code will be described, and the output results will be given and discussed.

### 3.1 Cross Section Examples

Six OCSTWB cross section examples, representing typical beam cross sections, have been used to validate the active OCSTWB code, as summarized in Table 3.1. The corresponding geometry of each cross section is shown in Figure 3.1. For each cross section, the reference line, and thus the origin of the global Cartesian coordinate system  $x_i$ , is positioned at the area centroid. The first example, a passive isotropic channel beam, was taken from the cross section examples included with the GT/VABS code, where both the input and output data for the example was included. Cross section Examples 2 through 6 represent

normal OCSTWBs. Beam Example 4 is referred to as an extensional I-beam since, as will be seen in Chapter 4, the beam undergoes displacement in the axial direction only. Beam Example 5 is referred to as a bimoment I-beam since the active plies induce only a bimoment in the beam.

**Table 3.1:** Summary of the cross section examples investigated.

	Geometry	Active or Passive
1. Isotropic Channel	Figure 3.1(a)	Passive
2. Strip	Figure 3.1(b)	Active
3. Cruciform	Figure 3.1(c)	Active
4. Extensional I-Beam	Figure 3.1(d)	Active
5. Bimoment I-Beam	Figure 3.1(d)	Active
6. Channel	Figure 3.1(e)	Active

The material properties used for the isotropic channel cross section are:  $E = 2.6E + 9$ ,  $G = 1.0E + 9$  and  $\nu = 0.3$ . Two materials have been used for the anisotropic cross section examples: passive carbon fibre plies, AS4/3506-1 and early generation generic active fibre plies with PZT fibres [24]. The material properties are listed in Table 3.2. The orthotropic elastic properties are given by the Young's moduli  $E_{11}$  and  $E_{22}$ , the shear moduli  $G_{12}$  and  $G_{23}$ , and the Poisson's ratios  $\nu_{12}$  and  $\nu_{23}$ , with respect to the local ply coordinate system  $x_{i-local}$ . The electromechanical properties are given by the electromechanical coupling terms  $d_{111}$ ,  $d_{112}$  and  $d_{122}$ . The ply thickness is given by  $t_{ply}$ , and the spacing between the interdigitated electrodes is given by  $t_{electrodes}$ .

The seven ply laminate lay-up of each branch, listed in Table 3.3, is given from bottom

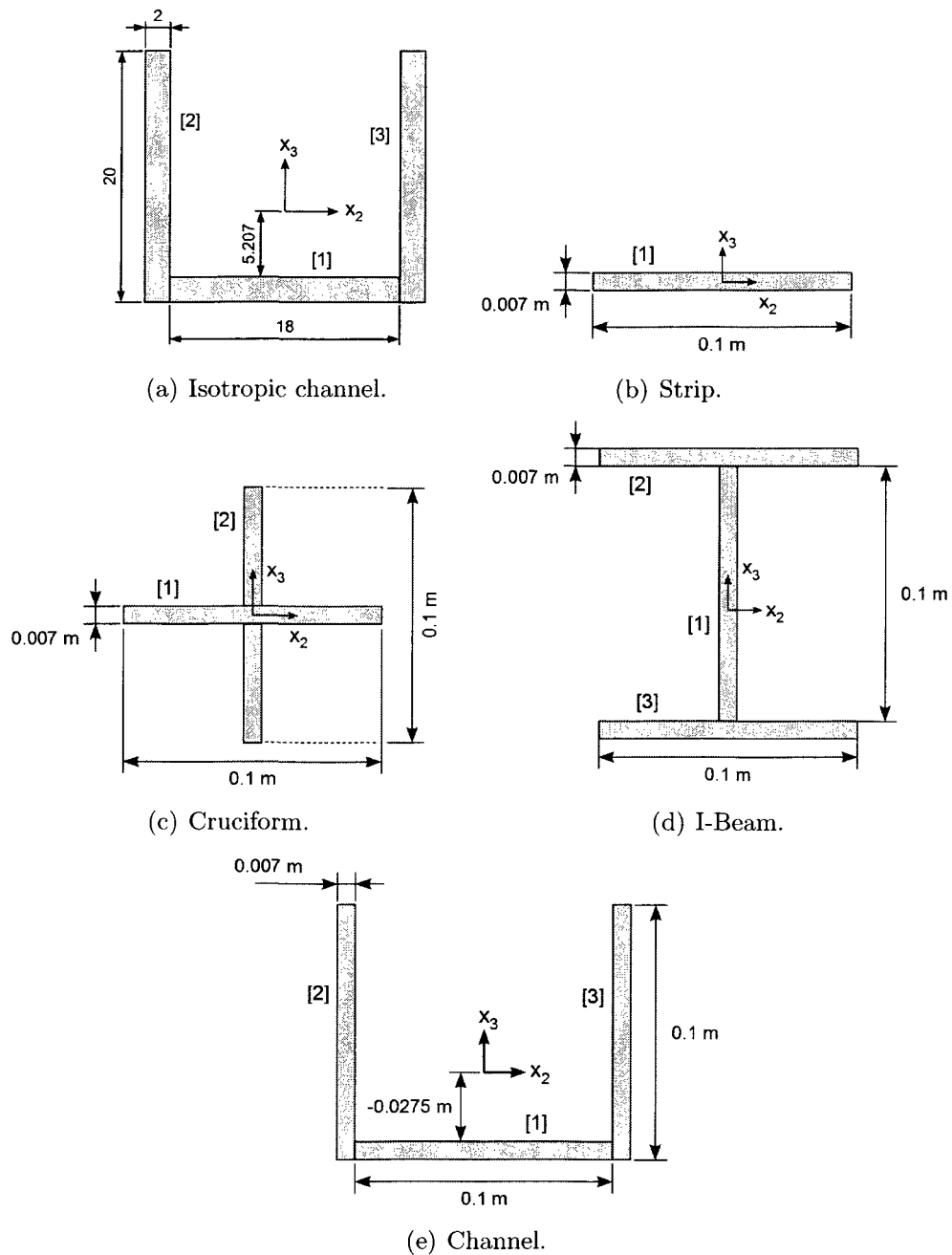


**Figure 3.1:** Geometry of the passive and active OCSTWB cross section examples.

to top for horizontal branches, and from left to right for vertical branches. The voltages applied to the active plies of each branch are given below the ply stacking sequence; in the case of Example 5, the bimoment I-beam, the voltage sign is reversed between the left

**Table 3.2:** Passive and active ply material properties.

	AS4/3506-1	Generic AFC
$E_{11}$ [GPa]	141.96	42.2
$E_{22}$ [GPa]	9.79	17.5
$G_{12}$ [GPa]	6	5.5
$G_{23}$ [GPa]	4.8	4.4
$\nu_{12}$	0.3	0.35
$\nu_{23}$	0.4	0.42
$t_{ply}$ [m]	1.0E-3	1.0E-3
$d_{111}$ [m/V]		3.81E-10
$d_{112}$ [m/V]		0
$d_{122}$ [m/V]		-1.6E-10
$t_{electrodes}$ [m]		1.1E-3

and right halves of the flanges. This checkered voltage pattern was used to induce a pure bimoment for the I-beam cross section. These examples, listed in order of complexity, were chosen to demonstrate the capabilities of the active OCSTWB code and the limitations one has to consider in applying the code to active OCSTWB.

**Table 3.3:** Laminate lay-up and applied voltage of each branch.

	Branch		
	[1]	[2]	[3]
1. Isotropic Channel	Isotropic	Isotropic	Isotropic
2. Strip	[0S/(45A) <sub>2</sub> /0S/(-45A) <sub>2</sub> /0S] +2000 V		
3. Cruciform	[0S/(-45A) <sub>2</sub> /0S/(45A) <sub>2</sub> /0S] +2000 V	[(0S/90S) <sub>3</sub> /0S]	
I-Beam:	[(0S) <sub>7</sub> ]	[0S/(0A) <sub>2</sub> /0S/(0A) <sub>2</sub> /0S]	[0S/(0A) <sub>2</sub> /0S/(0A) <sub>2</sub> /0S]
4. Extensional		+2000 V	+2000 V
5. Bimoment		+2000 V / -2000 V	-2000 V / +2000 V
6. Channel	[(45S/0S) <sub>3</sub> /45S]	[(0S/0A) <sub>3</sub> /0S] +2000 V	[(0S/0A) <sub>3</sub> /0S] -2000 V

Example 1 was analysed by GT/VABS, UM/VABS and the active OCSTWB code; the

remaining five examples were analysed by UM/VABS and the active OCSTWB code only. At the time the analyses were done, only UM/VABS had the capability to analyse cross sections with active materials; for GT/VABS, the capability of analysing cross sections with active materials was being incorporated into its code. In the next section, the preparation of input files for both UM/VABS and the active OCSTWB code will be presented.

## 3.2 Preparation of Input Files

### 3.2.1 UM/VABS

As specified in the UM/VABS documentation, UM/VABS requires a single text input file that contains the nodal coordinates of the meshed cross section; the definition of elements by nodes, type and material properties; the elastic and electromechanical properties of the materials; the ply angles and applied voltages; displacement constraints; and various parameters that control the type of analysis to be performed and the behaviour of the code [55]. A 3-D CAD program with a graphical user interface, called GiD, was used to generate a 2-D mesh of the example cross sections, including individual element material type assignment [56]. Using the custom file output generation capabilities of GiD, output code was written to instruct GiD to generate a fully compatible UM/VABS input file.

To begin, the 2-D geometry of a cross section is entered into GiD as a set of planar surfaces, as shown in Figures 3.2(a) and 3.2(b) for the I-beam and channel cross sections, respectively. An isoperimetric quadrilateral plate element, called CQUAD4, was used as the element type for the UM/VABS input file. As a CQUAD4 element is defined by a single node at each of its four corners, the surface is meshed with a structured mesh of quadrilateral elements, such that every interior node is directly connected to four nodes. As the anisotropic cross section examples are composed of laminates with seven equally

thick plies, the meshed cross sections must be seven elements thick, or a number evenly divisible by seven. The number of elements can be controlled in GiD by selecting **Meshed > Structured > Lines > Assign\_Number\_of\_Cells** in the GiD menu, choosing the lines that span the thickness of the example cross sections, and entering the number of elements, such as 7 for the present examples. The meshed I-beam and channel cross sections, each meshed with over 600 elements, are shown in Figures 3.2(c) and 3.2(d), respectively. A larger number of elements could not be used as the limited evaluation version of the software, which was used, did not permit more than 1000 nodes to be used in a mesh.

A CQUAD4 element is defined by listing its four corner nodes in a consecutive, counter-clockwise (CCW) order around the element, where a vector from the first node to the second node defines the direction of the  $x_{2-local}$  laminate axis [55]. For each of the six surfaces shown in Figures 3.2(a) and 3.2(b), GiD can use a different nodal ordering scheme for the elements generated, i.e. either clockwise or counter-clockwise, or with the first node located at any of the four element corners, as shown in Figure 3.3(a) for the channel cross section. The nodal ordering scheme of the channel sections, shown in Figure 3.3(a), must be reordered to the scheme shown in Figure 3.3(b). The ordering scheme used for a particular surface can be determined by selecting **Utilities > List > Elements** in the GiD menu, choosing an element of the desired surface, noting the order of the four nodes that define it, selecting **View > Label > All**, and comparing the nodal order for the element with the locations of its labelled nodes. Each surface, and the elements it contains, can be assigned to a single designation, called a “layer.” As there are eight possible ordering schemes—two directions and four locations for the first node—eight layers are created, each corresponding to a different ordering scheme. Each surface is subsequently assigned to the layer corresponding to the ordering scheme used for its elements. Output code was written to reorder the nodes of each element to the convention required for the UM/VABS input file using the layer designations assigned to every element, as given in Appendix B.1.1.

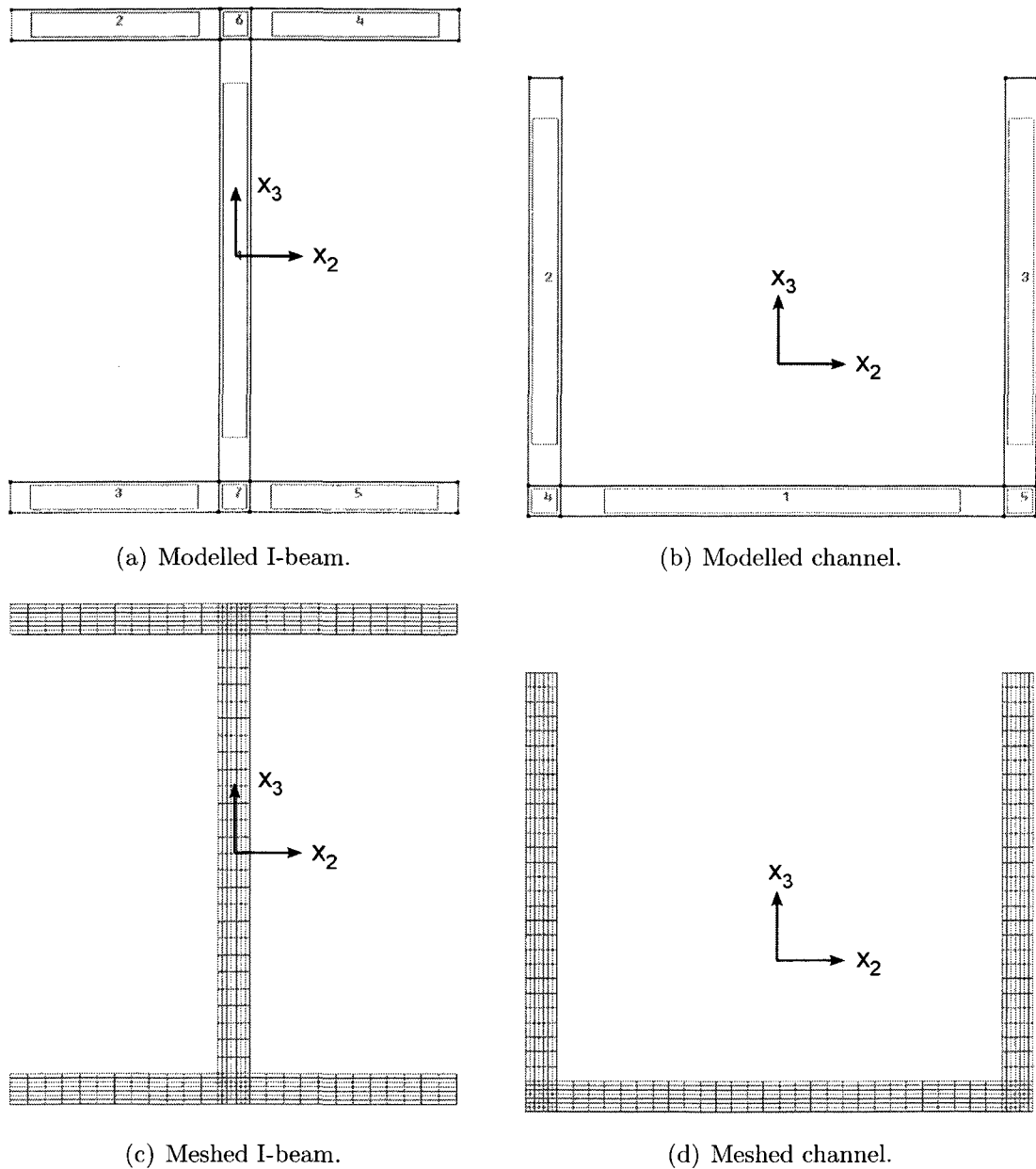


**Figure 3.2:** Modelled and meshed example cross sections in GiD.

In order to assign materials, ply angles and applied voltages, a set of files, that together are called a “problem type,” must be created and loaded into the main file, which contains the meshed cross section. These files also contain the output code used to generate the UM/VABS input file. Using the included `cmas2d.gid` problem type as a template, only the

.mat materials file and .bas output instructions code file were changed, and are included in Appendices B.1.1 and B.1.2, respectively. Defining a material type entry for every combination of materials, ply angles and applied voltages used, such as AS4/3506\_45deg and AFC\_0deg\_-2000V, the material type combinations are assigned to individual elements. This can be done by selecting **Data > Materials**, choosing the appropriate material type combination from the drop-down box, clicking **Assign > Elements**, and selecting the required elements. The results are shown in Figures 3.4(a) and 3.4(b) for the I-beam and channel cross sections, respectively.

A 3-D orthotropic material entry type, called MAT3D, was used to define the elastic properties of both the passive AS4/3506-1 carbon fibre composite, and the active fibre composite. Piezoelectric behaviour was modelled using thermal expansion through the active thermal entry, called MAT5. To apply piezoelectric material properties to a MAT5 active thermal entry, the equivalent thermal coefficients of expansion are set to  $\alpha_{11} = Vd_{111}$ ,  $\alpha_{22} = Vd_{122}$ ,  $\alpha_{12} = Vd_{112}$ , the remaining  $\alpha_{ij}$  thermal-mechanical coupling constants are set to zero, and the THICK field is set to  $t_{electrodes}$ . The applied voltage  $V$  is set by the TEMPD entry, which gives the change in temperature across the thickness, given by the THICK field. This is a direct parallel to the piezoelectric effect, where a change of voltage  $V$  occurs across the electrode spacing  $t_{electrodes}$ . As the TEMPD entry can only be set once, it is set to a value of unity and the electromechanical coupling constants  $d_{1ij}$  are scaled by the the applied voltage  $V$ . A unique material entry must be set for each combination of material and applied voltage used in the cross section.

An element property entry, called PSHELL, associates a material entry to a ply orientation angle  $\vartheta$ . A unique element property entry must be set for each combination of material entry and ply orientation angle.

Similar to how a 3-D FE model must be constrained from rigid body motion, the 2-D FE cross section must also be constrained. These rigid body constraints are applied using the **SPCADD** and **SPC1** single point constraint entries. UM/VABS requires that a cross section be constrained from rigid body translation in all three orthogonal directions, and from in-plane rigid body rotation. This can be done by placing constraints on two nodes in the cross section. First, an arbitrary node is chosen and constrained from rigid body translation in all three orthogonal directions. Second, an additional node is chosen and constrained against motion in either the  $x_2$  or  $x_3$  in-plane directions, such that rigid body in-plane rotation is constrained without constraining the cross sectional warping. The control parameters are set as shown in Appendix B.1.2, where the **VLASOV** parameter must be set to **YES** to request that a Vlasov analysis be performed on the cross section.

An input file can be generated by selecting **Files > Export > Calculation\_file...** in the GiD menu and giving it a **.vabs** extension. Once run in UM/VABS, such as by dragging the input file to the UM/VABS executable application file, the **.vout** output file will contain the  $5 \times 5$  cross sectional Vlasov stiffness matrix  $\mathbf{C}$  and the  $5 \times 1$  induced actuation vector, called a “Vlasov active force vector,” among other information. The UM/VABS coding factors out the negative signs of the  $F_1^{(a)}$ ,  $M_1^{(a)}$ ,  $M_3^{(a)}$  and  $M_\omega^{(a)}$  induced actuation terms. Consequently, these terms must be multiplied by  $-1$  in order to compare them against those predicted by the active OCSTWB code.

### 3.2.2 Active OCSTWB Code

The active OCSTWB theory that was presented in Chapter 2 was implemented using code written in MATLAB [15]. As specified in the active OCSTWB code documentation, two text input files are required. The first, **contour\_input.m**, contains the contour geometry, the paths of integration, and the laminate assignments; the second, **LaminatesInput.dat**,

contains the material properties, the ply thicknesses, the laminate ply lay-ups of each branch segment, and the applied electric fields [57]. In order to describe the contour of a cross section, a contour origin and a path of integration are required. A contour origin must satisfy the requirement that [15]

$$\int_{\Sigma s} \eta \, ds = 0 \quad (3.1)$$

where  $\eta$  has been defined in Eq. 2.53. The paths of integration proceed from the contour origin to the end points, or “edges,” of the cross section. At each corner, a new branch, with associated local contour coordinate  $s_i$ , begins, where  $i$  is the branch number. Branches can be arbitrarily subdivided into additional branches if needed. The paths of integration for the I-beam and channel cross section examples are shown in Figures 3.5(a) and 3.5(b), respectively. As shown in Figure 3.6, the contour has been represented by a series of points since the active OCSTWB code uses numerical integration to calculate the cross sectional stiffness and actuation constants. A sufficiently high contour point density is required to produce an accurate and converged solution.

Each branch requires six different entries in the `contour_input.m` input file. The first entry, `branch(i).branch_id`, is given a unique non-zero integer branch identification number  $i$ . The second entry, `branch(i).path_to_origin`, is set to a vector of branch numbers that identify the path to the contour origin, beginning with its connecting neighbour that is closest to the contour origin. If the branch connects directly to the contour origin, it is set to a value of [0]. The third and fourth entries, `branch(i).x2` and `branch(i).x3`, give the  $x_2$  and  $x_3$  coordinates, respectively, of the discretized contour branch points, beginning at  $s_i = 0$  and proceeding in order to the end of the branch. The fifth entry, `branch(i).laminates`, is set to the laminate identification number, contained in `LaminatesInput.dat`, of the laminate associated with each branch point. For the sixth entry, if the contour segment before the next contour point is of the same laminate type as

the present contour point, the present contour point is a continuous point in the laminate and is set to a space, ' '; otherwise, it is a transition point between laminates and is set to 'T', as shown in Figure 3.6.

As none of the current cross section examples have more than one laminate type in a branch, no transition points are needed; however, a cross section example used in Chapter 5 will need transition points. The contour input file for the extensional and bimoment I-beam cross section examples is included in Appendix B.2.1.

The `LaminatesInput.dat` input file begins with a `Number_of_Regions` entry that is set to the number of laminate types, called “regions,” used for the cross section. A region is a unique combination of a laminate ply lay-up and an applied electric field; it also includes elastic and electromechanical material properties, and ply thicknesses. The applied electric field  $E_1$  of a piezoelectric fibre composite material, used in Eq. 2.12, can be found by the relation [8]:

$$E_1 = \frac{V}{t_{electrodes}} \quad (3.2)$$

Each region block begins with a `Region` entry that is given the region/laminate identification number, the laminate thickness, and the number of plies in the laminate lay-up. The remainder of a region/laminate block consists of a `ply` entry for each ply in the laminate. The plies are given in order from  $\xi = -\frac{h}{2}$  to  $\xi = \frac{h}{2}$  where  $\xi$  is the through-the-thickness shell coordinate in the normal direction. Consequently, the direction of  $\xi$  and the resulting order of plies are functions of the direction of the contour coordinate  $s$ . A `ply` entry is given a ply identification number from one to the total number of plies in the laminate; the material name; the elastic properties of the orthotropic ply material; the ply thickness,  $t_{ply}$ ; the local ply angle  $\vartheta$  with respect to the axial coordinate  $x_1$ , as shown in Figure 2.2; the applied electric field  $E_1$ ; the electromechanical constants  $d_{1ij}$ ; and the material density.

The last entry, the material density, is not used in the code and can be set to unity. If the ply is passive, the electric field  $E_1$  and the electromechanical constants  $d_{1ij}$  are set to zero. The laminates input file for the bimoment I-beam cross section example is included in Appendix B.2.2.

The active OCSTWB code is executed by placing the contour and laminates input files in the same directory as the .m files that contain the code, and running the `calculate_stiffness_actuation.m` script in MATLAB. The output, which contains the terms of the  $5 \times 5$  cross sectional Vlasov stiffness matrix and the  $5 \times 1$  induced actuation vector, is displayed in the MATLAB Command Window, and is included in Appendix B.2.3 for the bimoment I-beam cross section example.

### 3.3 Results and Discussion

The direct stiffness terms of the stiffness matrix  $\mathbf{C}$  are the extensional  $C_{11}$ ; torsional  $C_{22}$ ; bending about the  $x_2$  and  $x_3$  axes,  $C_{33}$  and  $C_{44}$ , respectively; and Vlasov  $C_{55}$  stiffnesses. Generally, the results indicate that the direct stiffness terms are the dominant stiffness terms, while the coupling stiffness terms  $C_{ij}$ , where  $i \neq j$ , are mostly negligible.

The cross sectional stiffness results of the isotropic channel example, given in Table 3.4, show that there is an appreciable difference in results between all three cross section analysis codes. For the dominant stiffness terms, which include the direct stiffness terms and the  $C_{45}$  coupling term, the GT/VABS results are within 18.2% of the UM/VABS results, while the active OCSTWB code results are within 13.9% of those of UM/VABS and 2.3% of those of GT/VABS. Consequently, the relative amount of disagreement between the active OCSTWB code and the two FE codes, UM/VABS and GT/VABS, is similar to

**Table 3.4:** Cross sectional stiffness constants for the isotropic channel example predicted by UM/VABS, GT/VABS and the active OCSTWB code.

1. Isotropic Channel			
	UM/VABS	GT/VABS	Active OCSTWB
$C_{11}$	3.016E+11	3.120E+11 (+3.5% <sup>a</sup> )	3.016E+11 (0.0% <sup>a</sup> , -3.3% <sup>b</sup> )
$C_{22}$	1.568E+11	1.591E+11 (+1.5% <sup>a</sup> )	1.547E+11 (-1.4% <sup>a</sup> , -2.8% <sup>b</sup> )
$C_{33}$	1.220E+13	1.397E+13 (+14.6% <sup>a</sup> )	1.216E+13 (-0.3% <sup>a</sup> , -13.0% <sup>b</sup> )
$C_{44}$	2.340E+13	2.444E+13 (+4.5% <sup>a</sup> )	2.333E+13 (-0.3% <sup>a</sup> , -4.6% <sup>b</sup> )
$C_{55}$	5.549E+15	6.561E+15 (+18.2% <sup>a</sup> )	5.910E+15 (+6.5% <sup>a</sup> , -9.9% <sup>b</sup> )
$C_{12}$	0	0	0
$C_{13}$	-3.120E+7	≈0 (100% <sup>a</sup> )	-3.120E+7 (0.0% <sup>a</sup> , ∞% <sup>b</sup> )
$C_{14}$	≈0	≈0	≈0
$C_{15}$	≈0	≈0	≈0
$C_{23}$	0	0	0
$C_{24}$	0	0	0
$C_{25}$	0	0	0
$C_{34}$	-2.465E+2	≈0 (100% <sup>a</sup> )	≈0 (100% <sup>a</sup> , 0.0% <sup>b</sup> )
$C_{35}$	-1.572E+5	-1.031E+8 (+65500% <sup>a</sup> )	≈0 (100% <sup>a</sup> , 100% <sup>b</sup> )
$C_{45}$	3.300E+14	3.675E+14 (+11.4% <sup>a</sup> )	3.759E+14 (+13.9% <sup>a</sup> , 2.3% <sup>b</sup> )

<sup>a</sup> percent change with respect to UM/VABS.

<sup>b</sup> percent change with respect to GT/VABS.

the relative amount of disagreement between the two FE codes themselves.

As seen in Table 3.5 for the strip example, UM/VABS predicts significant values for the  $C_{12}$  stiffness term and the  $M_1^{(a)}$  induced actuation term, whereas the active OCSTWB code predicts these terms to be zero. This demonstrates a limitation of the active OCSTWB theory, where it cannot capture torsional couples induced by active layers within the thickness of a single composite lay-up due to the thin wall assumption. The extension-twist stiffness coupling  $C_{12}$  and induced torque  $M_1^{(a)}$  predicted by UM/VABS stem from the thickness-wise moment arm between the two lower +45° active plies and upper -45° active plies of the strip cross section example, given in Figure 3.1(b) and Table 3.3. This example was chosen only to demonstrate an aspect of the active OCSTWB theory; in a real active

OCSTWB application, twist would be induced using a built-up cross section of laminates separated by a distance proportional to  $a$  rather than using plies of a single laminate separated by a distance proportional to  $h$ , where  $a$  and  $h$  have been defined in Figure 1.3. The difference in results for the  $C_{24}$  term between UM/VABS and the active OCSTWB code is likely due to the thin wall assumption also. For the remaining dominant terms,  $C_{11}$ ,  $C_{22}$ ,  $C_{33}$ ,  $C_{44}$  and  $F_1^{(a)}$ , the active OCSTWB code results are within 5.7% of those of UM/VABS.

For the cruciform example results, given in Table 3.5, the active OCSTWB code is again unable to predict the  $C_{12}$  and  $M_1^{(a)}$  terms since the cruciform example is simply the previous active strip inverted, with two passive vertical walls added at the centre, shown in Figure 3.1(c) and Table 3.3. Consequently, the value of  $M_1^{(a)}$  predicted by UM/VABS for the cruciform is the same magnitude as the value predicted for the strip, but with opposite sign, as expected. The  $C_{11}$ ,  $C_{22}$  and  $C_{33}$  stiffness terms are much larger for the cruciform compared to the strip, as expected, due to the added stiffness given by the presence of vertical walls in the cruciform example. For the remaining dominant terms,  $C_{11}$ ,  $C_{22}$ ,  $C_{33}$ ,  $C_{44}$  and  $F_1^{(a)}$ , the active OCSTWB code results are within 1.7% of those of UM/VABS.

Both the extensional and bimoment I-beam examples have the same cross sectional stiffness properties, given in Table 3.6, as expected, since both have the same geometry and ply lay-ups, as shown in Figure 3.1(d) and Table 3.3. The bending stiffness about the  $x_2$  axis  $C_{33}$  is greater than about the  $x_3$  axis  $C_{44}$ , as would be expected of an I-beam. For the dominant stiffness terms,  $C_{11}$ ,  $C_{22}$ ,  $C_{33}$ ,  $C_{44}$  and  $C_{55}$ , the active OCSTWB results are within 2.1% of those of UM/VABS.

For the extensional I-beam, where all active plies are oriented in the  $x_1$  axial direction and have +2000 V applied, a pure axial induced extension force  $F_1^{(a)}$  is produced, shown in Table 3.7, as expected. For the dominant  $F_1^{(a)}$  term, the active OCSTWB code is within 0.2% of UM/VABS.

**Table 3.5:** Cross sectional stiffness and induced actuation constants of the strip and cruciform examples predicted by UM/VABS and the active OCSTWB code.

	2. Strip		3. Cruciform	
	UM/VABS	Active OCSTWB	UM/VABS	Active OCSTWB
$C_{11}$ [N]	4.956E+7	4.956E+7 (0.0%)	1.054E+8	1.054E+8 (0.0%)
$C_{22}$ [N·m <sup>2</sup> ]	8.571E+1	9.058E+1 (+5.7%)	1.569E+2	1.544E+2 (-1.6%)
$C_{33}$ [N·m <sup>2</sup> ]	2.771E+2	2.766E+2 (-0.2%)	5.027E+4	4.988E+4 (-0.6%)
$C_{44}$ [N·m <sup>2</sup> ]	4.127E+4	4.130E+4 (+0.1%)	4.155E+4	4.130E+4 (-0.6%)
$C_{55}$ [N·m <sup>4</sup> ]	2.301E-1	0 (100%)	4.766E-1	0 (100%)
$C_{12}$ [N·m]	3.727E+3	0 (100%)	-3.729E+3	0 (100%)
$C_{13}$ [N·m]	≈0	0	≈0	0
$C_{14}$ [N·m]	≈0	0	≈0	0
$C_{15}$ [N·m <sup>2</sup> ]	≈0	0	≈0	0
$C_{23}$ [N·m <sup>2</sup> ]	≈0	0	≈0	0
$C_{24}$ [N·m <sup>2</sup> ]	≈0	-9.909E+1 (∞%)	≈0	-9.909E+1 (∞%)
$C_{25}$ [N·m <sup>3</sup> ]	≈0	0	≈0	0
$C_{34}$ [N·m <sup>2</sup> ]	≈0	0	≈0	0
$C_{35}$ [N·m <sup>3</sup> ]	≈0	0	≈0	0
$C_{45}$ [N·m <sup>3</sup> ]	≈0	0	≈0	0
$F_1^{(a)}$ [N]	-2.795E+3	-2.741E+3 (+1.9%)	-2.800E+3	-2.848E+3 (-1.7%)
$M_1^{(a)}$ [N·m]	-1.357E+1	0 (100%)	1.358E+1	0 (100%)
$M_2^{(a)}$ [N·m]	≈0	0	≈0	0
$M_3^{(a)}$ [N·m]	≈0	0	≈0	0
$M_\omega^{(a)}$ [N·m <sup>2</sup> ]	≈0	0	≈0	0

For the bimoment I-beam, where all active plies are oriented in the  $x_1$  axial direction and have a checkered +2000 V / -2000 V voltage pattern applied to its flanges, a pure induced bimoment  $M_\omega^{(a)}$  is produced, shown in Table 3.7, as expected. For the dominant  $M_\omega^{(a)}$  term, the active OCSTWB code is within 1.5% of UM/VABS.

As seen in the channel results, given in Table 3.8, a large induced bending actuation about the  $x_3$  axis  $M_3^{(a)}$  is produced, as expected, due to the active plies oriented at 0° to the  $x_1$  direction in the flanges with opposite polarity voltages applied to the left and right flanges, shown in Figure 3.1(e) and Table 3.3. The channel is the most complicated of the cross section examples, as intended, since it produces more dominant terms than the

**Table 3.6:** Cross sectional stiffness constants of the extensional and bimoment I-beam examples predicted by UM/VABS and the active OCSTWB code.

	4. & 5. I-Beams	
	UM/VABS	Active OCSTWB
$C_{11}$ [N]	2.192E+8	2.183E+8 (-0.4%)
$C_{22}$ [N·m <sup>2</sup> ]	2.059E+2	2.017E+2 (-2.1%)
$C_{33}$ [N·m <sup>2</sup> ]	4.263E+5	4.233E+5 (-0.7%)
$C_{44}$ [N·m <sup>2</sup> ]	9.955E+4	9.912E+4 (-0.4%)
$C_{55}$ [N·m <sup>4</sup> ]	2.827E+2	2.880E+2 (+1.9%)
$C_{12}$ [N·m]	0	0
$C_{13}$ [N·m]	≈0	0
$C_{14}$ [N·m]	≈0	0
$C_{15}$ [N·m <sup>2</sup> ]	≈0	≈0
$C_{23}$ [N·m <sup>2</sup> ]	0	0
$C_{24}$ [N·m <sup>2</sup> ]	0	0
$C_{25}$ [N·m <sup>3</sup> ]	0	0
$C_{34}$ [N·m <sup>2</sup> ]	≈0	0
$C_{35}$ [N·m <sup>3</sup> ]	≈0	≈0
$C_{45}$ [N·m <sup>3</sup> ]	≈0	≈0

**Table 3.7:** Cross sectional induced actuation constants of the extensional and bimoment I-beam examples predicted by UM/VABS and the active OCSTWB code.

	4. Extensional I-Beam		5. Bimoment I-Beam	
	UM/VABS	Active OCSTWB	UM/VABS	Active OCSTWB
$F_1^{(a)}$ [N]	-2.341E+4	-2.338E+4 (+0.2%)	≈0	≈0
$M_1^{(a)}$ [N·m]	0	0	0	0
$M_2^{(a)}$ [N·m]	≈0	0	≈0	≈0
$M_3^{(a)}$ [N·m]	≈0	0	≈0	≈0
$M_\omega^{(a)}$ [N·m <sup>2</sup> ]	≈0	≈0	3.111E+1	3.158E+1 (+1.5%)

other cross section examples: five dominant direct stiffness terms, two dominant coupling stiffness terms  $C_{13}$  and  $C_{45}$ , and two dominant induced actuation terms  $M_3^{(a)}$  and  $M_\omega^{(a)}$ . For the dominant terms, the active OCSTWB code results are within 5.3% of those of UM/VABS.

For the  $C_{12}$  and  $C_{23}$  terms of Table 3.8, there is a large disagreement between the values

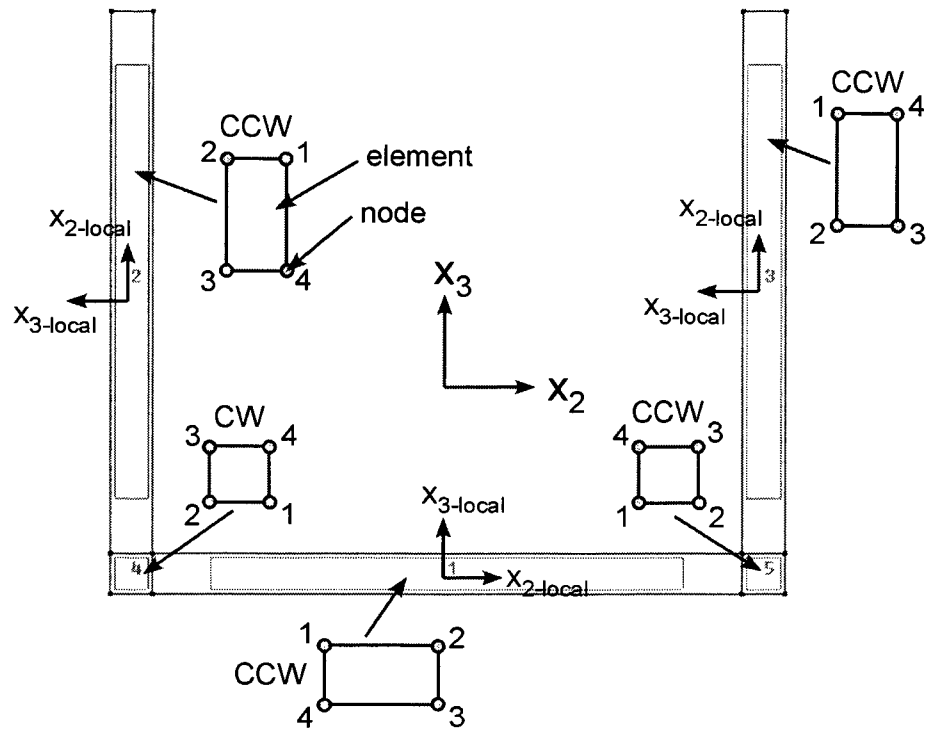
**Table 3.8:** Cross sectional stiffness and induced actuation constants of the channel example predicted by UM/VABS and the active OCSTWB code.

	6. Channel	
	UM/VABS	Active OCSTWB
$C_{11}$ [N]	1.881E+8	1.880E+8 (-0.1%)
$C_{22}$ [N·m <sup>2</sup> ]	2.778E+2	2.711E+2 (-2.4%)
$C_{33}$ [N·m <sup>2</sup> ]	1.966E+5	1.963E+5 (-0.2%)
$C_{44}$ [N·m <sup>2</sup> ]	4.393E+5	4.385E+5 (-0.2%)
$C_{55}$ [N·m <sup>4</sup> ]	2.744E+3	2.882E+3 (0.1%)
$C_{12}$ [N·m]	-1.479E+1	≈0 (100%)
$C_{13}$ [N·m]	6.299E+5	6.298E+5 (0.0%)
$C_{14}$ [N·m]	≈0	≈0
$C_{15}$ [N·m <sup>2</sup> ]	≈0	≈0
$C_{23}$ [N·m <sup>2</sup> ]	-4.287E+1	≈0 (100%)
$C_{24}$ [N·m <sup>2</sup> ]	≈0	≈0
$C_{25}$ [N·m <sup>3</sup> ]	≈0	≈0
$C_{34}$ [N·m <sup>2</sup> ]	≈0	≈0
$C_{35}$ [N·m <sup>3</sup> ]	≈0	≈0
$C_{45}$ [N·m <sup>3</sup> ]	3.197E+4	3.366E+4 (5.3%)
$F_1^{(a)}$ [N]	≈0	≈0
$M_1^{(a)}$ [N·m]	≈0	≈0
$M_2^{(a)}$ [N·m]	≈0	≈0
$M_3^{(a)}$ [N·m]	-9.381E+2	-9.377E+2 (0.0%)
$M_\omega^{(a)}$ [N·m <sup>2</sup> ]	-7.243E+1	-7.452E+1 (-2.3%)

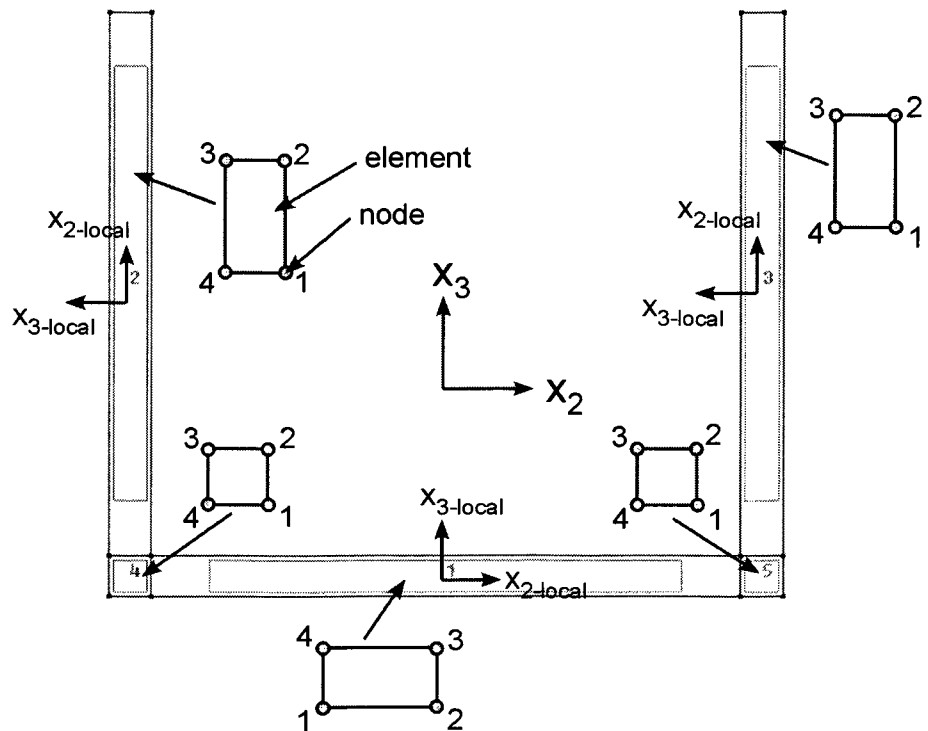
predicted by UM/VABS and the active OCSTWB code. However, these terms are much smaller, and therefore less important, than the other non-zero dominate terms. For the isotropic channel results, shown in Table 3.4, there is a large disagreement between some of the dominant coupling stiffness values predicted by UM/VABS and GT/VABS, such as  $C_{13}$  and  $C_{35}$ . As both UM/VABS and GT/VABS have been verified against experimental, literature and 3-D FEA data, the disagreement between some of coupling stiffness values predicted by the active OCSTWB code with those of UM/VABS does not invalidate the active OCSTWB code.

In the next chapter, cross section Examples 2 through 5 will be extended to full beam

examples, and additional beam examples will be introduced. The cross sectional constants will be used in a 1-D problem along the beam reference line to find the average beam extension, twist and deflection profiles at the beam reference line for the full beam examples. These results will be verified against either 3-D FEA or results available in the research literature. Various boundary conditions and applied mechanical loading will also be investigated, especially in regards to twisting an I-beam through bimoment actuation.

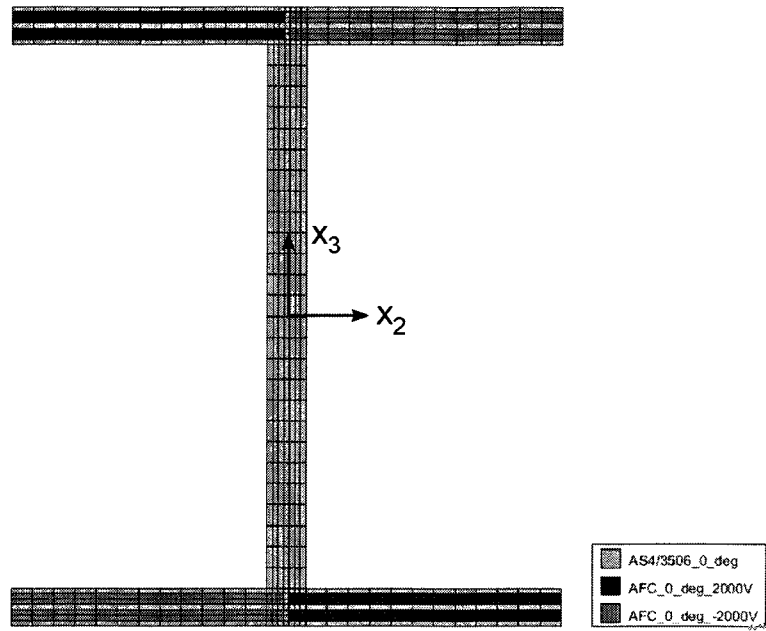


(a) Typical nodal connectivity orders, as coded by GiD.

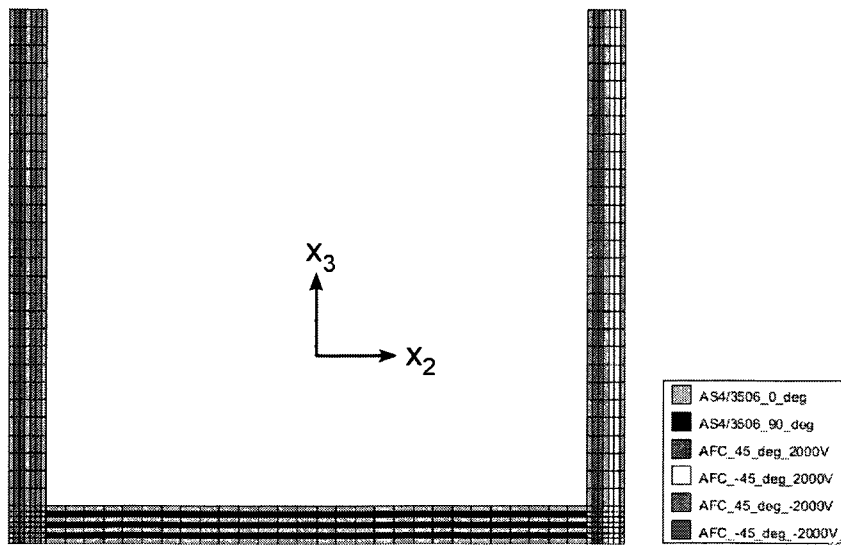


(b) Reordered nodal connectivities for the UM/VABS convention.

**Figure 3.3:** Nodal connectivity orders for the elements of each surface of a cross section.



(a) I-beam.



(b) Channel.

**Figure 3.4:** Material, ply angle and applied voltage assignments for the example cross sections.

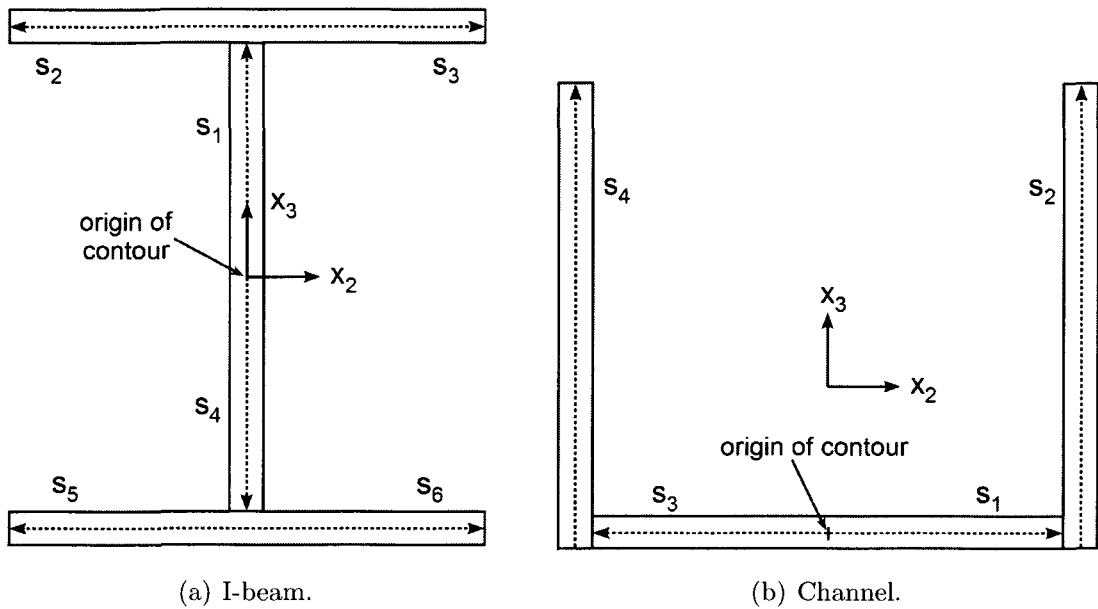


Figure 3.5: Discretized contours, paths of integration, and branches of the example cross sections.

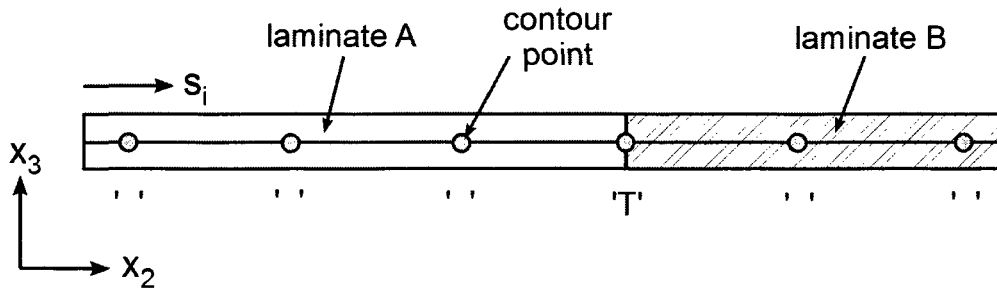


Figure 3.6: Identification of continuous contour points, 'o', and a transition contour point, 'T', in the region of two joining laminate types within a horizontal branch  $i$ .

# Chapter 4

## Investigation of Beam Displacement and Twist

In this chapter, the behaviour of the nonlinear 1-D problem along the beam reference line will be investigated using the cross sectional stiffness terms and induced actuation terms to obtain the beam displacement and twist at its reference line. Various beam examples will be presented, the solution of the nonlinear 1-D problem will be given, and the results will be validated against 3-D FEA.

### 4.1 Nonlinear 1-D Beam Problem Formulation

With the cross sectional constants evaluated, as discussed in Chapters 2 and 3, the global beam displacements and twist can be obtained by using them in a nonlinear 1-D problem along the beam reference line. Forces, moments and bimoments along the beam reference line are calculated by solving beam equilibrium equations. By discretizing the beam reference line by a number of beam elements, the strains at each node can then be obtained through the constitutive relation, Eq. 2.94, and used to find the relative change in the

orientation of the deformed basis  $\mathbf{B}$  between each pair of nodes, which can then be used to find beam displacements and twist.

For a Vlasov beam model, represented by Eq. 2.94, which is used for OCSTWB, the intrinsic static equilibrium equations are [23, 58]

$$\begin{aligned}
F'_1 - F_2 K_3 + F_3 K_2 + f_1 &= 0 \\
F'_2 - F_3 K_1 + F_1 K_3 + f_2 &= 0 \\
F'_3 - F_1 K_2 + F_2 K_1 + f_3 &= 0 \\
M'_1 - M_2 K_3 + M_3 K_2 - M''_\omega + m_1 &= 0 \\
M'_2 - M_3 K_1 + M_1 K_3 - (1 + \gamma_{11}) F_3 - K_3 M'_\omega + m_2 &= 0 \\
M'_3 - M_1 K_2 + M_2 K_1 + (1 + \gamma_{11}) F_2 - K_2 M'_\omega + m_3 &= 0
\end{aligned} \tag{4.1}$$

where  $K_i = k_i + \kappa_i$ , such that  $k_1$  is the initial beam twist, and  $k_2$  and  $k_3$  are the initial beam curvatures about the  $x_2$  and  $x_3$  axes, respectively;  $f_i$  are the body distributed forces in the  $x_i$  directions; and  $m_i$  are the body distributed moments about the  $x_i$  axes. For prismatic beams with no applied distributed forces or moments, one has  $k_i = 0$  and  $f_i = m_i = 0$ . To consider beams with initial twist and curvature, the active OCSTWB theory, given in Chapter 2, must be extended to include these features in addition to using non-zero  $k_i$  values in Eqs. 4.1 [19]. There are seven independent unknowns,  $F_1$ ,  $F_2$ ,  $F_3$ ,  $M_1$ ,  $M_2$ ,  $M_3$  and  $M_\omega$  in Eqs. 4.1. Whereas considering Eqs. 4.1, one has only six equations. An additional equation can be added to the set given in Eqs. 4.1 by considering the relations for  $\kappa_1$  and  $\kappa'_1$  as:

$$\begin{aligned}\kappa_1 &= S_{12}(F_1 - F_1^a) + S_{22}(M_1 - M_1^a) + S_{23}(M_2 - M_2^a) \\ &\quad + S_{24}(M_3 - M_3^a) + S_{25}(M_\omega - M_\omega^a)\end{aligned}\tag{4.2}$$

$$\begin{aligned}\kappa_1' &= S_{15}(F_1 - F_1^a) + S_{25}(M_1 - M_1^a) + S_{35}(M_2 - M_2^a) \\ &\quad + S_{45}(M_3 - M_3^a) + S_{55}(M_\omega - M_\omega^a)\end{aligned}\tag{4.3}$$

where these expressions for  $\kappa_1$  and  $\kappa_1'$  are obtained from the constitutive relation, Eq. 2.94. Differentiating Eq. 4.2 with respect to  $x_1$  and equating the resulting expression to the one given in Eq. 4.3 for  $\kappa_1'$ , yields the seventh intrinsic static beam equation, as

$$\begin{aligned}S_{12}F_1' + S_{22}M_1' + S_{23}M_2' + S_{24}M_3' + S_{25}M_\omega' - S_{15}(F_1 - F_1^a) \\ - S_{25}(M_1 - M_1^a) - S_{35}(M_2 - M_2^a) - S_{45}(M_3 - M_3^a) - S_{55}(M_\omega - M_\omega^a) = 0\end{aligned}\tag{4.4}$$

Adding Eq. 4.4 to Eqs. 4.1 and assuming small strain [19], such that  $(1 + \gamma_{11}) \approx 1$ , one can obtain the set of necessary intrinsic static equilibrium equations for a prismatic beam without any body forces or moments, as:

$$\begin{aligned}
F'_1 - F_2\kappa_3 + F_3\kappa_2 &= 0 \\
F'_2 - F_3\kappa_1 + F_1\kappa_3 &= 0 \\
F'_3 - F_1\kappa_2 + F_2\kappa_1 &= 0 \\
M'_1 - M_2\kappa_3 + M_3\kappa_2 - M''_\omega &= 0 \\
M'_2 - M_3\kappa_1 + M_1\kappa_3 - F_3 - \kappa_3M'_\omega &= 0 \\
M'_3 - M_1\kappa_2 + M_2\kappa_1 + F_2 - \kappa_2M'_\omega &= 0 \\
S_{12}F'_1 + S_{22}M'_1 + S_{23}M'_2 + S_{24}M'_3 + S_{25}M'_\omega - S_{15}(F_1 - F_1^a) & \quad (4.5) \\
-S_{25}(M_1 - M_1^a) - S_{35}(M_2 - M_2^a) - S_{45}(M_3 - M_3^a) - S_{55}(M_\omega - M_\omega^a) &= 0
\end{aligned}$$

The  $\kappa_i$  terms in Eqs. 4.5 can be replaced by their expressions in terms of  $F_i$ ,  $M_i$  and  $M_\omega$  using the constitutive relation, Eq. 2.94. Expanding Eq. 2.94 again, the relations for  $\kappa_2$  and  $\kappa_3$  are

$$\begin{aligned}
\kappa_2 &= S_{13}(F_1 - F_1^a) + S_{23}(M_1 - M_1^a) + S_{33}(M_2 - M_2^a) \\
&\quad + S_{34}(M_3 - M_3^a) + S_{35}(M_\omega - M_\omega^a) \quad (4.6)
\end{aligned}$$

$$\begin{aligned}
\kappa_3 &= S_{14}(F_1 - F_1^a) + S_{24}(M_1 - M_1^a) + S_{34}(M_2 - M_2^a) \\
&\quad + S_{44}(M_3 - M_3^a) + S_{45}(M_\omega - M_\omega^a) \quad (4.7)
\end{aligned}$$

To solve the intrinsic static beam equations, Eqs. 4.5, the beam reference line is discretized, as shown in Figure 4.1. Each of the  $n$  nodes are spaced evenly by a distance  $\Delta x_1$ . A first-order accurate finite difference scheme is used to solve the intrinsic static beam equations.

Attempts were made to solve Eqs. 4.5 using various finite element methods, such as the Galerkin weighted residual method and the least-squares method. Higher accuracy, faster convergence, and a mathematically more elegant solution compared with the finite difference method were the motivating factors behind the efforts to develop a FE solution scheme. The second order term  $M''_{\omega}$  in Eqs. 4.5, which is only present in the intrinsic static equilibrium equations derived for a Vlasov beam model, is the source of the difficulty in developing a stable and convergent FE solution scheme. Using the least-squares method, the boundary conditions were always satisfied, but small changes in input values or the number of elements used caused large variations in the results. The problem was ill-posed since the derived Jacobian was not full rank. To correct this problem, the residuals must be normalized in a specific way. This is a mathematical problem with no rigorous procedure available to find how these residuals must be normalized. A second-order accurate finite difference scheme was also attempted; however, due to possible singularities in the Jacobian, this scheme also gave divergent results for some cross sectional inputs.

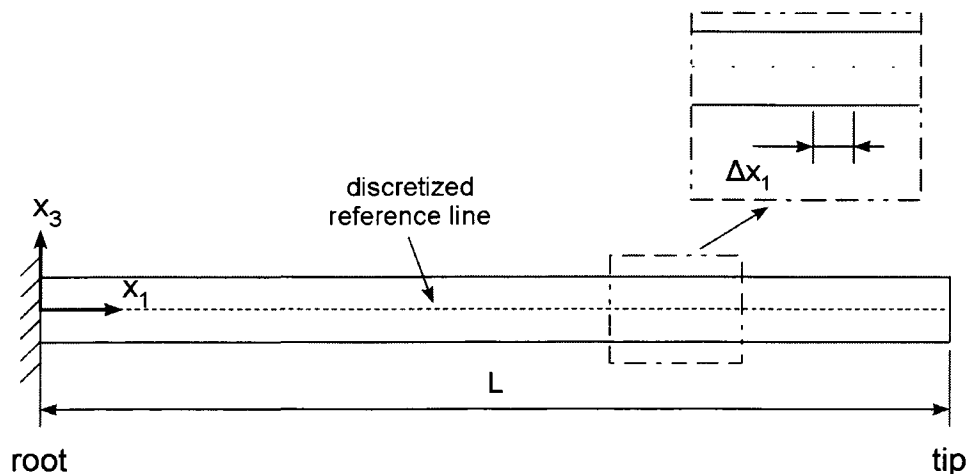


**Figure 4.1:** Profile view of a beam with a discretized beam reference line.

Substituting Eqs. 4.2, 4.6 and 4.7 into Eqs. 4.5 and discretizing as a forward difference

scheme, yields

$$\begin{aligned} & \frac{F_1^{j+1} - F_1^j}{\Delta x_1} - F_2^j [S_{14} (F_1 - F_1^a) + S_{24} (M_1 - M_1^a) + S_{34} (M_2 - M_2^a) \\ & + S_{44} (M_3 - M_3^a) + S_{45} (M_\omega - M_\omega^a)] + F_3^j [S_{13} (F_1 - F_1^a) + S_{23} (M_1 - M_1^a) \\ & + S_{33} (M_2 - M_2^a) + S_{34} (M_3 - M_3^a) + S_{35} (M_\omega - M_\omega^a)] = 0 \end{aligned} \quad (4.8a)$$

$$\begin{aligned} & \frac{F_2^{j+1} - F_2^j}{\Delta x_1} - F_3^j [S_{12} (F_1 - F_1^a) + S_{22} (M_1 - M_1^a) + S_{23} (M_2 - M_2^a) \\ & + S_{24} (M_3 - M_3^a) + S_{25} (M_\omega - M_\omega^a)] + F_1^j [S_{14} (F_1 - F_1^a) + S_{24} (M_1 - M_1^a) \\ & + S_{34} (M_2 - M_2^a) + S_{44} (M_3 - M_3^a) + S_{45} (M_\omega - M_\omega^a)] = 0 \end{aligned} \quad (4.8b)$$

$$\begin{aligned} & \frac{F_3^{j+1} - F_3^j}{\Delta x_1} - F_1^j [S_{13} (F_1 - F_1^a) + S_{23} (M_1 - M_1^a) + S_{33} (M_2 - M_2^a) \\ & + S_{34} (M_3 - M_3^a) + S_{35} (M_\omega - M_\omega^a)] + F_2^j [S_{12} (F_1 - F_1^a) + S_{22} (M_1 - M_1^a) \\ & + S_{23} (M_2 - M_2^a) + S_{24} (M_3 - M_3^a) + S_{25} (M_\omega - M_\omega^a)] = 0 \end{aligned} \quad (4.8c)$$

$$\begin{aligned} & \frac{M_1^{j+1} - M_1^j}{\Delta x_1} - \frac{W^{j+1} - W^j}{\Delta x_1} - M_2^j [S_{14} (F_1 - F_1^a) + S_{24} (M_1 - M_1^a) \\ & + S_{34} (M_2 - M_2^a) + S_{44} (M_3 - M_3^a) + S_{45} (M_\omega - M_\omega^a)] + M_3^j [S_{13} (F_1 - F_1^a) \\ & + S_{23} (M_1 - M_1^a) + S_{33} (M_2 - M_2^a) + S_{34} (M_3 - M_3^a) + S_{35} (M_\omega - M_\omega^a)] = 0 \end{aligned} \quad (4.8d)$$

$$\begin{aligned}
& \frac{M_2^{j+1} - M_2^j}{\Delta x_1} - M_3^j [S_{12} (F_1 - F_1^a) + S_{22} (M_1 - M_1^a) + S_{23} (M_2 - M_2^a) \\
& + S_{24} (M_3 - M_3^a) + S_{25} (M_\omega - M_\omega^a)] + M_1^j [S_{14} (F_1 - F_1^a) + S_{24} (M_1 - M_1^a) \quad (4.8e) \\
& + S_{34} (M_2 - M_2^a) + S_{44} (M_3 - M_3^a) + S_{45} (M_\omega - M_\omega^a)] - F_3^j - W^j [S_{14} (F_1 - F_1^a) \\
& + S_{24} (M_1 - M_1^a) + S_{34} (M_2 - M_2^a) + S_{44} (M_3 - M_3^a) + S_{45} (M_\omega - M_\omega^a)] = 0
\end{aligned}$$

$$\begin{aligned}
& \frac{M_3^{j+1} - M_3^j}{\Delta x_1} - M_1^j [S_{13} (F_1 - F_1^a) + S_{23} (M_1 - M_1^a) + S_{33} (M_2 - M_2^a) \\
& + S_{34} (M_3 - M_3^a) + S_{35} (M_\omega - M_\omega^a)] + M_2^j [S_{12} (F_1 - F_1^a) + S_{22} (M_1 - M_1^a) \quad (4.8f) \\
& + S_{23} (M_2 - M_2^a) + S_{24} (M_3 - M_3^a) + S_{25} (M_\omega - M_\omega^a)] - F_2^j + W^j [S_{13} (F_1 - F_1^a) \\
& + S_{23} (M_1 - M_1^a) + S_{33} (M_2 - M_2^a) + S_{34} (M_3 - M_3^a) + S_{35} (M_\omega - M_\omega^a)] = 0
\end{aligned}$$

$$\begin{aligned}
& S_{12} \frac{F_1^{j+1} - F_1^j}{\Delta x_1} + S_{22} \frac{M_1^{j+1} - M_1^j}{\Delta x_1} + S_{23} \frac{M_2^{j+1} - M_2^j}{\Delta x_1} + S_{24} \frac{M_3^{j+1} - M_3^j}{\Delta x_1} + S_{25} W^j \\
& - S_{15} (F_1 - F_1^a) - S_{25} (M_1 - M_1^a) - S_{35} (M_2 - M_2^a) \quad (4.8g) \\
& - S_{45} (M_3 - M_3^a) - S_{55} (M_\omega - M_\omega^a) = 0
\end{aligned}$$

$$W^j - \frac{M_\omega^{j+1} - M_\omega^j}{\Delta x_1} = 0 \quad (4.8h)$$

where a change of variables have been made,  $W = M'_\omega$ , in order to recast the problem into a first-order form. This results in an additional equation, Eq. 4.8h.

## 4.2 Beam Examples

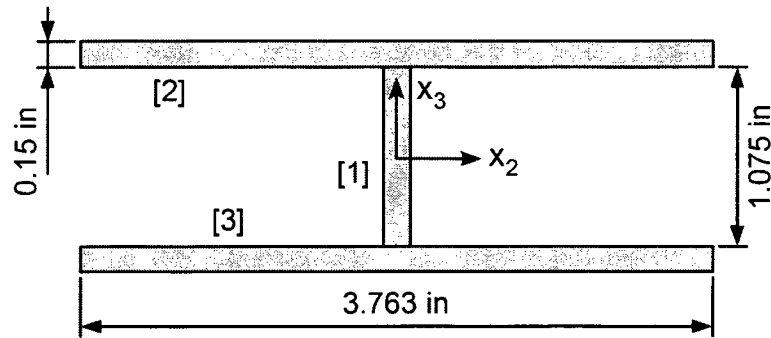
Fourteen OCSTWB examples have been used to verify the active OCSTWB code, as summarized in Table 4.1. The first four examples, passive isotropic I-beams with applied mechanical bimoments and torque, were taken from reference [1], where the authors have presented the corresponding twist profile results along the beams' reference lines. Examples 5 through 13, are beams with cross sections given previously in Table 3.1. In all cases, the spans of the beams are at least ten times their characteristic cross sectional dimension  $a$  to satisfy the slenderness assumption used by the VAM, Eq. 1.3. Examples 9 through 13, are used to investigate various boundary conditions and applied mechanical loading for the anisotropic I-beam example. Additionally, Example 12 is used to study the effect of reversing the electrical polarity, and thus the sign of the induced bimoment, at the beam midspan. This was done by reversing the sign of the induced bimoment  $M_{\omega}^{(a)}$  for the nodes of the outer half of the beam span,  $\frac{L}{2} < x_1 \leq L$ . Examples 9 and 11 have the same laminate ply lay-up as the other anisotropic I-beams, such as Example 8, except that the applied voltages have been removed, thereby causing the induced bimoment actuation term to become zero.

Beams 1 through 4 have the same isotropic cross section, as shown in Figure 4.2. The material properties used for the isotropic I-beams are:  $E = 10.6E+6 \text{ lb}_f/\text{in}^2$ ,  $G = 3.98E+6 \text{ lb}_f/\text{in}^2$  and  $\nu = 0.33$ .

The applied mechanical loading and boundary conditions for the beam examples are summarized in Table 4.2. For the isotropic I-beam, the mechanical bimoments are applied by a set of normal axial forces positioned at the tip,  $F^t$ , and root,  $F^r$ , flange edges, as shown in Figure 4.3. In order to verify the active OCSTWB code, the value of the mechanical torque  $T$ , that was applied at the tip of beam 4, was selected such that it would recreate the plot in reference [1]. The values of the mechanical bimoments  $M_{\omega}$

**Table 4.1:** Summary of the beam examples investigated.

	Type	Cross Section	Length	Laminate Lay-up	Active or Passive
1.	I-beam (lit.)	Figure 4.2	62 in	Isotropic	Passive
2.	I-beam (lit.)	Figure 4.2	62 in	Isotropic	Passive
3.	I-beam (lit.)	Figure 4.2	62 in	Isotropic	Passive
4.	I-beam (lit.)	Figure 4.2	62 in	Isotropic	Passive
5.	Strip	Figure 3.1(b)	1 m	Table 3.3 - 2.	Active
6.	Cruciform	Figure 3.1(c)	1 m	Table 3.3 - 3.	Active
7.	I-beam (ext.)	Figure 3.1(d)	1 m	Table 3.3 - 4.	Active
8.	I-beam (bimo.)	Figure 3.1(d)	1 m	Table 3.3 - 5.	Active
9.	I-beam (bimo.)	Figure 3.1(d)	1 m	Table 3.3 - I-Beam	Passive
10.	I-beam (bimo.)	Figure 3.1(d)	1 m	Table 3.3 - 5.	Active
11.	I-beam (bimo.)	Figure 3.1(d)	1 m	Table 3.3 - I-Beam	Passive
12.	I-beam (bimo.)	Figure 3.1(d)	1 m	Table 3.3 - 5. Reversed	Active
13.	I-beam (bimo.)	Figure 3.1(d)	1 m	Table 3.3 - 5.	Active

**Figure 4.2:** Cross section of the isotropic I-beam from [1].

applied at the tips of Examples 9 and 11, were chosen to be about the same as the induced bimoments  $M_{\omega}^{(a)}$  produced for the active bimoment anisotropic I-beam examples, given in Table 3.7. This would allow for comparison of twist profiles between the application of a bimoment through active induction and mechanically at the beam ends. The free to warp root boundary condition used for Examples 10 through 13 will determine if the reduction in torsional stiffness will lead to greater twist, as discussed in [1].

Examples 1 through 4, were analysed using the active OCSTWB code and the results were compared against the literature results; and Examples 5 through 13, were analysed

**Table 4.2:** Applied mechanical loading and boundary conditions for the beam examples.

Boundary Conditions		Applied Mechanical Loading	
Root	Tip	Root	Tip
1. Web restrained	Free	$F^r = 400 \text{ lb}_f$	$F^t = 0$
2. Web restrained	Free	$F^r = 0$	$F^t = 400 \text{ lb}_f$
3. Web restrained	Free	$F^r = 400 \text{ lb}_f$	$F^t = 400 \text{ lb}_f$
4. Web restrained	Free	$F^r = 0$	$F^t = 0, T = 30.1 \text{ lb}_f \cdot \text{in}$
5. Restrained	Free		
6. Restrained	Free		
7. Restrained	Free		
8. Restrained	Free		
9. Restrained	Free		
10. Restrained	Free		$M_\omega = -30 \text{ N} \cdot \text{m}^2$
11. Free to warp	Free		
12. Free to warp	Free		$M_\omega = -30 \text{ N} \cdot \text{m}^2$
13. Free to warp	Free		
14. Free to warp	Restrained warping		

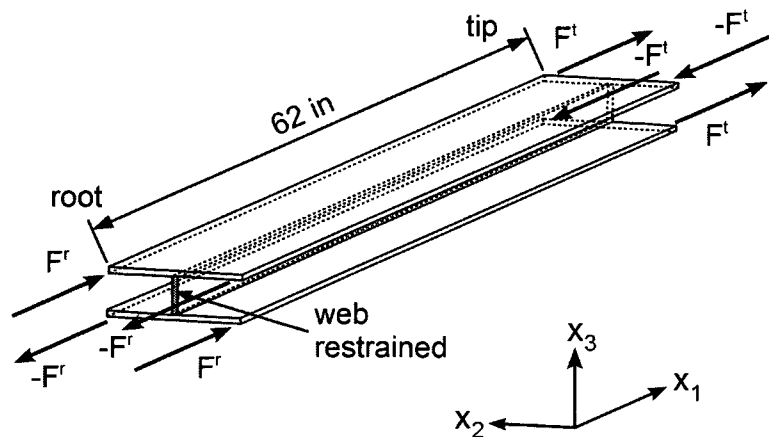


**Figure 4.3:** 3-D model of the isotropic I-beam example with boundary conditions, and applied mechanical forces at both tip and root.

by 3-D FEA, UM/VABS and the active OCSTWB code. In the following section, the nonlinear 1-D problem along the beam reference line and the analysis of the beam examples using 3-D FEA will be discussed.

### 4.3 Boundary Conditions and Applied Loading

Boundary conditions and applied loading must be expressed in terms of the unknown forces, moments and bimoment variables,  $F_i$ ,  $M_i$  and  $M_\omega$ , respectively, in order to include them in the finite difference scheme. For the discrete set of normal axial forces applied to the isotropic I-beam flanges at the root,  $F^r$  and tip,  $F^t$ , shown in Figure 4.3, the resulting mechanical bimoments are  $M_\omega^r$  at the root, and  $M_\omega^t$  at the tip. Following the theory given in [26], a bimoment can be expressed as

$$M_\omega = \int_{\Sigma} \omega \sigma_{x_1} h \, ds \quad (4.9)$$

where  $\omega$  is a warping function,  $\sigma_{x_1}$  are the normal axial stresses in the beam, and  $h$  is the wall thickness. The warping function  $\omega$  depends on the cross section geometry and is given by [26]

$$\omega = \omega_o - \int r_n \, ds \quad (4.10)$$

where  $\omega_o$  is the initial value of  $\omega$  and is zero at the origin of the contour  $s_o$ . As required by Eq. 3.1, the origin of the contour is coincident with the area centroid for an I-beam, as shown in Figure 4.4. Substituting the second relation of Eqs. 2.3 into Eq. 4.10, yields

$$\omega = \omega_o - \int \mathbf{n} \cdot \mathbf{r} \, ds \quad (4.11)$$

where the unit normal vector  $\mathbf{n}$  is given by the third relation of Eqs. 2.1 and is included in Figure 4.4 along with the contour position vector  $\mathbf{r}$ . The warping function along the third branch  $s_3$  is given by

$$\begin{aligned}
 \omega(s_3) &= 0 - \int_0^{s_3} 0 \, ds \\
 &= 0
 \end{aligned}
 \tag{4.12}$$

for the second branch  $s_2$ ,

$$\begin{aligned}
 \omega(s_2) &= \omega(s_3 = g) - \int_0^{s_2} -g \, ds \\
 &= gs_2
 \end{aligned}
 \tag{4.13}$$

and for the remaining branches, the warping function is given in Table 4.3.

A positive axial force  $F$  is directed in the positive  $x_1$  direction and vice-versa, as shown in Figure 4.3 and Table 4.3. As stress is related to linearized strain by  $\sigma_{x_1} = E \frac{\partial u_{x_1}}{\partial x_1}$ , a positive axial force at the beam root,  $F^r$ , produces compression in the flange and thus negative stress. However, a positive axial force at the tip,  $F^t$ , produces tension in the flange and thus positive stress, as indicated in Table 4.3.

**Table 4.3:** Warping functions and applied axial stresses for each branch of an I-beam cross section.

Branch	$\omega$	Axial force	$\sigma_{x_1}$	
			Root	Tip
$s_1$	$-gs_1$	$-F$	$\sigma_{x_1}$	$-\sigma_{x_1}$
$s_2$	$gs_2$	$F$	$-\sigma_{x_1}$	$\sigma_{x_1}$
$s_3$	0			
$s_4$	0			
$s_5$	$gs_5$	$F$	$-\sigma_{x_1}$	$\sigma_{x_1}$
$s_6$	$-gs_6$	$-F$	$\sigma_{x_1}$	$-\sigma_{x_1}$

As the normal axial forces,  $F^r$  and  $F^t$ , are applied at the flange edges, the only contributions to the integral of Eq. 4.9 are at the four discrete flange edges, such that, at the

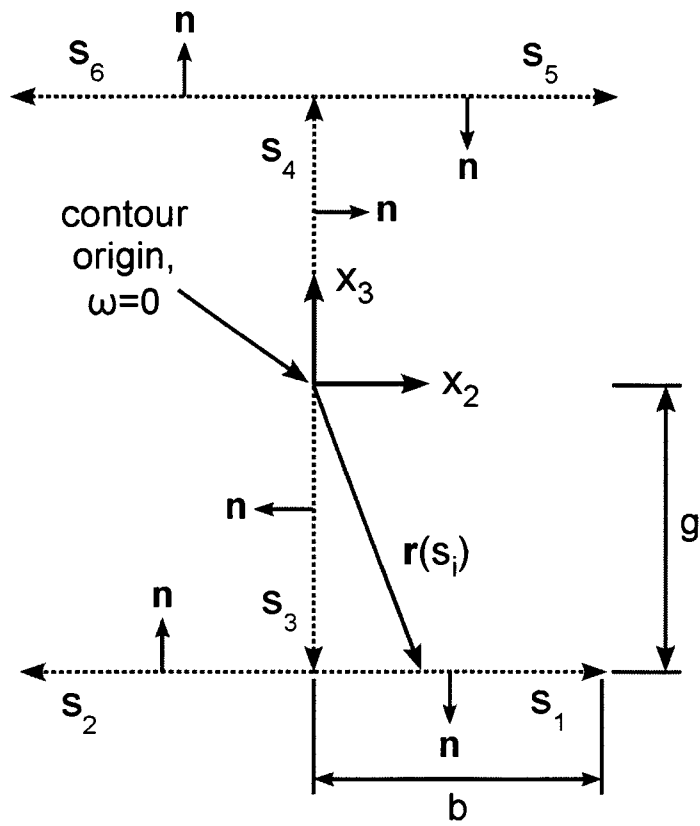


**Figure 4.4:** Cross sectional parameters of an I-beam used to construct a warping function.

root

$$\begin{aligned}
 M_{\omega}^r &= \sum_{i=1,2,5,6} \omega(s_i = b) F^r(s_i = b) \\
 &= -4gbF^r
 \end{aligned}
 \tag{4.14}$$

and at the tip

$$\begin{aligned}
M_{\omega}^t &= \sum_{i=1,2,5,6} \omega(s_i = b) F^t(s_i = b) \\
&= 4gbF^t
\end{aligned} \tag{4.15}$$

For the isotropic I-beam examples, beam Examples 1 through 4, given in Table 4.2 and Figures 4.2 and 4.3, the evaluated applied mechanical bimoment values at the root and tip are given in Table 4.4.

**Table 4.4:** Applied mechanical bimoment values at the root and tip for the isotropic I-beam examples.

	$M_{\omega}^r$ [lb <sub>f</sub> ·in <sup>2</sup> ]	$M_{\omega}^t$ [lb <sub>f</sub> ·in <sup>2</sup> ]
1.	-1844	0
2.	0	1844
3.	-922	922
4.	0	0

As discussed in [59], a free to warp root boundary condition is applied by setting the bimoment at the root node to zero,  $M_{\omega}^1 = 0$ . The condition that the beam root has zero twist,  $\theta(x_1 = 0) = 0$ , is applied during the post-processing of the finite difference results. A mechanical bimoment at a free to warp root can be applied by directly setting the root bimoment to the value of the applied bimoment,  $M_{\omega}^1 = M_{\omega}^r$ , and likewise, a mechanical bimoment can be applied at a free tip by setting  $M_{\omega}^n = M_{\omega}^t$ . A restrained root end requires that warping at the beam end be restrained, such that  $\kappa_1 = \theta' = 0$  [23, 26, 59]. Using Eq. 4.2, the restrained root boundary condition can be expressed in terms of the unknown forces, moments and bimoment,  $F_i$ ,  $M_i$  and  $M_{\omega}$ , as

$$\begin{aligned}
S_{12} (F_1^1 - F_1^a) + S_{22} (M_1^1 - M_1^a) + S_{23} (M_2^1 - M_2^a) \\
+S_{24} (M_3^1 - M_3^a) + S_{25} (M_\omega^1 - M_\omega^a) = 0
\end{aligned} \tag{4.16}$$

and likewise for a restrained warping boundary condition at the tip, as

$$\begin{aligned}
S_{12} (F_1^n - F_1^a) + S_{22} (M_1^n - M_1^a) + S_{23} (M_2^n - M_2^a) \\
+S_{24} (M_3^n - M_3^a) + S_{25} (M_\omega^n - M_\omega^a) = 0
\end{aligned} \tag{4.17}$$

The total torque  $T$  in a beam is the sum of the Vlasov torque  $-M'_\omega$  and the Saint-Venant torque  $M_1$ , such that  $T = -M'_\omega + M_1$  [26, 59]. After the change of variables,  $W = M'_\omega$ , and rearranging,  $M_1 = W + T$ . At the tip,  $M_1^n = W^n + T$ , where any applied mechanical torque must be equal to the total torque  $T$ . Moreover, at a free end,  $F_1^n = F_2^n = F_3^n = M_2^n = M_3^n = M_\omega^n = 0$  and  $M_1^n = W^n$  [23].

## 4.4 Beam Displacements

The finite difference equations formed at the root, interior and tip nodes are given in Table 4.5. These equations form a linearly independent set of equations that are neither overdetermined nor underdetermined. They were solved numerically using the Newton-Raphson method [60].

Once the forces, moments and bimoments,  $F_i$ ,  $M_i$  and  $M_\omega$ , have been solved for at each node, the corresponding strains can be obtained using the beam constitutive relation, Eq. 2.94. To determine beam displacements and twists, first it is necessary to use the

**Table 4.5:** Beam equations applied to each node of a discretized beam reference line.

	Root Node, 1	Interior Nodes	Tip Node, $n$
i.	Eq. 4.8b	Eq. 4.8b	$F_1^n = 0$
ii.	Eq. 4.8c	Eq. 4.8c	$F_2^n = 0$
iii.	Eq. 4.8d	Eq. 4.8d	$F_3^n = 0$
iv.	Eq. 4.8e	Eq. 4.8e	$M_1^n = W^n + T$
v.	Eq. 4.8f	Eq. 4.8f	$M_2^n = 0$
vi.	Eq. 4.8g	Eq. 4.8g	$M_3^n = 0$
vii.	Eq. 4.8h	Eq. 4.8h	a) Free: $M_\omega^n = 0$ b) Mechanical bimoment: $M_\omega^n = M_\omega^t$ c) Restrained warping: $\kappa_1 = 0$ , Eq. 4.17
viii.	Eq. 4.8h	Eq. 4.8h	
ix.	a) Free to warp: $M_\omega^1 = 0$ b) Mechanical bimoment: $M_\omega^1 = M_\omega^r$ c) Restrained: $\kappa_1 = 0$ , Eq. 4.16		

computed strains at each node to construct rotation, or direction cosine, matrices that relate the change in orientation of the deformed basis  $\mathbf{B}$  between each pair of nodes [19]. In reference to Figure 1.5, let a rotation matrix  $\mathbf{C}^{Bb}$  represent the change in orientation between an undeformed point on the beam reference line, in basis  $\mathbf{b}$ , to its final deformed orientation, in basis  $\mathbf{B}$ . The rotation matrix of a node  $j + 1$  is related to the rotation matrix of its neighbouring node  $j$ , as

$$\mathbf{C}^{Bb(j+1)} = \Delta \mathbf{C}^{Bb(j+1)} \mathbf{C}^{Bb(j)} \quad (4.18)$$

where  $\Delta \mathbf{C}^{Bb(j+1)}$  is the change in orientation between the two deformed neighbouring nodes due to twist and bending strains. At the beam root, where rotation is constrained to zero,  $\theta = 0$ , and  $\mathbf{C}^{Bb(1)}$  consequently becomes the identity matrix  $\mathbf{I}$ . The change in orientation matrix  $\Delta \mathbf{C}^{Bb(j+1)}$  can be expressed as an exponential power series, as [19]

$$\begin{aligned}\Delta C^{Bb} &= e^{-\tilde{\Phi}} \\ &= \mathbf{I} - \tilde{\Phi} + \frac{1}{2}\tilde{\Phi}\tilde{\Phi} - \frac{1}{6}\tilde{\Phi}\tilde{\Phi}\tilde{\Phi} + \dots\end{aligned}\quad (4.19)$$

where  $\Phi^T = \begin{bmatrix} e_1\alpha & e_2\alpha & e_3\alpha \end{bmatrix}$  is the finite rotation vector, the tilde is the skew-symmetric operator, which transforms a vector to a matrix, as

$$\tilde{\Phi} = \begin{bmatrix} 0 & -e_3\alpha & e_2\alpha \\ e_3\alpha & 0 & -e_1\alpha \\ -e_2\alpha & e_1\alpha & 0 \end{bmatrix}\quad (4.20)$$

and  $e^T = \begin{bmatrix} e_1 & e_2 & e_3 \end{bmatrix}$  is a unit vector about which a rotation  $\alpha$  occurs. The numerical efficiency can be increased by transforming the power series expression for  $\Delta C^{Bb}$  in Eq. 4.19 to an alternative form using Padé approximation to read [61]

$$\Delta C^{Bb} = \left(\mathbf{I} + \frac{1}{2}\tilde{\Phi}\right)^{-1} \left(\mathbf{I} - \frac{1}{2}\tilde{\Phi}\right) + \mathcal{O}(\tilde{\Phi}^3)\quad (4.21)$$

Terms of  $\mathcal{O}(\tilde{\Phi}^3)$  and higher will be neglected in Eq. 4.21 since small strain has been assumed. As the strains,  $\kappa_1$ ,  $\kappa_2$  and  $\kappa_3$ , represent the twist and bending rotations per unit beam length, the finite rotation matrix, Eq. 4.20, can be rewritten in terms of the nodal strains, as

$$\tilde{\Phi} = \Delta x_1 \begin{bmatrix} 0 & -\kappa_3 & \kappa_2 \\ \kappa_3 & 0 & -\kappa_1 \\ -\kappa_2 & \kappa_1 & 0 \end{bmatrix}\quad (4.22)$$

where  $\Delta x_1$  is the separation distance between nodes. Substituting Eqs. 4.21 and 4.22 into

Eq. 4.18, yields

$$\mathbf{C}^{\mathbf{Bb}(j+1)} = \left( \frac{1}{\Delta x_1} \mathbf{I} + \frac{1}{2} \begin{bmatrix} 0 & -\kappa_3^{(j+1)} & \kappa_2^{(j+1)} \\ \kappa_3^{(j+1)} & 0 & -\kappa_1^{(j+1)} \\ -\kappa_2^{(j+1)} & \kappa_1^{(j+1)} & 0 \end{bmatrix} \right)^{-1} \left( \frac{1}{\Delta x_1} \mathbf{I} - \frac{1}{2} \begin{bmatrix} 0 & -\kappa_3^{(j+1)} & \kappa_2^{(j+1)} \\ \kappa_3^{(j+1)} & 0 & -\kappa_1^{(j+1)} \\ -\kappa_2^{(j+1)} & \kappa_1^{(j+1)} & 0 \end{bmatrix} \right) \mathbf{C}^{\mathbf{Bb}(j)} \quad (4.23)$$

Beginning at the root node, where  $\mathbf{C}^{\mathbf{Bb}(1)} = \mathbf{I}$ , Eq. 4.23 can be evaluated iteratively to find the deformed orientation of each node. The beam twist  $\phi$  at each node can be calculated by rotating the undeformed unit vector,  $\mathbf{b}_3 = \begin{bmatrix} 0 & 0 & 1 \end{bmatrix}^T$ , by  $\mathbf{C}^{\mathbf{Bb}}$ , such that  $\mathbf{B}_3 = \mathbf{C}^{\mathbf{Bb}} \mathbf{b}_3$ , as shown in Figure 4.5. The resulting components of the deformed vector,  $\mathbf{B}_3 = \begin{bmatrix} C_{1,3}^{\mathbf{Bb}} & C_{2,3}^{\mathbf{Bb}} & C_{3,3}^{\mathbf{Bb}} \end{bmatrix}^T$ , can be used to calculate the twist at each node, as

$$\phi^j = \frac{180^\circ}{\pi} \arctan \frac{C_{2,3}^{\mathbf{Bb}(j)}}{C_{3,3}^{\mathbf{Bb}(j)}} \quad (4.24)$$

where the subscripts denote the row and column entries of the rotation matrix  $\mathbf{C}^{\mathbf{Bb}}$ .

The strains in the deformed basis  $\mathbf{B}$  are given by [19]

$$\boldsymbol{\gamma} = \mathbf{C}^{\mathbf{Bb}} (\mathbf{e}_1 + \mathbf{u}' + \tilde{\mathbf{k}} \mathbf{u}) - \mathbf{e}_1 \quad (4.25)$$

where  $\boldsymbol{\gamma} = \begin{bmatrix} \gamma_{11} & 2\gamma_{12} & 2\gamma_{13} \end{bmatrix}^T$ ,  $\mathbf{e}_1 = \begin{bmatrix} 1 & 0 & 0 \end{bmatrix}^T$ ,  $\mathbf{u}'$  is the displacement vector differentiated with respect to  $x_1$ ,  $\tilde{\mathbf{k}}$  is a skew-symmetric matrix of the components of initial twist and curvature, and  $\mathbf{u} = \begin{bmatrix} u_1 & u_2 & u_3 \end{bmatrix}^T$  is the displacement vector in the  $\mathbf{b}$  basis. In the absence of initial twist and curvature,  $\tilde{\mathbf{k}} = \mathbf{0}$ . Neglecting global shear strains, as

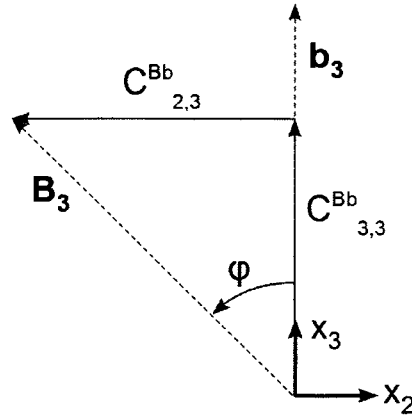


**Figure 4.5:** Angle of a deformed reference frame  $\mathbf{B}_i$  at a particular axial position  $x_1$  relative to the undeformed reference frame  $\mathbf{b}_i$ .

discussed in Chapter 1, results in  $\gamma_{12} = \gamma_{13} = 0$ , and recognizing that  $\gamma_{11}$  is the strain in the  $\mathbf{B}_1$  direction, the displacements of each node in the undeformed  $\mathbf{b}$  basis are given by

$$\mathbf{u}^{j+1} = \mathbf{u}^j + (\mathbf{C}^{Bb(j+1)})^{-1} \begin{bmatrix} (\gamma_{11}^{j+1} + 1) \Delta x_1 \\ 0 \\ 0 \end{bmatrix} - \begin{bmatrix} \Delta x_1 \\ 0 \\ 0 \end{bmatrix} \quad (4.26)$$

where  $\mathbf{u}^1 = \begin{bmatrix} 0 & 0 & 0 \end{bmatrix}^T$  since displacement is constrained at the root due to the beam support.

The above finite difference scheme, given in Table 4.5, has been implemented using six MATLAB `.m` function files. The code used to calculate the beam displacements and twist from the computed nodal forces, moments and bimoments, was taken from code previously developed by the Applied Dynamics Group to analyse active closed cross section thin wall beams. In the beam input file, `beam_input.m`, given in Appendix C.1.1, the following input must be entered: the beam analysis code used; whether the induced actuation is off, on, or has its signs reversed at the beam midspan; the beam length; the boundary conditions; the applied loading; and the previously computed cross sectional stiffness and induced

actuation constants from Chapter 3. Next, the input processing file, `process_input.m`, given in Appendix C.1.2, transforms the stiffness constants  $C_{ij}$  to flexibility constants  $S_{ij}$ , assigns the induced actuation values at each node, and sets the initial guess values for the unknown forces, moments and bimoments at each node. The main analysis file, `beam_displacement_twist.m`, given in Appendix C.1.3, calls all the supporting functions and outputs the beam displacement and twist results. The system of beam equations and their corresponding Jacobian are constructed in the `equations.m` and `jacobian.m` files, given in Appendices C.1.4 and C.1.5. These equations are then solved in the Newton-Raphson solver file, `newton_raphson.m`, given in Appendix C.1.6. The beam displacements and twist recovery code is not included.

## 4.5 3-D Finite Element Analysis

Beam Examples 1 through 4 were omitted from this FE analysis since literature results were available. As there was a lack of experimental data available for active OCSTWBs, beam Examples 5 through 12, were analysed using 3-D FEA. The software used to perform the 3-D FE analysis was ANSYS Multiphysics. To begin a 3-D FEA analysis, the beam geometry should be entered. Each ply must have its own separate volume since material type, ply orientation and applied voltages are assigned directly to volumes. At a corner or intersection between two laminates, separate volumes must be defined which have height and width equal to the ply thicknesses. The 49 volumes that compose the lower laminate intersection of the I-beam are shown in Figure 4.6. This must be done to help ANSYS generate a valid structured mesh. Neighbouring volumes are bonded to each other by `Preprocessor > Modeling > Operate > Booleans > Glue > Volumes`.

An eight node elastic brick element with optional piezoelectric capabilities, called SOLID5, was selected by `Preprocessor > Element Type > Add/Edit/Delete > Add...`

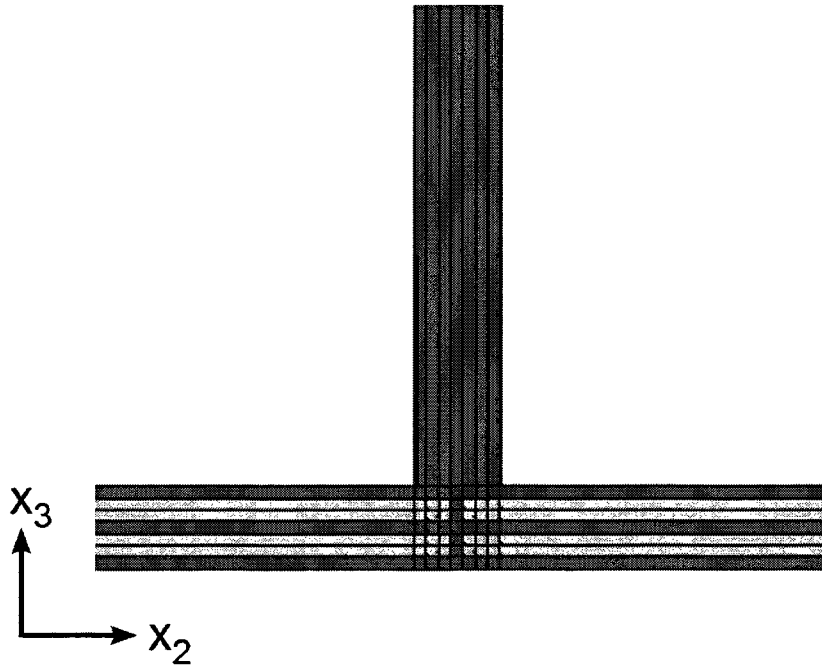


**Figure 4.6:** Front view of the lower laminate intersection of the 3-D FEA I-beam.

Two element types were created: one with displacement  $u_i$  degrees of freedom only for the carbon fibre plies, and one with an additional voltage  $V$  degree of freedom for the active plies.

Material properties are entered by `Preprocessor > Material Props > Material Models`. For the carbon fibre plies, a material model is created with an arbitrary density of unity and the elastic properties entered as a linear orthotropic material type. For the active plies, a material model is created with an arbitrary value of unity for material density; a relative permittivity ratio of 1800 for PZT fibres; the orthotropic material properties converted to an anisotropic elastic matrix, as required by ANSYS for active materials; and the piezoelectric electro-mechanical coupling terms  $d_{lij}$  entered as a piezoelectric strain matrix. For the piezoelectric strain matrix, the strain in the fibre direction due to an applied electric field in the fibre direction  $d_{111}$  is entered in row X column X; the strains perpendicular to the fibre direction due to an electric field in the fibre direction  $d_{122}$  are

entered in the YX and ZX row-column positions; and the remaining entries are set to zero.

Local coordinate systems must be created for each unique ply orientation by **WorkPlane > Local Coordinate Systems > Create Local CS > At Specified Loc +**, where the local  $x_{3-local}$  axis is oriented in the  $x_3$  direction for horizontal laminates and in the  $-x_2$  direction for vertical laminates, as shown in Figure 3.3. The  $x_{1-local}$  and  $x_{2-local}$  axes are oriented such that  $x_{1-local}$  is in the fibre direction, as shown in Figure 2.2. The element types, material models and local coordinate systems are assigned to each volume by **Preprocessor > Meshing > Mesh Attributes > Picked Volumes**.

A restrained boundary condition is applied by **Preprocessor > Loads > Define Loads > Apply > Structural > Displacement > On Areas**, selecting all the areas at the beam root, and prescribing zero displacement. A free to warp boundary condition can be approximately applied to a meshed I-beam model by restraining the nodes at the root end around the area centroid, such that rigid body motion of the beam is constrained.

A mechanical torque load at a beam tip is applied by first creating a single point node coincident with the beam reference line and positioned in front of the tip. Next, the node is connected to the tip by **Preprocessor > Modeling > Create > Contact Pair > Contact Wizard**, and selecting the areas that compose the beam tip as the Target Surface, the previously created node as the Target Type and a force-distributed constraint as the Constraint Surface Type. Finally, the torque is applied by **Preprocessor > Loads > Define Loads > Apply > Structural > Force/Moment > On Nodes** and entering the torque value. Using a contact pair, ANSYS will generate weighting functions that determine how the torque load will be distributed over the tip cross section.

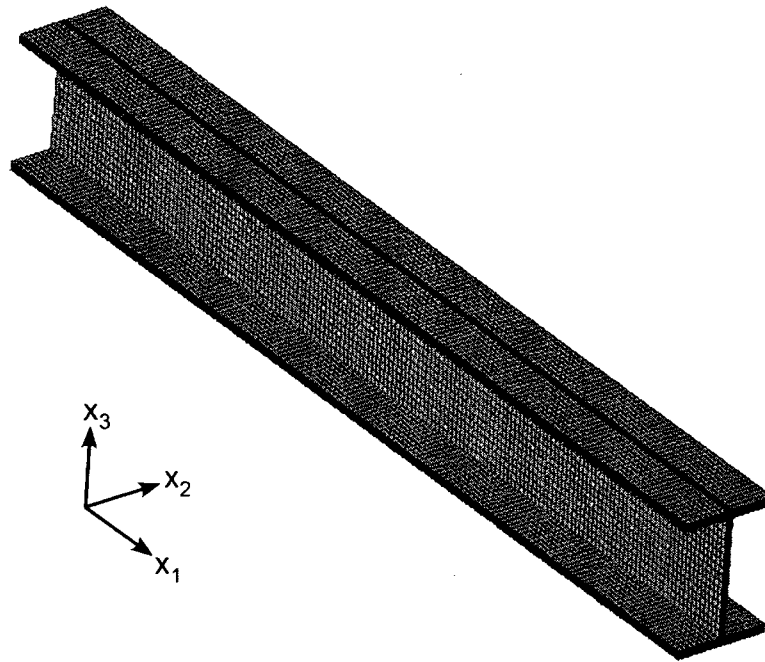
For a mechanical bimoment applied at the tip of an I-beam, Eq. 4.9 and Table 4.3 are used to determine the values of stress that must be applied to the flanges, as

$$\sigma_{x_1} = -\frac{M_{\omega}^t}{2hgb^2} \quad (4.27)$$

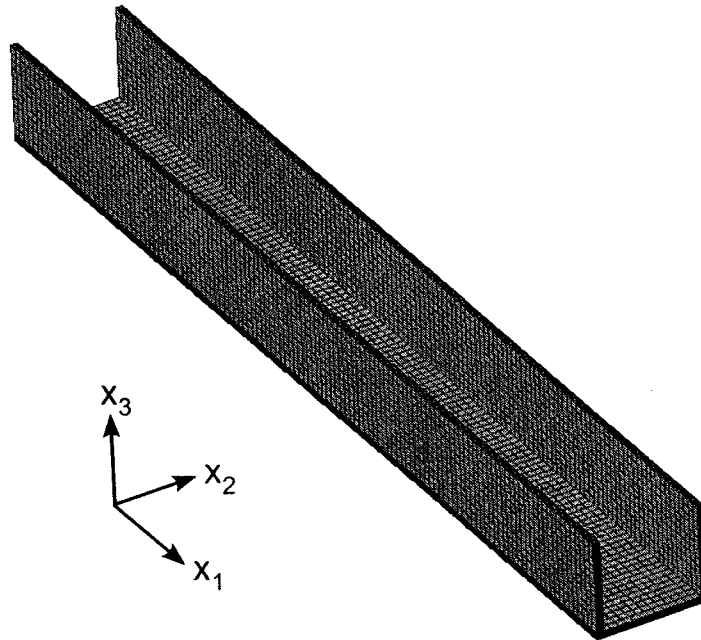
where the resulting stress value is  $\sigma_{x_1} = 17.14\text{E} + 6$  Pa. The sign of the stress on each flange is indicated in Table 4.3. In ANSYS, the stresses at the beam tip were applied by `Preprocessor > Loads > Define Loads > Apply > Structural > Pressure > On Areas`.

The value of the required electric field in the PZT fibre direction is given by Eq. 3.2. An electric field is applied to the active plies by first selecting `Preprocessor > Loads > Define Loads > Apply > Electric > Boundary > Voltage > On Areas`, and setting a voltage of zero to all the areas at the root end. Next, voltages are applied to the active ply areas on the tip end, producing an electric field in the axial beam direction. The values of the applied voltages are chosen such that the resulting components of the generated electric fields in the local PZT fibre directions are the required electric field values. The electric field components perpendicular to the PZT fibre directions will induce no strain, as required, since, by definition, the  $d_{1ij}$  electro-mechanical coupling terms only generate strain in the presence of an electric field in the fibre direction.

The beam model is meshed by first selecting `Preprocessor > Meshing > Mesh Tool > Size Controls > Global > Set`. It was checked that a maximum element edge length of 0.008 m was sufficient to obtain a converged solution. If the meshed elements were allowed to exceed 0.008 m in length, the resulting solution became poorly conditioned. The meshed I-beam and channel beam models are shown in Figures 4.7(a) and 4.7(b), respectively.



(a) I-beam.



(b) Channel.

**Figure 4.7:** Perspective view of the meshed 3-D FEA I-beam and channel beam models.

After running the simulation, the deformed beam shapes can be plotted by selecting **General Postproc > Plot Results > Deformed Shape**. Typical front views of the deformed I-beam and channel beam are shown in Figures 4.8(a) and 4.8(b), respectively, where the cross sectional warping can be more clearly discernable to the eye for the channel beam than for the I-beam.

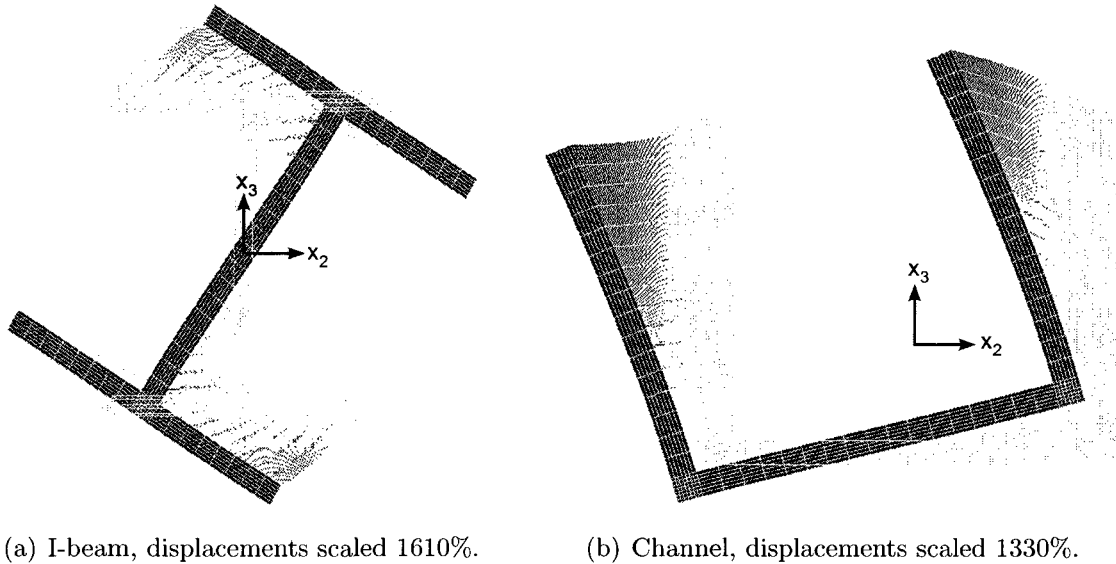


**Figure 4.8:** Front view of the deformed 3-D FEA I-beam and channel beam models.

To calculate the average beam displacements and twist, the coordinates  $x_i$  and displacements  $\hat{u}_i$  of every node are required. The nodal coordinates can be obtained by selecting **List > Nodes...** and the nodal displacements can be obtained by selecting **General Postproc > List Results > Nodal Solution > DOF Solution > Displacement vector sum**. Considering a typical beam cross section, as shown in Figure 4.9, the undeformed cross section undergoes a rigid body translation and rotation, described by the unknown displacement variables,  $u_2$  and  $u_3$ , and the unknown rotation variable  $\theta$ . These displacement and rotation variables describe the global deformation of a beam cross section and are the same as those described in Section 4.4. A rotation  $\theta$  of vector  $\mathbf{r}\mathbf{A}$  is given by

$$\begin{bmatrix} \cos \theta & -\sin \theta \\ \sin \theta & \cos \theta \end{bmatrix} \begin{bmatrix} x_2^i \\ x_3^i \end{bmatrix} = \begin{bmatrix} x_2^i \cos \theta - x_3^i \sin \theta \\ x_2^i \sin \theta + x_3^i \cos \theta \end{bmatrix} \quad (4.28)$$

where  $A$  can be any point on the cross section. After a rigid body translation and rotation, point  $A$  moves to point  $A''$ , and the displacement can be described by

$$\begin{bmatrix} u_2^{A''} \\ u_3^{A''} \end{bmatrix} = \begin{bmatrix} u_2 + x_2^i (\cos \theta - 1) - x_3^i \sin \theta \\ u_3 + x_3^i (\cos \theta - 1) + x_2^i \sin \theta \end{bmatrix} \quad (4.29)$$

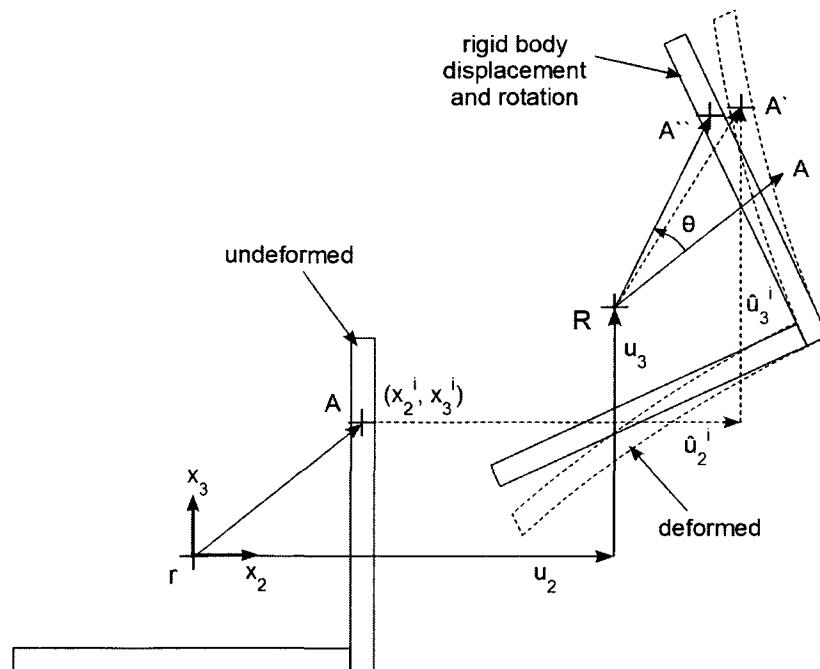


**Figure 4.9:** Undeformed, deformed, and rigid body minimized with respect to the deformed cross sections of an angle beam at a particular axial position  $x_1$ .

A minimization function can be constructed that measures the distance between a point on the cross section that has undergone rigid body deformation and one that has undergone full deformation, as predicted by ANSYS. The distances are added for all the nodes in the cross section, resulting in the function

$$\begin{aligned}
f(\theta, u_2, u_3) = \sum_{i=0}^N & [\hat{u}_2^i - u_2 - x_2^i (\cos \theta - 1) + x_3^i \sin \theta]^2 \\
& + [\hat{u}_3^i - u_3 - x_3^i (\cos \theta - 1) - x_2^i \sin \theta]^2
\end{aligned} \tag{4.30}$$

that when minimized, it describes how closely a particular rigid body deformation approximates the deformation predicted by ANSYS. In Eq. 4.30,  $N$  is the total number of nodes in a cross section and the square root sign has been omitted in order to cast the minimization function in a form that can be minimized using the `lsqnonlin` minimization function in MATLAB. The extensional displacement  $u_1$  can be obtained by averaging all of the axial displacements of the nodes in a cross section.

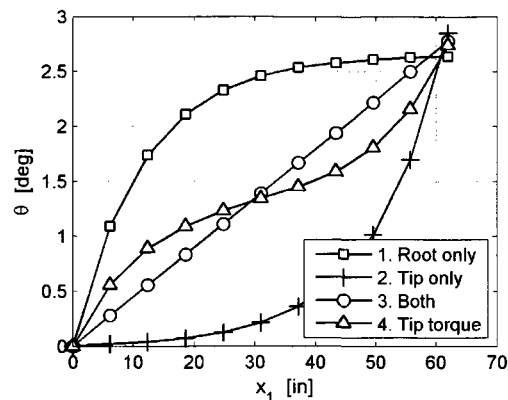
Three `.m` function files were developed in MATLAB to perform the minimization. The `read_ansys_results.m` file, given in Appendix C.2.1, uses a third party function called `txt2mat.m` to extract nodal results from the output text files produced by ANSYS and enter them into a matrix. The main analysis file, `beam_displ_rot.m`, given in Appendix C.2.2, finds the nodes that compose a particular cross section, calls the minimization function, and outputs the results. The minimization function file, `rigid_body_minimization.m`, given in Appendix C.2.3, implements Eq. 4.30.

## 4.6 Results and Discussion

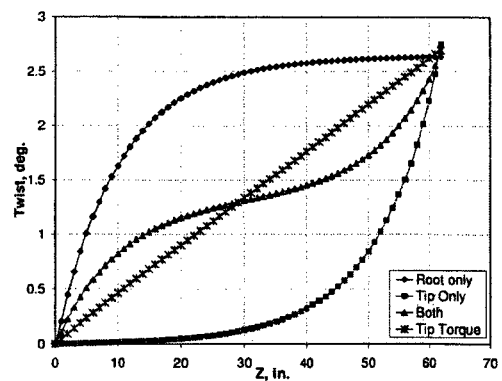
The displacements and twists predicted for the beam examples by the cross sectional analysis codes, UM/VABS and the active OCSTWB code, using the nonlinear 1-D beam formulation were obtained. Due to the absence of any corresponding experimental data in the literature, these results were compared to the corresponding results from a 3-D FEA

solution in each case. Only the significant displacement and twist profiles are presented below, where the insignificant ones have been omitted. It should be noted that in all the following examples, the beam is restrained from twist and displacement at the root and the tip is always free to twist and displace.

The twist profiles of the isotropic I-beams, Examples 1 through 4, analysed by the active OCSTWB code, are shown in Figure 4.10(a). The corresponding results given in the literature [1], are shown in Figure 4.10(b). The agreement of the results with the literature is excellent.



(a) Active OCSTWB code.



(b) Literature, courtesy of [1].

**Figure 4.10:** Examples 1 through 4. Twist profiles predicted for the isotropic I-beams, for a free to warp root and free tip, with mechanical bimoments applied to the root only (1), the tip only (2), and to both the tip and the root (3); and a mechanical torque applied to the tip (4).

Figures 4.11(a) and 4.11(b) show the twist  $\theta$  profiles of the active strip and cruciform, Examples 5 and 6, respectively, predicted by 3-D FEA, UM/VABS and the active OCSTWB code. For both examples, the root is restrained, the tip is free, and 2000 V is applied. Both 3-D FEA and UM/VABS are in close agreement; however, the active OCSTWB code predicts zero twist. These special beam examples demonstrate a limitation of the active OCSTWB code where it cannot capture active torsional couples induced

by active layers within the thickness of a single composite lay-up due to the thin wall assumption. However, it is capable of capturing the induced moments within a built-up cross section of active laminates, as would be used in practical applications. As the cruciform, Example 6, is simply the strip, Example 5 with a symmetric lay-up and passive vertical stiffeners added, the reversed twist direction and reduced twist magnitude of the cruciform compared to the strip, are as expected.

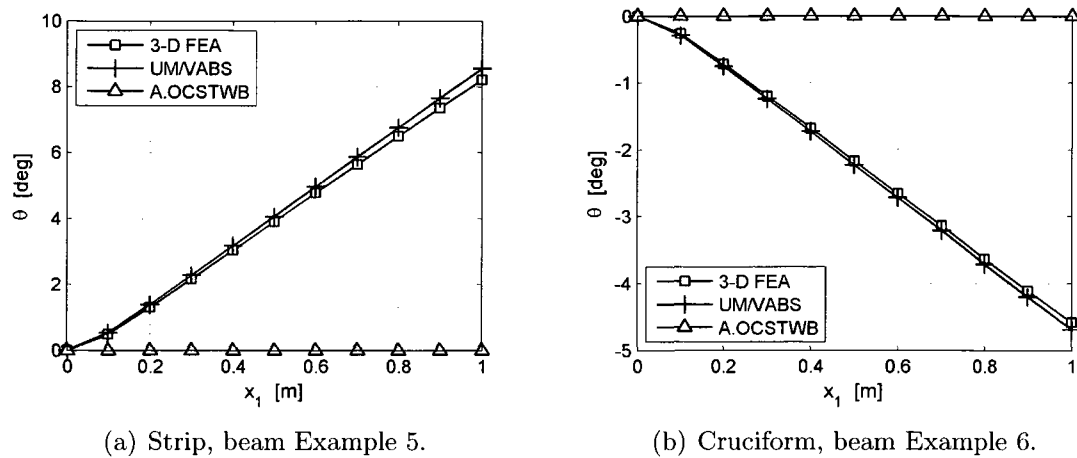


**Figure 4.11:** Examples 5 and 6. Twist profiles of the active strip and cruciform, for a restrained root and free tip, with 2000 V applied.

The axial displacement  $u_1$  profile of the active extensional I-beam, Example 7, predicted by 3-D FEA, UM/VABS and the active OCSTWB code, is shown in Figure 4.12. Again, the root is restrained, the tip is free, and 2000 V is applied. The excellent agreement of the results with the 3-D FEA is clearly shown in this diagram.

The twist  $\theta$  profiles of the active and passive I-beams with restrained warping at the root and free warping at the tip, Examples 8 and 9, as predicted by 3-D FEA, UM/VABS and the active OCSTWB code, are shown in Figures 4.13(a) and 4.13(b), respectively, and indicate close agreement between all three codes. In the case of the passive I-beam, a mechanical bimoment of  $M_\omega^t = -30 \text{ N}\cdot\text{m}^2$  was applied at the tip. This mechanical bimoment is approximately equal to the values of the induced bimoment that were predicted

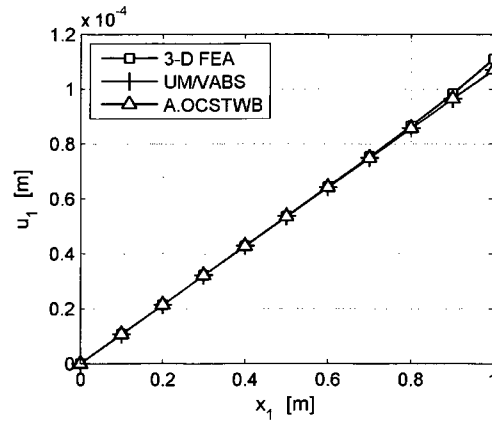


**Figure 4.12:** Example 7. Axial extension of the active I-beam, for a restrained root and free tip, with 2000 V applied.

by UM/VABS and the active OCSTWB code of  $M_{\omega}^t = -31.1 \text{ N}\cdot\text{m}^2$  and  $M_{\omega}^t = -31.6 \text{ N}\cdot\text{m}^2$ , respectively. Both the active and passive twist profiles closely match, indicating that an active I-beam with an induced bimoment, and warping restrained root and free tip boundary conditions can alternatively be analysed as a passive beam with an equal valued mechanical bimoment applied at the tip. For the active I-beam, the maximum twist of  $-2.43^\circ$  at the beam tip shows that appreciable twist can be achieved by inducing an active bimoment in an I-beam with restrained warping at the root.

The twist  $\theta$  profiles of the active and passive I-beams with free to warp boundary conditions at the root and the tip, Examples 10 and 11, predicted by 3-D FEA, UM/VABS and the active OCSTWB code, are shown in Figures 4.14(a) and 4.14(b), respectively. For both plots, the UM/VABS and active OCSTWB code results are in close agreement; however, the 3-D FEA results predict somewhat greater twist than the other two codes. In the active case, the 3-D FEA results predicted slightly greater than zero twist at the root ends due to the difficulty in modelling a true zero twist boundary condition at a free to warp beam end of a 3-D FEA model. As a result, while the centre of the I-beam web at the root is constrained to have a zero twist, the remainder of the I-beam cross section

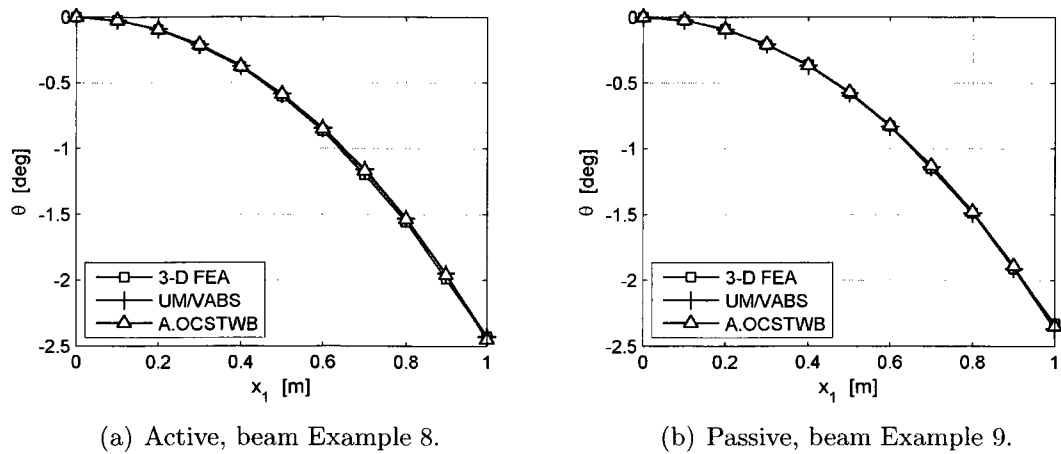


**Figure 4.13:** Examples 8 and 9, I-beams restrained from warping at the root and free to warp at the tip. Twist profiles of (a) active beam subjected to  $\pm 2000$  V and (b) passive beam with  $M_{\omega}^t = -30$  N·m<sup>2</sup> applied mechanical tip bimoment.

at the root can warp such that the net rigid body rotation of the entire cross section at the root end is no longer zero. In the passive case, the twist predicted by 3-D FEA is 13.2% larger than that predicted by UM/VABS and the active OCSTWB code. This could be due to two reasons. A lower level of accuracy in the finite difference scheme that was used to recover global displacements and twist, and the greater beam flexibility due to more degrees of freedom in a 3-D FEA analysis than in a 2-D cross sectional analysis.

Unlike in the case of a warping restrained root and free to warp tip boundary condition, for the free to warp root and free to warp tip boundary condition, the twist profiles predicted for a passive and active I-beam with equal valued induced and mechanical bimoments are very different. Consequently, there are particular boundary conditions in which an active beam cannot be analysed as a passive beam with a corresponding mechanical end load. By changing the root boundary condition of the passive I-beam from warping restrained, in Example 9, to free to warp, in Example 11, the amount of twist produced is about four times greater, as shown in Figures 4.13(b) and 4.14(b). A greater amount

of twist is expected with a free to warp root since a warping restrained root reduces the Vlasov warping, which is a mode for beam twist.

For the active I-beam with a free to warp root, Example 10, the twist profile is symmetrical with approximately zero twist predicted at the beam ends and a maximum twist of  $0.71^\circ$  predicted at the beam midspan, as shown in Figure 4.14(a). At the tip, the twist predicted by UM/VABS and the active OCSTWB code is not exactly zero. This is likely due to the displacement and twist recovery code accumulating numerical error as it cumulatively adds changes in displacement and twist node-to-node from the prescribed zero initial displacement and twist at the root node.

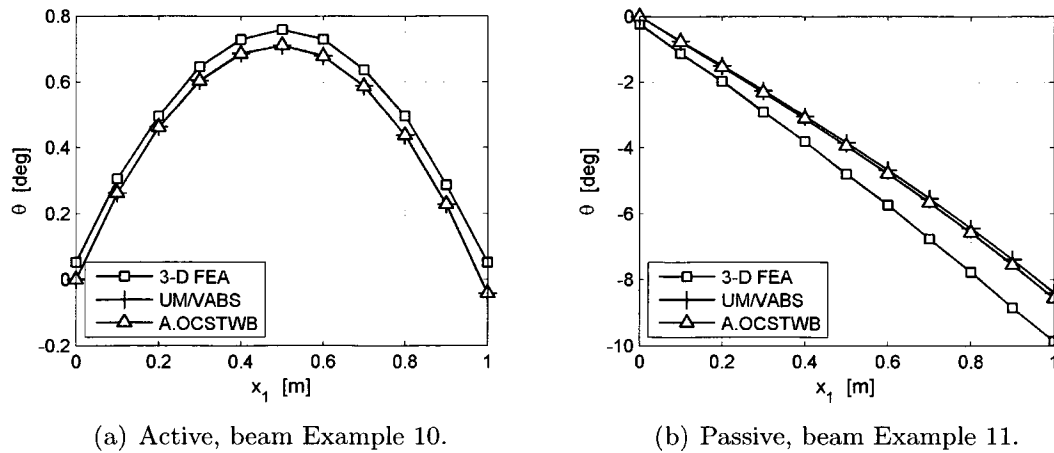


**Figure 4.14:** Examples 10 and 11, I-beams free to warp at the root and tip. Twist profiles of (a) active beam subjected to  $\pm 2000$  V and (b) passive beam, with  $M_\omega^t = -30 \text{ N}\cdot\text{m}^2$  applied mechanical tip bimoment.

In an attempt to generate appreciable twist in an active I-beam with a free to warp root boundary condition, the sign of the voltage of Example 10 was reversed at the beam midspan. The resulting twist profile for Example 12 is shown in Figure 4.15, where, as in the case of Example 10, shown in Figure 4.14(a), no appreciable twist is produced in the beam. As before, zero twist is predicted at the beam ends; however, the twist profile

now has a sinusoidal shape, with zero twist predicted at the beam midspan. Also, both the UM/VABS and the active OCSTWB code results are in close agreement, while the twist predicted by 3-D FEA is somewhat different. This difference again can be attributed to the modelling of the zero twist root boundary condition in a 3-D FEA model and the limited accuracy of the finite difference scheme used to recover the beam displacements and twist.

Beam Examples 10 and 12 have only internal normal axial forces due to the actuation of the active plies, whereas Examples 8, 9 and 12 all have external normal axial forces due to either the presence of a warping restrained end or the direct application of normal axial mechanical forces. Consequently, Figures 4.13, 4.14 and 4.15 indicate that external normal axial forces are required to generate appreciable twist in an I-beam through Vlasov deformation.

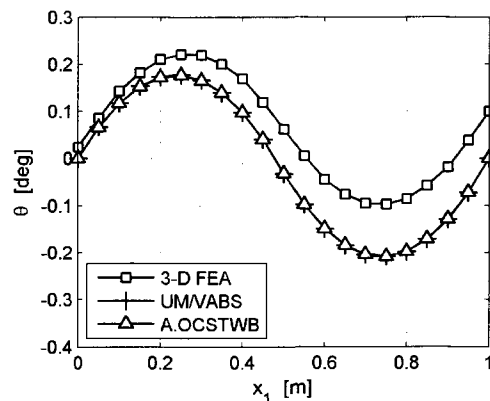


**Figure 4.15:** Example 12, I-beam with free to warp at the root and the tip. Twist profile of the active beam subjected to  $\pm 2000$  V, with the sign of the applied voltages reversed at the midspan.

In a second attempt to generate appreciable twist in an active I-beam with a free to warp root boundary condition, the tip boundary condition of beam Example 10 was changed to warping restrained. The resulting twist profile for beam Example 13 is shown

in Figure 4.16, where an appreciable twist of  $2.41^\circ$  was predicted at the beam tip. The twist profile of beam Example 13 has both an inverted sign and shape from the twist profile of beam Example 8, as expected, since the warping restrained boundary condition has been moved to the beam tip and a free to warp root boundary condition effectively acts as a free end in the case of induced actuation.

As seen in Figures 4.13(a) and 4.16, greater overall twist is achieved in the outer half of the beam span of Example 13 compared to Example 8. Of the previous active I-beam examples analysed, Example 13 is the most appropriate one to use as an I-beam spar for a helicopter rotor blade since the outboard half of a rotor blade generates the most lift due to its higher velocity relative to the inboard half. In the following chapter, an active I-beam spar will be optimized for maximum produced twist.

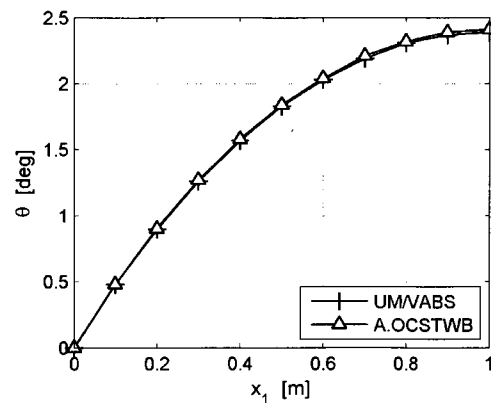


**Figure 4.16:** Example 13. Twist profile of the active I-beam with a free to warp root and a warping restrained tip, subjected to  $\pm 2000$  V.

# Chapter 5

## Parametric Investigation of an Active I-beam

In this chapter, a parametric investigation of an active I-beam spar for maximum twist in a helicopter rotor blade will be investigated using the active OCSTWB code, previously verified in Chapters 3 and 4. The optimal placement of passive and active plies in an I-beam spar to achieve maximum twist using an induced bimoment will be determined. High performance MFCs will be used rather than older AFCs in order to give an improved estimate of the actuation authority one can expect when using piezoelectric fibre composites in a rotor blade.

### 5.1 I-beam Spar Configurations

Beginning with the integral twist-actuated rotor blades presented in [62, 37], the dimensions and laminates given for the  $(\frac{1}{6})^{\text{th}}$  Mach-scaled Boeing CH-47D helicopter rotor blade, modified to include AFCs, were used as a baseline to obtain a beam length, chord length, airfoil shape, and a mass per unit length value for the spar. Next, the active D-spar was

replaced by an active I-beam spar with the same wall thickness, as shown in Figure 5.1. The rotor blade skin and internal foam are only needed to maintain the airfoil shape and their contribution to the beam stiffness will be neglected in the current analysis. The height-to-width ratio of the I-beam spar in [1], optimized for maximum twist using a mechanical bimoment, was chosen as a reasonable starting ratio for an active I-beam spar to be optimized for maximum twist using an induced bimoment, as shown in Figure 5.2.

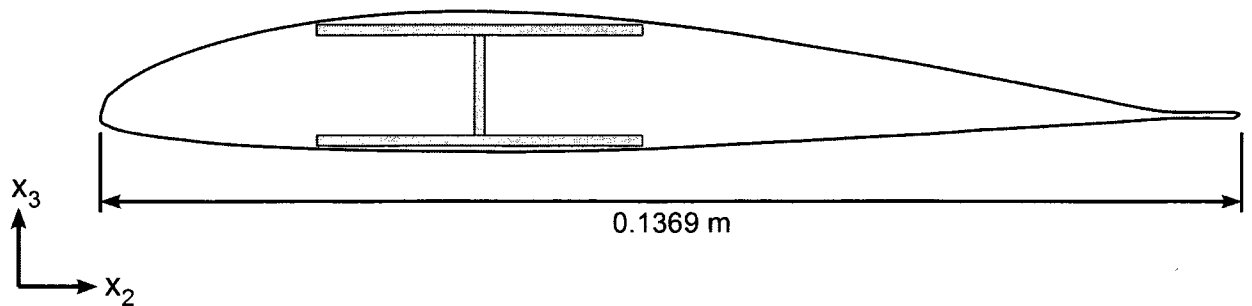


**Figure 5.1:** Cross sectional view of an I-beam spar embedded in a VR-7 airfoil of a  $(\frac{1}{6})^{\text{th}}$  scaled Boeing CH-47D helicopter rotor blade.

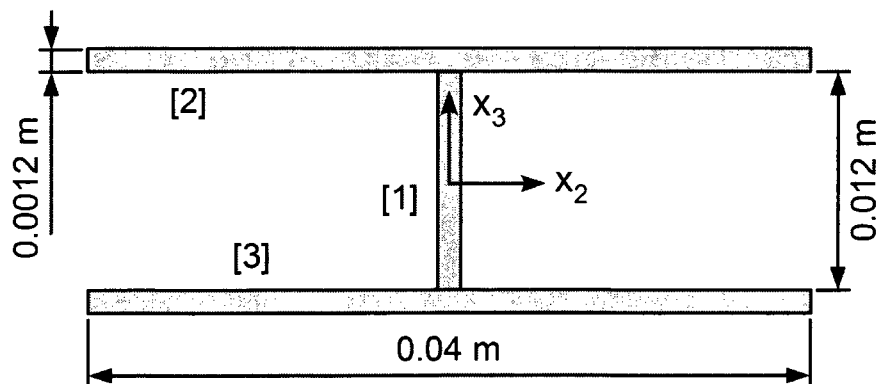


**Figure 5.2:** Cross sectional dimensions of the active I-beam spar.

As given in [52], the thickness of an AS4/3506-1 carbon fibre ply is  $1.27\text{E-}4$  m; however, it will be approximated as  $1.5\text{E-}4$  m to facilitate the cross sectional modelling. Both the AS4/3506-1 and MFC material properties are given in Table 5.1, where the MFC material

properties were obtained from [9].

**Table 5.1:** Passive and active ply material properties.

	AS4/3506-1	MFC
$E_{11}$ [GPa]	141.96	30.34
$E_{22}$ [GPa]	9.79	15.86
$G_{12}$ [GPa]	6	5.52
$G_{23}$ [GPa]	4.8	5.52
$\nu_{12}$	0.3	0.31
$\nu_{23}$	0.4	0.31
$t_{ply}$ [m]	3.0E-4	1.5E-4
$d_{111}$ [m/V]		4.60E-10
$d_{112}$ [m/V]		0
$d_{122}$ [m/V]		-2.10E-10
$t_{electrodes}$ [m]		5.0E-4

Each flange is divided into four equal width laminates, the outer ( $O_f$ ) widths and inner ( $I_f$ ) widths, as shown in Figure 5.3. The corresponding laminate ply lay-ups are given in Tables 5.2, 5.3 and 5.4, where S denotes AS4/3506-1, M denotes MFC, and  $M^P$  denotes a passive MFC ply such that no voltage is applied. The laminate ply lay-ups are given from bottom to top. Both top [2] and bottom [3] flanges have the same laminate ply lay-ups. All the configurations have a web laminate ply lay-up of  $[(90S)_2/(0S)_4/(90S)_2]$ . The voltages applied to the left (L) and right (R) halves of each flange are: +1500 V, -500 V, -500 V and +1500 V, for the [2-L], [2-R], [3-L] and [3-R] flange halves, respectively. These are the maximum voltage values given in the MFC specifications [9]. The magnitude of the negative applied voltages, which cause the MFCs to contract in the fibre direction, is less than the magnitude of the positive applied voltages since PZT fibres can contract much less than they can extend. For Configurations 7 and 8, in Table 5.4, the I-beam spar is divided into two equal length spans, an inner ( $I_s$ ) span and an outer ( $O_s$ ) span, as shown in Figure 5.4.

Three different laminate ply lay-up variables of the I-beam spar were optimized. First, beam Configurations 1 through 3, given in Table 5.2, were used to determine the optimal

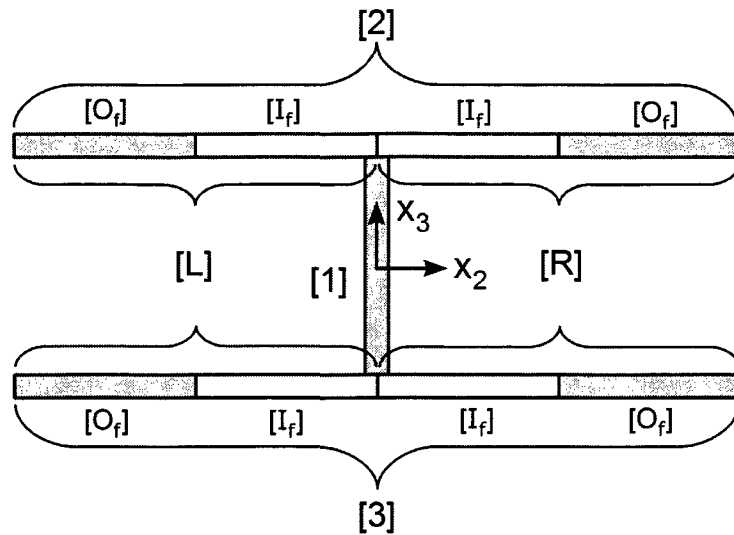


**Figure 5.3:** Inner ( $I_f$ ) and outer ( $O_f$ ) laminate segments of the left (L) and right (R) I-beam flanges.

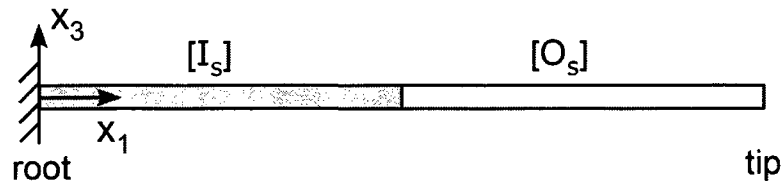


**Figure 5.4:** Inner ( $I_s$ ) and outer ( $O_s$ ) I-beam spar spans.

flange-wise placement of the carbon fibre plies. Under constant induced bimoment, the carbon fibre plies are initially uniform across the flanges, then distributed in the inner widths of the flanges, and finally distributed in the outer widths of the flanges. The total amount of carbon fibre plies is constant in all three beam configurations. Second, beam Configurations 4 through 6, given in Table 5.3, were used to determine the optimal flange-wise placement of the MFCs. Under constant stiffness, the active MFC plies are initially uniform across the flanges, then alternately distributed in the inner and outer widths of the flanges. Third, beam Configurations 4, 7 and 8, given in Table 5.4, were used to determine the optimal span-wise placement of the MFCs. Under constant stiffness, the active MFC plies are initially uniform across both the flange and span, then alternately distributed in the inner and outer spans of the beam. In all beam configurations, the beam length is 1

m and the boundary conditions are warping restrained at the root and free to warp at the tip. For Configurations 4 through 8, the mass per unit length of the beam, 0.3454 kg/m, is a little less than the for the D-spar of reference [62], 0.3621 kg/m. Consequently, these I-beam spar configurations are comparable to the original D-spar.

**Table 5.2:** Active I-beam spar configurations for the flange-wise distribution of carbon plies under constant induced bimoment.

Distribution	Segment	
	$[I_f]$	$[O_f]$
1. Uniform	$[0M/(0S)_2/0M^P/0M]$	same
2. In	$[0M/(0S)_4/0M]$	$[0M/(0M^P)_2/0M]$
3. Out	$[0M/(0M^P)_2/0M]$	$[0M/(0S)_4/0M]$

**Table 5.3:** Active I-beam spar configurations for the flange-wise distribution of MFC plies under constant stiffness.

Distribution	Segment	
	$[I_f]$	$[O_f]$
4. Uniform	$[(0S)_2/0M/0M^P/(0S)_2]$	same
5. In	$[(0S)_2/(0M)_2/(0S)_2]$	$[(0S)_2/(0M^P)_2/(0S)_2]$
6. Out	$[(0S)_2/(0M^P)_2/(0S)_2]$	$[(0S)_2/(0M)_2/(0S)_2]$

**Table 5.4:** Active I-beam spar configurations for the span-wise distribution of MFC plies under constant stiffness.

Distribution	Segment	
	$[I_s]$	$[O_s]$
4. Uniform	$[(0S)_2/0M/0M^P/(0S)_2]$	same
7. In	$[(0S)_2/(0M)_2/(0S)_2]$	$[(0S)_2/(0M^P)_2/(0S)_2]$
8. Out	$[(0S)_2/(0M^P)_2/(0S)_2]$	$[(0S)_2/(0M)_2/(0S)_2]$

## 5.2 Results and Discussion

The twist profiles of the active I-beam spar with various flange-wise distributions of carbon fibre plies, Configurations 1 through 3, are shown in Figure 5.5. The distribution of  $0^\circ$  carbon fibre plies near the web compared to near the flange edges has little effect on the twist produced in the I-beam spar.

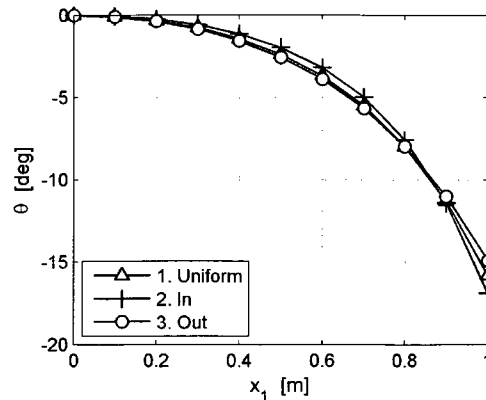
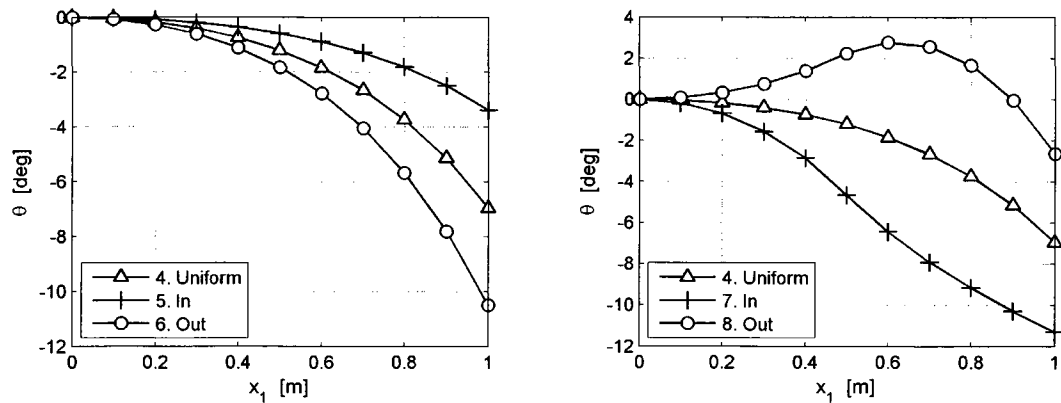


**Figure 5.5:** Flange-wise carbon fibre ply distribution, I-beam spar Configurations 1 through 3. Twist profiles of the active I-beam spar, for a warping restrained root and a free to warp tip, with the distribution of carbon fibre plies varying in the flange-wise direction.

The twist profiles of the active I-beam spar with various flange-wise MFC ply distributions, Configurations 4 through 6, are shown in Figure 5.6(a). An MFC ply in the outer flange width contributes approximately 210% more to twist actuation than an MFC ply in the inner flange width. The twist profiles of the active I-beam spar with various span-wise MFC ply distributions, Configurations 4, 7 and 8, are shown in Figure 5.6(b). An MFC ply in the inner I-beam spar span, which is the span closest to the warping restrained root boundary condition, contributes approximately 330% more to twist actuation than an MFC ply in the outer I-beam spar span. Consequently, to maximize twist in an I-beam spar by inducing a bimoment, the active plies must be distributed towards the outer flange edges and close to the warping restrained boundary condition at the root.



(a) Flange-wise distribution, Configurations 4 through 6. (b) Span-wise distribution, Configurations 4, 7 and 8.

**Figure 5.6:** Twist profiles of the active I-beam spar, for a warping restrained root and a free to warp tip, with the distribution of MFC plies varying in the (a) flange-wise and (b) span-wise directions.

Between Configurations 4 through 8, which satisfy the mass per unit length restrictions of the  $(\frac{1}{6})^{\text{th}}$  scaled CH-47D rotor blade, Configurations 6 and 7 produce the highest tip twist values of  $\pm 10.5^\circ$  and  $\pm 11.3^\circ$ , respectively. Using the I-beam spar Configuration 6, an alternate set of boundary conditions and applied voltage were found to produce a slightly greater tip twist. Restraining the warping at both the root and the tip of Configuration 6, and reversing the sign of the applied voltages at the midspan, results in the twist profile shown in Figure 5.7. This new set of boundary conditions and applied voltages result in greater overall twist for the outer span of the rotor blade, where most of the lift is produced [1].

A full analysis of the rotor blade, including the skin, foam and I-beam spar, is required to obtain a more accurate twist profile for the  $(\frac{1}{6})^{\text{th}}$  scaled CH-47D rotor blade. If a span-wise segmented airfoil structure is used, such that the airfoil skin and foam are cut in the chord-wise direction at a number of beam stations, as shown in Figure 5.8, the I-beam spar would become the dominant structural member that provides torsional stiffening. In this case, the twist values predicted for the active I-beam spar would be close to the twist

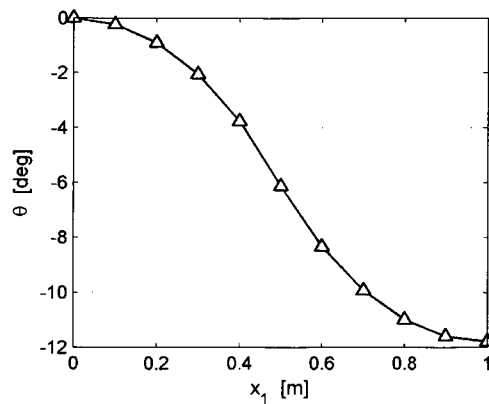


**Figure 5.7:** Configuration 6, alternate boundary conditions. Twist profile of the optimized active I-beam spar, for a warping restrained root and a warping restrained tip, with the signs of the applied voltages reversed at the midspan.

produced by the overall rotor blade structure. The segmented airfoil model was proposed and investigated in [8], where it was experimentally shown that the chord-wise cuts have little effect on the aerodynamic properties of the rotor blade.

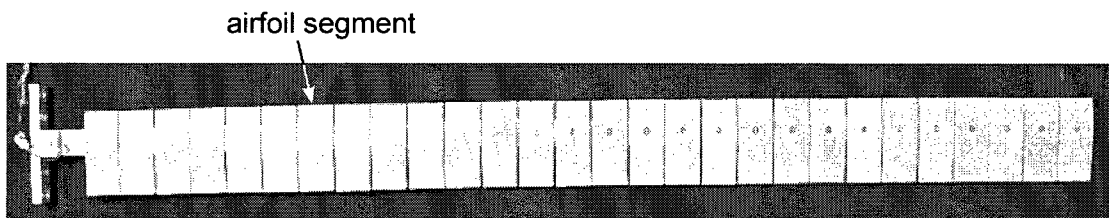


**Figure 5.8:** Segmented airfoil concept, courtesy of [8].

As discussed in [45], a new type of MFC, called a “single crystal MFC,” is currently in development. When used in the Active Twist Rotor (ATR) model [12], the single crystal MFC implementation produced approximately 300% more twist than a standard MFC implementation and 900% more twist than when using AFCs [45]. Consequently, MFCs can be used to produce appreciable twist in an I-beam spar; and a new type of MFC, not yet being manufactured, offers the possibility of producing much larger amounts of twist in an I-beam spar.

# Chapter 6

## Conclusions and Recommendations

### 6.1 Conclusions

The thesis work began by a literature review of beam theories, the Variational Asymptotic Method (VAM), and composite and active materials. The application of the VAM to analyse active OCSTWB was reviewed. The validity of the resulting active OCSTWB analysis code was investigated by analysing the cross sectional properties of a number of different open active sections using OCSTWB and comparing the results to those (a) existing in the literature and (b) resulting from other available methods. This code proved to be an extremely accurate, reliable and fast method. Using these cross sectional properties, the nonlinear behaviour of a number of open passive and active, thin wall cross sections subjected to mechanically applied and induced bimoments were investigated. To this end, the nonlinear span-wise problem along the beam reference line was solved by discretizing the governing equilibrium equations using a forward finite difference scheme. The modelling of active OCSTWB in 3-D FEA was investigated, and the global displacements and twist values were calculated by minimizing the deformation of a rigid body cross section with the 3-D FEA nodal displacements. Both 3-D FEA and literature results were used

to verify the active OCSTWB code. An active I-beam spar was used in a parametric optimization study to determine the distributions of carbon fibre and MFC plies that produce the greatest twist using an induced bimoment effect. The following conclusions are noteworthy:

- A code based on the VAM that can analytically analyse active prismatic OCSTWB has been verified against literature results, 3-D FEA, and the 2-D FE cross sectional analysis tools, GT/VABS and UM/VABS.
- Appreciable twist can be produced in an OCSTWB using piezoelectric fibre composites. Using MFCs to induce a bimoment in an I-beam can be a particularly effective method of producing twist.
- In an implementation of an optimized active I-beam spar in a  $(\frac{1}{6})^{\text{th}}$  Mach-scaled Boeing CH-47D helicopter rotor blade using MFCs, it was found that twist could be maximized, when using the induced bimoment effect, by distributing the MFCs towards the outer flange edges and towards the restrained warping beam root.

## 6.2 Recommendations

There is much work that can be done in further development of the active OCSTWB theory. Some of the possible future work could involve:

- Extend the active OCSTWB theory to include beams that have initial twist and curvature since many helicopter rotor blades are designed with initial twist.
- Augment the active OCSTWB theory to construct a Timoshenko-like beam model, in order to analyse beams with short lengths, beams undergoing high frequency vibration, or to accurately find the shear centre of a beam.

- Derive the intrinsic dynamic equilibrium equations for a Vlasov-like beam model, in order to perform vibration and dynamic analyses.
- Solve the nonlinear problem along the beam span using the FE method, in order to obtain a more accurate solution that converges with fewer elements, and thus faster, compared to using the finite difference method.
- Develop the local recovery relations, in order to find the displacements, stresses and strains at a particular local material point in the beam.
- Use a broad optimization design space of an active OCSTWB spar and perform simulation runs using the active OCSTWB code in a genetic or swarm optimization scheme.

# Bibliography

- [1] Mihir Mistry, Farhan Gandhi, and Ramesh Chandra. Twist Control of an I-beam through Vlasov Bimoment Actuation. In *Collection of Papers - 49<sup>th</sup> AIAA/ASME/ASCE/AHS/ASC Structures, Structural Dynamics and Materials Conference*, Schaumburg, IL, 7-10 April 2008. AIAA.
- [2] A. D. Wright, L. J. Fingersh, and K. A. Stol. Testing controls to mitigate fatigue loads in the controls advanced research turbine. In *2009 17<sup>th</sup> Mediterranean Conference on Control and Automation (MED)*, Thessaloniki, Greece, 24-26 June 2009. IEEE.
- [3] M. Asano, Y. Yamano, K. Yoshie, Y. Koike, K. Nakagawa, and T. Murata. Development of active-damping bridges and its application to triple high-rise buildings. *JSME International Journal, Series C (Mechanical Systems, Machine Elements and Manufacturing)*, 46(3):854–60, 2003.
- [4] J. Rocha, P.A. Moniz, A. P. Costa, and A. Suleman. On active aeroelastic control of an adaptive wing using piezoelectric actuators. *Journal of Aircraft*, 42(1):278–282, 2005.
- [5] Andrew Rader. Optimization of Piezoelectric Actuator Configuration on a Flexible Fin for Vibration Control Using Genetic Algorithms. Master’s thesis, Carleton University, 2005.

- [6] Carlos E. S. Cesnik, SangJoon Shin, and Matthew L. Wilbur. Dynamic response of active twist rotor blades. *Smart Materials and Structures*, 10(1):62–76, 2001.
- [7] Serkan Ozbay, Olivier Bauchau, D. Stefan Dancila, and Erian A. Armanios. Extension-Twist Coupling Optimization in Composite Rotor Blades. In *Collection of Technical Papers - AIAA/ASME/ASCE/AHS/ASC Structures, Structural Dynamics and Materials Conference*, Austin, TX, APRIL 2005. American Institute of Aeronautics and Astronautics Inc.
- [8] F. Khouli. *Modelling and Attenuation Feasibility of the Aeroelastic Response of Active Helicopter Rotor Systems During the Engagement/Disengagement Phase of Maritime Operation*. PhD thesis, Carleton University, 2009.
- [9] Smart Material Corporation. *MFC Technical Data*. <http://www.smart-material.com/media/Publications/MFCata.pdf>.
- [10] S. L. Lemanski, P. M. Weaver, and G. F. J. Hill. Design of composite helicopter rotor blades to meet given cross-sectional properties. *The Aeronautical Journal*, 109(1100):471–475, 2005.
- [11] Vitaliv Volovoi, Sangpil Yoon, Chang-Young Lee, and Dewey Hodges. Structural optimization of composite rotor blades. In *Collection of Papers - 45<sup>th</sup> AIAA/ASME/ASCE/AHS/ASC Structures, Structural Dynamics and Materials Conference*, Palm Springs, CA, 19-22 April 2004. AIAA.
- [12] Carlos E. S. Cesnik, Jiwon Mok, Anish S. Parikh, and SangJoon Shin. Optimization Design Framework of Integrally Twisted Helicopter Blades. In *Collection of Papers - 45<sup>th</sup> AIAA/ASME/ASCE/AHS/ASC Structures, Structural Dynamics and Materials Conference*, Palm Springs, CA, 19-22 April 2004. AIAA.

- [13] Jae-Sang<sup>1</sup> Park and Ji-Hwan Kim. Design and aeroelastic analysis of active twist rotor blades incorporating single crystal macro fiber composite actuators. *Composites Part B: Engineering*, 39(6):1011–1025, 2008.
- [14] Justin M. Lloyd, R. Brett Williams, Daniel J. Inman, and W. Keats Wilkie. An analytical model of the mechanical properties of the single crystal macro-fiber composite actuator. In *Proceedings of SPIE - The International Society for Optical Engineering*, San Diego, CA, March 2004. SPIE.
- [15] F. Khouli, F. F. Afagh, and R. G. Langlois. Actuation of slender thin-wall anisotropic open cross-section beams base on asymptotically-correct Vlasov theory. In *Proceedings of the 17<sup>th</sup> International Conference on Adaptive Structures and Technologies*, Taipei, Taiwan, 16-19 October 2006. ASME/AIAA/IEEE.
- [16] Carlos E. S. Cesnik and Dewey H. Hodges. VABS: A New Concept for Composite Rotor Blade Cross-Sectional Modeling. In *American Helicopter Society 51<sup>st</sup> Annual Forum*, Fort Worth, TX, 9-11 May 1995. American Helicopter Society Inc.
- [17] Wenbin Yu, Vitali V. Volovoi, Dewey H. Hodges, and Xianyu Hong. Validation of the Variational Asymptotic Beam Sectional Analysis (vabs). In *Collection of Technical Papers - 42<sup>nd</sup> AIAA/ASME/ASCE/AHS/ASC Structures, Structural Dynamics, and Materials Conference*, Seattle, WA, 16-19 April 2001. AIAA.
- [18] F. Khouli, J. Griffiths, F. F. Afagh, and R. G. Langlois. Actuation of slender thin-wall anisotropic open cross-section beams based on asymptotically-correct Vlasov. *Submitted to the Journal of Intelligent Material Systems and Structures*, 2009.
- [19] Dewey H. Hodges. *Nonlinear Composite Beam Theory*, volume 213 of *Progress in Aeronautics and Astronautics*. AIAA, 2006.

- [20] Wenbin Yu and Dewey H. Hodges. The Timoshenko-like Theory of the Variational Asymptotic Beam Sectional Analysis. In *Collection of Technical Papers - 44<sup>th</sup> AIAA/ASME/ASCE/AHS/ASC Structures, Structural Dynamics, and Materials Conference*, Norfolk, VA, 7-10 April 2003. AIAA.
- [21] J. R. Barber. *Elasticity*. Kluwer Academic Publishers, second edition edition, 2002.
- [22] J. N. Reddy, C. M. Wang, and K. H. Lee. Relationships Between Bending Solutions of Classical and Shear Deformation Beam Theories. *International Journal of Solids and Structures*, 2(5-7):3373–3384, 1997.
- [23] Wenbin Yu, Dewey H. Hodges, Vitali V. Volovoi, and Eduardo D. Fuchs. A generalized Vlasov theory for composite beams. *Thin-Walled Structures*, 43(9):1493–1511, 2005.
- [24] Carlos E.S. Cesnik and Rafael Palacios. Modeling piezocomposite actuators embedded in slender structures. In *Collection of Technical Papers - 44<sup>th</sup> AIAA/ASME/ASCE/AHS/ASC Structures, Structural Dynamics and Materials Conference*, Norfolk, VA, 7-10 April 2003. AIAA.
- [25] V. V. Volovoi, D. H. Hodges, C. E. S. Cesnik, and B. Popescu. Assessment of Beam Modeling Methods for Rotor Blade Applications. In *Proceedings of the 1999 55<sup>th</sup> Annual Forum of the American Helicopter Society*, Montreal, CA, 25-27 May 1999. American Helicopter Society.
- [26] Walter D. Pilkey. *Nonlinear Composite Beam Theory*. John Wiley & Sons Inc., 2002.
- [27] V. L. Berdichevskii. Variational-asymptotic method of constructing a theory of shells. *Applied Mathematics and Mechanics*, 43(4):711–736, 1979.
- [28] M.J.S. Hirst and M.F. Yeo. The analysis of composite beams using standard finite element programs. *Computers and Structures*, 11(3):233–237, 1980.

- [29] Fuh-Gwo Yuan and Robert E. Miller. New finite element for laminated composite beams. *Computers and Structures*, 31(5):737–745, 1989.
- [30] J. Griffiths, F. Khouli, and F. F. Afagh. Nonlinear Static Analysis of Reducible Thin-Wall Active Open Cross-Section Beams Based on Generalized Vlasov Theory. In *Collection of Papers - 3<sup>rd</sup> International Conference on Integrity, Reliability and Failure*, Porto, Portugal, 20-24 July 2009. University of Toronto and University of Porto.
- [31] Carlos E. S. Cesnik, Vladislav G. Sutyryn, and Dewey H. Hodges. A Refined Composite Beam Theory Based on the Variational-Asymptotical Method. In *Collection of Technical Papers - 34<sup>th</sup> AIAA/ASME/ASCE/AHS/ASC Structures, Structural Dynamics, and Materials Conference*, La Jolla, CA, 19-22 April 1993. AIAA.
- [32] Rafael Palacios and Carlos E. S. Cesnik. Cross-Sectional Analysis of Nonhomogeneous Anisotropic Active Slender Structures. *AIAA Journal*, 43(12):2624–2638, 2005.
- [33] Sitikantha Roy, Wenbin Yu, and Dong Han. An asymptotically correct classical model for smart beams. *AIAA Journal*, 44(25-26):8424–8439, 2007.
- [34] V. V. Volovoi and D. H. Hodges. Theory of Anisotropic Thin-Walled Beams. *Journal of Applied Mechanics*, 67(3):453–459, 2000.
- [35] Vitali V. Volovoi and Dewey H. Hodges. Single- and Multicelled Composite Thin-Walled Beams. *AIAA Journal*, 40(5):960–965, 2002.
- [36] F. Khouli, R. G. Langlois, and F. F. Afagh. Analysis of active closed cross-section slender beams based on asymptotically correct thin-wall beam theory. *Smart Materials and Structures*, 16(1):221–229, 2007.

- [37] C.E.S. Cesnik and SangJoon Shin. On the twist performance of a multiple-cell active helicopter blade. *Smart Materials and Structures*, 10(1):53–61, 2001.
- [38] Jean-Marie Berthelot. *Composite Materials*. Springer-Verlag, 1999.
- [39] Andre Preumont. *Vibration Control of Active Structures: An Introduction*, volume 96 of *Solid Mechanics and Its Applications*. Springer, second edition edition, 2002.
- [40] A.A. Bent and N.W. Hagood. Piezoelectric fiber composites with interdigitated electrodes. *Journal of Intelligent Material Systems and Structures*, 8(11):903–919, 1997.
- [41] R. Brett Williams, Gyuhae Park, Daniel J. Inman, and W. Keats Wilkie. An overview of composite actuators with piezoceramic fibers. In *Proceedings of IMAC-XX: A Conference on Structural Dynamics*, Los Angeles, CA, 4-7 February 2002. SPIE.
- [42] DuPont. *Summary of Properties of Kapton® Polyimide Films*. [http://www2.dupont.com/Kapton/en\\_US/assets/downloads/pdf/summaryofprop.pdf](http://www2.dupont.com/Kapton/en_US/assets/downloads/pdf/summaryofprop.pdf).
- [43] Kanhaiya Lal Yadav and R.N.P. Choundhary. Piezoelectric properties of modified PZT ceramics. *Ferroelectrics*, 325:87–94, 2005.
- [44] L.A. Celi, A.C. Caballero, M. Villegas, and J. De Frutos. Effect of grain growth control on PZT properties. In *Tenth International Meeting on Ferroelectricity*, Madrid, Spain, 3-7 September 2001. Gordon & Breach.
- [45] Jae-Sang Park and Ji-Hwan Kim. Analytical development of single crystal macro fiber composite actuators for active twist rotor blades. *Smart Materials and Structures*, 14(4):745–753, 2005.
- [46] C.R. Bowen, L.J. Nelson, R. Stevens, M.G. Cain, and M. Stewart. Optimisation of interdigitated electrodes for piezoelectric actuators and active fibre composites. *Journal of Electroceramics*, 16(4):263–269, 2006.

- [47] Anthony W. Nutbourne. *Differential geometry applied to curve and surface design*. John Wiley & Sons Inc., 1987.
- [48] Anthony N. Palazotto and Scott T. Dennis. *Nonlinear Analysis of Shell Structures*. AIAA Education Series. AIAA, 1992.
- [49] V. Berdichevsky, E. Armanios, and A. Badir. Theory of anisotropic thin-walled closed-cross-section beams. *Composites Engineering*, 10(1):411–432, 1992.
- [50] Standards Committee of the IEEE Ultrasonics, Ferroelectrics, and Frequency Control Society. Ieee standard on piezoelectricity. Technical report, IEEE, January 1988.
- [51] Nicolaie Dan Cristescu, Eduard-Marius Craciun, and Eugen Soós. *Mechanics of Elastic Composites*. CRC Series: Modern Mechanics and Mathematics. Chapman & Hall/CRC, 2004.
- [52] Brent Bailey. Investigation of a composite hingeless helicopter rotor blade with integral actuators. Master’s thesis, Carleton University, 2000.
- [53] Atle Gjelsvik. *The Theory of Thin Walled Bars*. John Wiley & Sons Inc., 1981.
- [54] Carl M. Bender and Steven A. Orszag. *Advanced mathematical methods for scientists and engineers: Asymptotic Methods and Perturbation Theory*. McGraw-Hill, 1978.
- [55] Carlos Cesnik and Rafael Palacios. *UM/VABS Release 1.23 User’s Manual*. Active Aeroelasticity and Structures Research Laboratory: The University of Michigan, January 2005.
- [56] International Centre for Numerical Methods in Engineering: Universitat Politècnica de Catalunya. *GiD Version 9 Reference Manual*, June 2008. [http://gid.cimne.upc.es/support\\_team/su04.html](http://gid.cimne.upc.es/support_team/su04.html).

- [57] Fidel Khouli. *Cross-Sectional Analysis of Active Airfoils*. Applied Dynamics Group: Department of Mechanical and Aerospace Engineering, Carleton University, June 2009.
- [58] Dewey H. Hodges. A mixed variational formulation based on exact intrinsic equations for dynamics of moving beams. *International Journal of Solids and Structures*, 26(11):1253–1273, 1990.
- [59] Matthew W. Floros and Edward C. Smith. Finite element modeling of open-section composite beams with warping restraint effects. In *Proceedings of the 1996 37<sup>th</sup> AIAA/ASME/ASCE/AHS/ASC Structures, Structural Dynamics, and Materials Conference*, Salt Lake City, UT, 15-17 April 1996. AIAA.
- [60] Gerald W. Recktenwald. *Introduction to Numerical Methods and MATLAB: Implementations and Applications*. Prentice Hall, 2000.
- [61] Louis Komzsik. *Approximation Techniques for Engineers*. CRC/Taylor & Francis Group, LLC, 2007.
- [62] John P. Rogers and Nesbitt W. Hagood. Preliminary Mach-scale hover testing of an integral twist-actuated rotor blade. In *Proceedings of SPIE - The International Society for Optical Engineering*, San Diego, CA, 2-5 March 1998. SPIE.

# Appendix A

## A.1 Shell Energy

The following derivation transforms the shell energy from indicial notation form, Eq. 2.29, into matrix form. Repeating Eq. 2.29:

$$2\tilde{\mathcal{U}}^{(m)} = \int_{\Sigma} \int_s \int_{-\frac{\hbar}{2}}^{\frac{\hbar}{2}} D^{\alpha\beta\gamma\delta} (\gamma_{\alpha\beta} + \xi\rho_{\alpha\beta} - \bar{d}_{1\alpha\beta}E) (\gamma_{\gamma\delta} + \xi\rho_{\gamma\delta} - \bar{d}_{1\gamma\delta}E) d\xi ds \quad (\text{A.1})$$

Expanding Eq. A.1, yields

$$\begin{aligned}
2\tilde{\mathcal{U}}^{(m)} = & \int_{\Sigma} \int_{s} \int_{-\frac{h}{2}}^{\frac{h}{2}} \left( [D^{1111} (\gamma_{11} + \xi\rho_{11} - \bar{d}_{111}E) + 2D^{1112} (\gamma_{12} + \xi\rho_{12} - \bar{d}_{112}E) \right. \\
& \left. + D^{1122} (\gamma_{22} + \xi\rho_{22} - \bar{d}_{122}E)] (\gamma_{11} + \xi\rho_{11} - \bar{d}_{111}E) \right. \\
& \left. + [2D^{1112} (\gamma_{11} + \xi\rho_{11} - \bar{d}_{111}E) + 4D^{1212} (\gamma_{12} + \xi\rho_{12} - \bar{d}_{112}E) \right. \\
& \left. + 2D^{1222} (\gamma_{22} + \xi\rho_{22} - \bar{d}_{122}E)] (\gamma_{12} + \xi\rho_{12} - \bar{d}_{112}E) \right. \\
& \left. + [D^{1122} (\gamma_{11} + \xi\rho_{11} - \bar{d}_{111}E) + 2D^{1222} (\gamma_{12} + \xi\rho_{12} - \bar{d}_{112}E) \right. \\
& \left. + D^{2222} (\gamma_{22} + \xi\rho_{22} - \bar{d}_{122}E)] (\gamma_{22} + \xi\rho_{22} - \bar{d}_{122}E) \right) d\xi ds \tag{A.2}
\end{aligned}$$

$$\tag{A.3}$$

where the following symmetries have been used:  $\bar{d}_{112} = \bar{d}_{121}$ ,  $\gamma_{12} = \gamma_{21}$ ,  $\rho_{12} = \rho_{21}$ , and  $D^{\alpha\beta\gamma\delta} = D^{\beta\alpha\gamma\delta} = D^{\alpha\beta\delta\gamma} = D^{\gamma\delta\alpha\beta} = D^{\delta\gamma\alpha\beta} = D^{\gamma\delta\beta\alpha}$ .

Grouping terms in the integrand of Eq. A.3 that are quadratic in the known strains,  $\gamma_{11}\gamma_{11}$ ,  $\gamma_{11}\rho_{11}$ ,  $\gamma_{11}\rho_{12}$ ,  $\rho_{11}\rho_{11}$ ,  $\rho_{11}\rho_{12}$  and  $\rho_{12}\rho_{12}$ , as  $I_{\psi\psi}$ ; coupling between the known and unknown strains,  $\gamma_{12}\gamma_{11}$ ,  $\gamma_{12}\rho_{11}$ ,  $\gamma_{12}\rho_{12}$ ,  $\gamma_{22}\rho_{11}$ ,  $\gamma_{22}\rho_{12}$  and  $\rho_{22}\rho_{12}$ , as  $I_{\phi\psi}$ ; quadratic in the unknown strains,  $\gamma_{12}\gamma_{12}$ ,  $\gamma_{12}\gamma_{22}$ ,  $\gamma_{12}\rho_{22}$ ,  $\gamma_{22}\gamma_{22}$ ,  $\gamma_{22}\rho_{22}$  and  $\rho_{22}\rho_{22}$ , as  $I_{\phi\phi}$ ; coupling between the known strains and electromechanical strain components,  $\gamma_{11}\bar{d}_{1\alpha\beta}$ ,  $\rho_{11}\bar{d}_{1\alpha\beta}$  and  $\rho_{12}\bar{d}_{1\alpha\beta}$ , as  $I_{\psi\bar{d}_{1\alpha\beta}}$ ; coupling between the unknown strains and electromechanical strain components,  $\gamma_{12}\bar{d}_{1\alpha\beta}$ ,  $\gamma_{22}\bar{d}_{1\alpha\beta}$  and  $\rho_{22}\bar{d}_{1\alpha\beta}$ , as  $I_{\phi\bar{d}_{1\alpha\beta}}$ ; and quadratic in the electromechanical field,  $\bar{d}_{1\alpha\beta}\bar{d}_{1\gamma\delta}$ , as  $I_{\bar{d}_{1\alpha\beta}\bar{d}_{1\gamma\delta}}$ , yields

$$2\tilde{\mathcal{U}}^{(m)} = \int_{\Sigma} \int_{s} \int_{-\frac{h}{2}}^{\frac{h}{2}} \left( I_{\psi\psi} + I_{\phi\psi} + I_{\phi\phi} + I_{\psi\bar{d}_{1\alpha\beta}} + I_{\phi\bar{d}_{1\alpha\beta}} + I_{\bar{d}_{1\alpha\beta}\bar{d}_{1\gamma\delta}} \right) d\xi ds \tag{A.4}$$

where, after factoring out the known and unknown strain vectors,  $\boldsymbol{\psi}^T = \begin{bmatrix} \gamma_{11} & h\rho_{11} & h\rho_{12} \end{bmatrix}$

and  $\phi^T = \begin{bmatrix} 2\gamma_{12} & \gamma_{22} & h\rho_{22} \end{bmatrix}$ , respectively, gives

$$\begin{aligned}
I_{\psi\psi} &= \begin{bmatrix} \gamma_{11} & h\rho_{11} & h\rho_{12} \end{bmatrix} \begin{bmatrix} D^{1111} & D^{1111} \left(\frac{\xi}{h}\right) & 2D^{1112} \left(\frac{\xi}{h}\right) \\ D^{1111} \left(\frac{\xi}{h}\right) & D^{1111} \left(\frac{\xi}{h}\right)^2 & 2D^{1112} \left(\frac{\xi}{h}\right)^2 \\ 2D^{1112} \left(\frac{\xi}{h}\right) & 2D^{1112} \left(\frac{\xi}{h}\right)^2 & 4D^{1212} \left(\frac{\xi}{h}\right)^2 \end{bmatrix} \begin{bmatrix} \gamma_{11} \\ h\rho_{11} \\ h\rho_{12} \end{bmatrix} \\
I_{\phi\psi} &= 2 \begin{bmatrix} 2\gamma_{12} & \gamma_{22} & h\rho_{22} \end{bmatrix} \begin{bmatrix} D^{1112} & D^{1112} \left(\frac{\xi}{h}\right) & 2D^{1212} \left(\frac{\xi}{h}\right) \\ D^{1122} & D^{1122} \left(\frac{\xi}{h}\right) & 2D^{1222} \left(\frac{\xi}{h}\right) \\ D^{1122} \left(\frac{\xi}{h}\right) & D^{1122} \left(\frac{\xi}{h}\right)^2 & 2D^{1222} \left(\frac{\xi}{h}\right)^2 \end{bmatrix} \begin{bmatrix} \gamma_{11} \\ h\rho_{11} \\ h\rho_{12} \end{bmatrix} \\
I_{\phi\phi} &= \begin{bmatrix} 2\gamma_{12} & \gamma_{22} & h\rho_{22} \end{bmatrix} \begin{bmatrix} D^{1212} & D^{1222} & D^{1222} \left(\frac{\xi}{h}\right) \\ D^{1222} & D^{2222} & D^{2222} \left(\frac{\xi}{h}\right) \\ D^{1222} \left(\frac{\xi}{h}\right) & D^{2222} \left(\frac{\xi}{h}\right) & D^{2222} \left(\frac{\xi}{h}\right)^2 \end{bmatrix} \begin{bmatrix} 2\gamma_{12} \\ \gamma_{22} \\ h\rho_{22} \end{bmatrix} \\
I_{\psi\bar{d}_{1\alpha\beta}} &= -2 \begin{bmatrix} \gamma_{11} & h\rho_{11} & h\rho_{12} \end{bmatrix} \begin{bmatrix} (D^{1111}\bar{d}_{111} + 2D^{1112}\bar{d}_{112} + D^{1122}\bar{d}_{122}) E \\ (D^{1111}\bar{d}_{111} + 2D^{1112}\bar{d}_{112} + D^{1122}\bar{d}_{122}) \frac{\xi E}{h} \\ (2D^{1112}\bar{d}_{111} + 4D^{1212}\bar{d}_{112} + 2D^{1222}\bar{d}_{122}) \frac{\xi E}{h} \end{bmatrix} \\
I_{\phi\bar{d}_{1\alpha\beta}} &= -2 \begin{bmatrix} 2\gamma_{12} & \gamma_{22} & h\rho_{22} \end{bmatrix} \begin{bmatrix} (2D^{1112}\bar{d}_{111} + 4D^{1212}\bar{d}_{112} + 2D^{1222}\bar{d}_{122}) \frac{E}{2} \\ (D^{1122}\bar{d}_{111} + 2D^{1222}\bar{d}_{112} + D^{2222}\bar{d}_{122}) E \\ (D^{1122}\bar{d}_{111} + 2D^{1222}\bar{d}_{112} + D^{2222}\bar{d}_{122}) \frac{\xi E}{h} \end{bmatrix}
\end{aligned} \tag{A.5}$$

and the group of terms composing the quadratic electromechanical field can be collapsed into indicial notation form, as

$$I_{\bar{d}_{1\alpha\beta}\bar{d}_{1\gamma\delta}} = D^{\alpha\beta\gamma\delta} \bar{d}_{1\alpha\beta} \bar{d}_{1\gamma\delta} E^2 \tag{A.6}$$

Integrating through the shell thickness  $h$ , while recognizing that the shell strains,  $\gamma_{\alpha\beta}$

and  $\rho_{\alpha\beta}$ , are functions of the contour coordinate  $s$  only, gives

$$2\mathcal{U}^{(m)} = \int_{\Sigma_s} (\boldsymbol{\psi}^T \mathbf{Q} \boldsymbol{\psi} + 2\boldsymbol{\phi}^T \mathbf{S} \boldsymbol{\psi} + \boldsymbol{\phi}^T \mathbf{P} \boldsymbol{\phi} - 2\boldsymbol{\psi}^T \mathbf{H} - 2\boldsymbol{\phi}^T \mathbf{G} + \aleph(E)) ds \quad (\text{A.7})$$

where the  $\mathbf{Q}$ ,  $\mathbf{S}$  and  $\mathbf{P}$  matrices describe the laminate elastic material properties and are given by

$$\begin{aligned} \mathbf{Q} &= \begin{bmatrix} E_e^{1111} & E_{eb}^{1111} & 2E_{eb}^{1112} \\ E_{eb}^{1111} & E_b^{1111} & 2E_b^{1112} \\ 2E_{eb}^{1112} & 2E_b^{1112} & 4E_b^{1212} \end{bmatrix} \\ \mathbf{S} &= \begin{bmatrix} E_e^{1112} & E_{eb}^{1112} & 2E_{eb}^{1212} \\ E_e^{1122} & E_{eb}^{1122} & 2E_{eb}^{1222} \\ E_{eb}^{1122} & E_b^{1122} & 2E_b^{1222} \end{bmatrix} \\ \mathbf{P} &= \begin{bmatrix} E_e^{1212} & E_e^{1222} & E_{eb}^{1222} \\ E_e^{1222} & E_e^{2222} & E_{eb}^{2222} \\ E_{eb}^{1222} & E_{eb}^{2222} & E_b^{2222} \end{bmatrix} \end{aligned} \quad (\text{A.8})$$

where  $E_e^{\alpha\beta\gamma\delta}$ ,  $E_{eb}^{\alpha\beta\gamma\delta}$  and  $E_b^{\alpha\beta\gamma\delta}$  are the shell stretching, coupling and bending elastic stiffness constants, respectively, and are given as [34]

$$\left\{ E_e^{\alpha\beta\gamma\delta}, E_{eb}^{\alpha\beta\gamma\delta}, E_b^{\alpha\beta\gamma\delta} \right\} = \int_{-\frac{h}{2}}^{\frac{h}{2}} D^{\alpha\beta\gamma\delta} \left\{ 1, \frac{\xi}{h}, \left( \frac{\xi}{h} \right)^2 \right\} d\xi \quad (\text{A.9})$$

In Eq. 2.30,  $\mathbf{H}$  and  $\mathbf{G}$  are electromechanical coupling matrices given by

$$\mathbf{H} = \begin{bmatrix} Z_1^{(a)} \\ W_1^{(a)}/h \\ W_2^{(a)}/h \end{bmatrix} \quad \text{and} \quad \mathbf{G} = \begin{bmatrix} Z_2^{(a)}/2 \\ Z_3^{(a)} \\ W_3^{(a)}/h \end{bmatrix} \quad (\text{A.10})$$

where the  $Z_i^{(a)}$  and  $W_i^{(a)}$  components are

$$\begin{aligned} Z_1^{(a)} &= \int_{-\frac{h}{2}}^{\frac{h}{2}} [D^{1111}\bar{d}_{111} + 2D^{1112}\bar{d}_{112} + D^{1122}\bar{d}_{122}] E d\xi \\ Z_2^{(a)} &= \int_{-\frac{h}{2}}^{\frac{h}{2}} [2D^{1112}\bar{d}_{111} + 4D^{1212}\bar{d}_{112} + 2D^{1222}\bar{d}_{122}] E d\xi \\ Z_3^{(a)} &= \int_{-\frac{h}{2}}^{\frac{h}{2}} [D^{1122}\bar{d}_{111} + 2D^{1222}\bar{d}_{112} + D^{2222}\bar{d}_{122}] E d\xi \end{aligned} \quad (\text{A.11})$$

and

$$\begin{aligned} W_1^{(a)} &= \int_{-\frac{h}{2}}^{\frac{h}{2}} [D^{1111}\bar{d}_{111} + 2D^{1112}\bar{d}_{112} + D^{1122}\bar{d}_{122}] E\xi d\xi \\ W_2^{(a)} &= \int_{-\frac{h}{2}}^{\frac{h}{2}} [2D^{1112}\bar{d}_{111} + 4D^{1212}\bar{d}_{112} + 2D^{1222}\bar{d}_{122}] E\xi d\xi \\ W_3^{(a)} &= \int_{-\frac{h}{2}}^{\frac{h}{2}} [D^{1122}\bar{d}_{111} + 2D^{1222}\bar{d}_{112} + D^{2222}\bar{d}_{122}] E\xi d\xi \end{aligned} \quad (\text{A.12})$$

The final term in the integrand of Eq. 2.30,  $\aleph(E)$ , is a quadratic term of the electric field, given by

$$\aleph(E) = \int_{-\frac{h}{2}}^{\frac{h}{2}} D^{\alpha\beta\gamma\delta} \bar{d}_{1\alpha\beta} \bar{d}_{1\gamma\delta} E^2 d\xi \quad (\text{A.13})$$

## A.2 First Perturbed Strain Field

The following derivation finds the first perturbed strain field. Repeating the general strain field, Eq. 2.9, gives

$$\begin{aligned}
 \gamma_{11} &= v_{1,1} \\
 \rho_{11} &= v_{3,11} \\
 2\gamma_{12} &= v_{1,2} + v_{2,1} \\
 \rho_{12} &= v_{3,12} + \frac{1}{4R}(v_{1,2} - 3v_{2,1}) \\
 \gamma_{22} &= v_{2,2} + \frac{v_3}{R} \\
 \rho_{22} &= v_{3,22} - \left(\frac{v_2}{R}\right)_{,2}
 \end{aligned} \tag{A.14}$$

and the first perturbed displacement field, Eq. 2.48, as

$$\begin{aligned}
 v_1 &= u_1 + \hat{w}_1 \\
 v_2 &= u_\alpha \dot{x}_\alpha + \theta r_n + \hat{w}_2 \\
 v_3 &= u_2 \dot{x}_3 - u_3 \dot{x}_2 - \theta r_\tau + \hat{w}_3
 \end{aligned} \tag{A.15}$$

Substituting the first perturbed displacement field, Eq. A.15, into each strain component of the general strain field, Eq. A.14, yields, for  $\gamma_{11}$ ,  $h\rho_{11}$  and  $2\gamma_{12}$ ,

$$\gamma_{11} = u_1' - \hat{w}_{1,1} \tag{A.16}$$

$$\rho_{11} = h(u_2'' \dot{x}_3 - u_3'' \dot{x}_2 - \theta'' r_\tau + \hat{w}_{3,11}) \tag{A.17}$$

$$\begin{aligned}
2\gamma_{12} &= (u_{1,2} + \hat{w}_{1,2}) - (u'_\alpha \dot{x}_\alpha + \theta' r_n + \hat{w}_{2,1}) \\
&= u'_2 \dot{x}_2 + u'_3 \dot{x}_3 + \theta' r_n + \hat{w}_{1,2} + \hat{w}_{2,1}
\end{aligned} \tag{A.18}$$

where  $u_{1,2} = 0$  since  $u_1$  is a function of the axial coordinate  $x_1$  only. For  $h\rho_{12}$ ,

$$\begin{aligned}
h\rho_{12} &= h \left[ u'_2 \ddot{x}_3 - u'_3 \ddot{x}_2 - \theta' \dot{r}_\tau + \hat{w}_{3,12} \right. \\
&\quad \left. + \frac{1}{4R} (u_{1,2} + \hat{w}_{1,2} - 3u'_\alpha \dot{x}_\alpha - 3\theta' r_n - 3\hat{w}_{2,1}) \right] \\
&= h \left( \frac{1}{4R} (\dot{x}_\alpha u'_\alpha + r_n \theta' - \hat{w}_{1,2}) - \theta' + \hat{w}_{3,12} - \frac{3}{4R} \hat{w}_{2,1} \right)
\end{aligned} \tag{A.19}$$

where  $u_{1,2} = 0$ , the relations  $\ddot{x}_2 = \frac{\dot{x}_3}{R}$  and  $\ddot{x}_3 = \frac{\dot{x}_2}{R}$  from Eqs. 2.6 were used, and the following relation between  $\dot{r}_\tau$  and  $r_n$  was derived using Eqs. 2.3 and 2.6, as

$$\begin{aligned}
\dot{r}_\tau &= \dot{x}_2 \dot{x}_2 + \ddot{x}_2 x_2 + \dot{x}_3 \dot{x}_3 + \ddot{x}_3 x_3 \\
&= \left( \frac{\partial x_2}{\partial s} \right)^2 + \left( \frac{\partial x_3}{\partial s} \right)^2 - \frac{\dot{x}_3}{R} x_2 + \frac{\dot{x}_2}{R} x_3 \\
&= 1 - \frac{1}{R} r_n
\end{aligned} \tag{A.20}$$

where the Pythagorean theorem  $(\partial x_2)^2 + (\partial x_3)^2 = (\partial s)^2$  was used.

For  $\gamma_{22}$ ,

$$\begin{aligned}
\gamma_{22} &= (u_\alpha \ddot{x}_\alpha + \theta \dot{r}_n + \hat{w}_{2,2}) + \left( u_2 \frac{\dot{x}_3}{R} - u_3 \frac{\dot{x}_2}{R} - \theta \frac{r_\tau}{R} + \frac{\hat{w}_3}{R} \right) \\
&= \hat{w}_{2,2} + \frac{\hat{w}_3}{R}
\end{aligned} \tag{A.21}$$

where the relations  $\ddot{x}_2 = \frac{\dot{x}_3}{R}$  and  $\ddot{x}_3 = \frac{\dot{x}_2}{R}$  from Eqs. 2.6 were used, and the following relation between  $\dot{r}_n$  and  $r_\tau$  was derived using Eqs. 2.3 and 2.6, as

$$\begin{aligned}
\dot{r}_n &= \dot{x}_3 \dot{x}_2 + \ddot{x}_3 x_2 - \dot{x}_2 \dot{x}_3 - \ddot{x}_2 x_3 \\
&= \ddot{x}_3 x_2 - \ddot{x}_2 x_3 \\
&= \frac{\dot{x}_2}{R} x_2 + \frac{\dot{x}_3}{R} x_3 \\
&= \frac{1}{R} r_\tau
\end{aligned} \tag{A.22}$$

For  $h\rho_{22}$ ,

$$\begin{aligned}
h\rho_{22} &= h \left[ u_2 \ddot{x}_3 - u_3 \ddot{x}_2 - \theta \dot{r}_\tau + \hat{w}_{3,2} \right. \\
&\quad \left. - \frac{1}{4R} (u_\alpha \dot{x}_\alpha + \theta r_n + \hat{w}_2) \right]_{,2} \\
&= h \left[ \hat{w}_{3,2} - \frac{\hat{w}_2}{R} \right]_{,2}
\end{aligned} \tag{A.23}$$

where Eq. A.20 and the relations  $\ddot{x}_2 = \frac{\dot{x}_3}{R}$  and  $\ddot{x}_3 = \frac{\dot{x}_2}{R}$  from Eqs. 2.6 were used.

# Appendix B

## B.1 GiD to UM/VABS Interface Code

### B.1.1 Materials File: .mat

```
NUMBER: 1 MATERIAL: AS4/3506_0_deg END MATERIAL
NUMBER: 2 MATERIAL: AS4/3506_45_deg END MATERIAL
NUMBER: 3 MATERIAL: AS4/3506_90_deg END MATERIAL
NUMBER: 4 MATERIAL: AFC_0_deg_2000V END MATERIAL
NUMBER: 5 MATERIAL: AFC_45_deg_2000V END MATERIAL
NUMBER: 6 MATERIAL: AFC_-45_deg_2000V END MATERIAL
NUMBER: 7 MATERIAL: AFC_0_deg_-2000V END MATERIAL
NUMBER: 8 MATERIAL: AFC_45_deg_-2000V END MATERIAL
NUMBER: 9 MATERIAL: AFC_-45_deg_-2000V END MATERIAL
```

### B.1.2 Output Instructions File: .bas

```
$ -----
$ GENERAL INFO
$ -----
$ Number of Elements & Nodes:
$ *nelem *npoin
$ -----
$ NODES
$ -----
```

```

$ Node Y Z
*set elems(all)
*loop nodes
*format ‘‘%11i%23.4f%8.4f’’
GRID *NodesNum *NodesCoord(2,real)*NodesCoord(3,real)
*end nodes
$ -----
$ CONNECTIVITIES
$ -----
$ Element Material Node(1) Node(2) Node(3) Node(4)
$ Initially CW nodal assignments:
*set Layer LayerCW4321 *elems
$ LayerCW4321
*loop elems *OnlyInLayer
*format ‘‘%9i%7i%7i%7i%7i%7i’’
CQUAD4 *ElemsNum *ElemsMat *ElemsConec(4) *ElemsConec(3) *ElemsConec(2) *ElemsConec(1)
*end elems
$
*set Layer LayerCW3214 *elems
$ LayerCW3214
*loop elems *OnlyInLayer
*format ‘‘%9i%7i%7i%7i%7i%7i’’
CQUAD4 *ElemsNum *ElemsMat *ElemsConec(3) *ElemsConec(2) *ElemsConec(1) *ElemsConec(4)
*end elems
$
*set Layer LayerCW2143 *elems
$ LayerCW2143
*loop elems *OnlyInLayer
*format ‘‘%9i%7i%7i%7i%7i%7i’’
CQUAD4 *ElemsNum *ElemsMat *ElemsConec(2) *ElemsConec(1) *ElemsConec(4) *ElemsConec(3)
*end elems
$
*set Layer LayerCW1432 *elems
$ LayerCW1432
*loop elems *OnlyInLayer
*format ‘‘%9i%7i%7i%7i%7i%7i’’
CQUAD4 *ElemsNum *ElemsMat *ElemsConec(1) *ElemsConec(4) *ElemsConec(3) *ElemsConec(2)
*end elems
$

```

```

$ Initially CCW nodal assignments:
*set Layer LayerCCW1234 *elems
$ LayerCCW1234
*loop elems *OnlyInLayer
*format ‘‘%9i%7i%7i%7i%7i%7i’’
CQUAD4 *ElemsNum *ElemsMat *ElemsConec(1) *ElemsConec(2) *ElemsConec(3) *ElemsConec(4)
*end elems
$
*set Layer LayerCCW2341 *elems
$ LayerCCW2341
*loop elems *OnlyInLayer
*format ‘‘%9i%7i%7i%7i%7i%7i’’
CQUAD4 *ElemsNum *ElemsMat *ElemsConec(2) *ElemsConec(3) *ElemsConec(4) *ElemsConec(1)
*end elems
$
*set Layer LayerCCW3412 *elems
$ LayerCCW3412
*loop elems *OnlyInLayer
*format ‘‘%9i%7i%7i%7i%7i%7i’’
CQUAD4 *ElemsNum *ElemsMat *ElemsConec(3) *ElemsConec(4) *ElemsConec(1) *ElemsConec(2)
*end elems
$
*set Layer LayerCCW4123 *elems
$ LayerCCW4123
*loop elems *OnlyInLayer
*format ‘‘%9i%7i%7i%7i%7i%7i’’
CQUAD4 *ElemsNum *ElemsMat *ElemsConec(4) *ElemsConec(1) *ElemsConec(2) *ElemsConec(3)
*end elems
$ -----
$ MATERIALS
$ -----
$ -----Materials Used In AS4/3506-----
MAT3D 1 142E+9 9.8E+9 9.8E+9 6.00E+9 6.00E+9 4.80E+9 0.3 +
0.3 0.42 1
$ -----Materials Used In AFC_2000V-----
MAT3D 2 42.2E+9 17.5E+9 17.5E+9 5.5E+9 5.5E+9 4.4E+9 0.354 +
0.354 0.42 1
$
MAT5 2 381E-12 -16E-11 0 0 0 0 1.1E-3

```

TEMPD 2000

\$ -----Materials Used In AFC\_-2000V-----  
 MAT3D 3 42.2E+9 17.5E+9 17.5E+9 5.5E+9 5.5E+9 4.4E+9 0.354 +  
 0.354 0.42 1

\$

MAT5 3 -381E-12 16E-11 0 0 0 0 1.1E-3

\$ -----

\$ PROPERTIES

\$ -----

\$ -----Property: AS4/3506\_0.deg--

PSHELL 1 1 0

\$ -----Property: AS4/3506\_45.deg--

PSHELL 2 1 45

\$ -----Property: AS4/3506\_90.deg--

PSHELL 3 1 90

\$ -----Property: AFC\_0.deg\_2000V--

PSHELL 4 2 0

\$ -----Property: AFC\_45.deg\_2000V--

PSHELL 5 2 45

\$ -----Property: AFC\_-45.deg\_2000V--

PSHELL 6 2 -45

\$ -----Property: AFC\_0.deg\_-2000V--

PSHELL 7 3 0

\$ -----Property: AFC\_45.deg\_-2000V--

PSHELL 8 3 45

\$ -----Property: AFC\_-45.deg\_-2000V--

PSHELL 9 3 -45

\$ -----

\$ CONSTRAINTS

\$ -----

SPCADD 2

SPC1 2 123 1

SPC1 2 3 200

\$ -----

\$ CONTROL PARAMETERS

\$ -----

vParam DEBUG YES

vParam ECHO YES

vParam ORDER2 NO

```
vParam REORDER NO
vParam RENUMBER NO
vParam TIMOSH NO
vParam VLASOV YES
```

## B.2 Active OCSTWB Input and Output Files

### B.2.1 I-Beam Contour Input File: contour\_input.m

```
branch(1).branch_id = 1;
branch(1).path_to_origin = [0];
branch(1).x3 = (0:0.0005:0.05);
branch(1).x2(1:length(branch(1).x3)) = 0;
branch(1).laminates(1:length(branch(1).x3)) = 1;
branch(1).laminates_cont(1:length(branch(1).x3)) = ' ';
%
branch(2).branch_id = 2;
branch(2).path_to_origin = [1];
branch(2).x2 = (0:-0.0005:-0.05);
branch(2).x3(1:length(branch(2).x2)) = 0.0535;
branch(2).laminates(1:length(branch(1).x3)) = 2;
branch(2).laminates_cont(1:length(branch(2).x3)) = ' ';
%
branch(3).branch_id = 3;
branch(3).path_to_origin = [1];
branch(3).x2 = (0:0.0005:0.05);
branch(3).x3(1:length(branch(3).x2)) = 0.0535;
branch(3).laminates(1:length(branch(3).x3)) = 3;
branch(3).laminates_cont(1:length(branch(3).x3)) = ' ';
%
branch(4).branch_id = 4;
branch(4).path_to_origin = [0];
branch(4).x3 = (0:-0.0005:-0.05);
branch(4).x2(1:length(branch(4).x3)) = 0;
branch(4).laminates(1:length(branch(4).x3)) = 4;
branch(4).laminates_cont(1:length(branch(4).x3)) = ' ';
%
branch(5).branch_id = 5;
branch(5).path_to_origin = [4];
```

```

branch(5).x2 = (0:-0.0005:-0.05);
branch(5).x3(1:length(branch(5).x2)) = -0.0535;
branch(5).laminates(1:length(branch(5).x3)) = 5;
branch(5).laminates_cont(1:length(branch(5).x3)) = ' ';
%
branch(6).branch_id = 6;
branch(6).path_to_origin = [4];
branch(6).x2 = (0:0.0005:0.05);
branch(6).x3(1:length(branch(6).x2)) = -0.0535;
branch(6).laminates(1:length(branch(6).x3)) = 6;
branch(6).laminates_cont(1:length(branch(6).x3)) = ' ';

```

## B.2.2 I-Beam Laminates Input File: LaminatesInput.dat

Number\_of\_Regions 6

Region1 7.0E-3 7

```

ply1-AS4/3506-1 141.96E+9 9.79E+9 6.00E+9 4.80E+9 0.3 0.42 1.0E-3 0 0 0 0 0 1
ply2-AS4/3506-1 141.96E+9 9.79E+9 6.00E+9 4.80E+9 0.3 0.42 1.0E-3 0 0 0 0 0 1
ply3-AS4/3506-1 141.96E+9 9.79E+9 6.00E+9 4.80E+9 0.3 0.42 1.0E-3 0 0 0 0 0 1
ply4-AS4/3506-1 141.96E+9 9.79E+9 6.00E+9 4.80E+9 0.3 0.42 1.0E-3 0 0 0 0 0 1
ply5-AS4/3506-1 141.96E+9 9.79E+9 6.00E+9 4.80E+9 0.3 0.42 1.0E-3 0 0 0 0 0 1
ply6-AS4/3506-1 141.96E+9 9.79E+9 6.00E+9 4.80E+9 0.3 0.42 1.0E-3 0 0 0 0 0 1
ply7-AS4/3506-1 141.96E+9 9.79E+9 6.00E+9 4.80E+9 0.3 0.42 1.0E-3 0 0 0 0 0 1

```

Region2 7.0E-3 7

```

ply1-AS4/3506-1 141.96E+9 9.79E+9 6.00E+9 4.80E+9 0.3 0.42 1.0E-3 0 0 0 0 0 1
ply2-AFC 42.2E+9 17.5E+9 5.5E+9 4.4E+9 0.354 0.42 1.0E-3 0 1818.1E+3 381E-12 0 -160E-12 1
ply3-AFC 42.2E+9 17.5E+9 5.5E+9 4.4E+9 0.354 0.42 1.0E-3 0 1818.1E+3 381E-12 0 -160E-12 1
ply4-AS4/3506-1 141.96E+9 9.79E+9 6.00E+9 4.80E+9 0.3 0.42 1.0E-3 0 0 0 0 0 1
ply5-AFC 42.2E+9 17.5E+9 5.5E+9 4.4E+9 0.354 0.42 1.0E-3 0 1818.1E+3 381E-12 0 -160E-12 1
ply6-AFC 42.2E+9 17.5E+9 5.5E+9 4.4E+9 0.354 0.42 1.0E-3 0 1818.1E+3 381E-12 0 -160E-12 1
ply7-AS4/3506-1 141.96E+9 9.79E+9 6.00E+9 4.80E+9 0.3 0.42 1.0E-3 0 0 0 0 0 1

```

Region3 7.0E-3 7

```

ply1-AS4/3506-1 141.96E+9 9.79E+9 6.00E+9 4.80E+9 0.3 0.42 1.0E-3 0 0 0 0 0 1
ply2-AFC 42.2E+9 17.5E+9 5.5E+9 4.4E+9 0.354 0.42 1.0E-3 0 -1818.1E+3 381E-12 0 -160E-12 1
ply3-AFC 42.2E+9 17.5E+9 5.5E+9 4.4E+9 0.354 0.42 1.0E-3 0 -1818.1E+3 381E-12 0 -160E-12 1
ply4-AS4/3506-1 141.96E+9 9.79E+9 6.00E+9 4.80E+9 0.3 0.42 1.0E-3 0 0 0 0 0 1
ply5-AFC 42.2E+9 17.5E+9 5.5E+9 4.4E+9 0.354 0.42 1.0E-3 0 -1818.1E+3 381E-12 0 -160E-12 1
ply6-AFC 42.2E+9 17.5E+9 5.5E+9 4.4E+9 0.354 0.42 1.0E-3 0 -1818.1E+3 381E-12 0 -160E-12 1
ply7-AS4/3506-1 141.96E+9 9.79E+9 6.00E+9 4.80E+9 0.3 0.42 1.0E-3 0 0 0 0 0 1

```

Region4 7.0E-3 7

```

ply1-AS4/3506-1 141.96E+9 9.79E+9 6.00E+9 4.80E+9 0.3 0.42 1.0E-3 0 0 0 0 0 1
ply2-AS4/3506-1 141.96E+9 9.79E+9 6.00E+9 4.80E+9 0.3 0.42 1.0E-3 0 0 0 0 0 1
ply3-AS4/3506-1 141.96E+9 9.79E+9 6.00E+9 4.80E+9 0.3 0.42 1.0E-3 0 0 0 0 0 1
ply4-AS4/3506-1 141.96E+9 9.79E+9 6.00E+9 4.80E+9 0.3 0.42 1.0E-3 0 0 0 0 0 1
ply5-AS4/3506-1 141.96E+9 9.79E+9 6.00E+9 4.80E+9 0.3 0.42 1.0E-3 0 0 0 0 0 1
ply6-AS4/3506-1 141.96E+9 9.79E+9 6.00E+9 4.80E+9 0.3 0.42 1.0E-3 0 0 0 0 0 1
ply7-AS4/3506-1 141.96E+9 9.79E+9 6.00E+9 4.80E+9 0.3 0.42 1.0E-3 0 0 0 0 0 1
Region5 7.0E-3 7
ply1-AS4/3506-1 141.96E+9 9.79E+9 6.00E+9 4.80E+9 0.3 0.42 1.0E-3 0 0 0 0 0 1
ply2-AFC 42.2E+9 17.5E+9 5.5E+9 4.4E+9 0.354 0.42 1.0E-3 0 -1818.1E+3 381E-12 0 -160E-12 1
ply3-AFC 42.2E+9 17.5E+9 5.5E+9 4.4E+9 0.354 0.42 1.0E-3 0 -1818.1E+3 381E-12 0 -160E-12 1
ply4-AS4/3506-1 141.96E+9 9.79E+9 6.00E+9 4.80E+9 0.3 0.42 1.0E-3 0 0 0 0 0 1
ply5-AFC 42.2E+9 17.5E+9 5.5E+9 4.4E+9 0.354 0.42 1.0E-3 0 -1818.1E+3 381E-12 0 -160E-12 1
ply6-AFC 42.2E+9 17.5E+9 5.5E+9 4.4E+9 0.354 0.42 1.0E-3 0 -1818.1E+3 381E-12 0 -160E-12 1
ply7-AS4/3506-1 141.96E+9 9.79E+9 6.00E+9 4.80E+9 0.3 0.42 1.0E-3 0 0 0 0 0 1
Region6 7.0E-3 7
ply1-AS4/3506-1 141.96E+9 9.79E+9 6.00E+9 4.80E+9 0.3 0.42 1.0E-3 0 0 0 0 0 1
ply2-AFC 42.2E+9 17.5E+9 5.5E+9 4.4E+9 0.354 0.42 1.0E-3 0 1818.1E+3 381E-12 0 -160E-12 1
ply3-AFC 42.2E+9 17.5E+9 5.5E+9 4.4E+9 0.354 0.42 1.0E-3 0 1818.1E+3 381E-12 0 -160E-12 1
ply4-AS4/3506-1 141.96E+9 9.79E+9 6.00E+9 4.80E+9 0.3 0.42 1.0E-3 0 0 0 0 0 1
ply5-AFC 42.2E+9 17.5E+9 5.5E+9 4.4E+9 0.354 0.42 1.0E-3 0 1818.1E+3 381E-12 0 -160E-12 1
ply6-AFC 42.2E+9 17.5E+9 5.5E+9 4.4E+9 0.354 0.42 1.0E-3 0 1818.1E+3 381E-12 0 -160E-12 1
ply7-AS4/3506-1 141.96E+9 9.79E+9 6.00E+9 4.80E+9 0.3 0.42 1.0E-3 0 0 0 0 0 1

```

## B.2.3 Bimoment I-Beam Output

The classical 4x4 stiffness matrix

```

2.1832e+008      0 -1.0656e-008 4.2746e-010
      0 2.0167e+002      0      0
-1.0656e-008      0 4.2327e+005 4.7748e-012
4.2746e-010      0 4.7748e-012 9.9121e+004

```

The classical actuation vector

```

-1.1369e-013
0
-1.2621e-012
-3.9968e-014

```

The Vlasov-classical coupling terms

```

1.2506e-012 0 1.7053e-013 9.5213e-013

```

The Vlasov Rigidity

2.8799e+002

The Vlasov actuation moment

3.1577e+001

0

0

0

# Appendix C

## C.1 Nonlinear 1-D Beam Span Analysis Code

### C.1.1 Input File: beam\_input.m

```
function [Cij_F1Mia,analysis,length,rootBC,tipBC,T,Mw_root,Mw_tip, ...
    induced_actuation,number_of_elements] = beam_input

analysis = 'ActiveOCSTWB';      % 'ActiveOCSTWB', 'UMVABS' or 'GTVABS'
induced_actuation = 'uniform'; % 'passive', 'uniform' or 'reversed'
length = 1;                    % 1 m, GTVABS: 200, Gandhi: 62 in
number_of_elements = 120;

                                % boundary conditions:
rootBC = 'restrained';         % 'restrained' or 'freeToWarp'
tipBC = 'free';                % 'free' or 'warpingRestrained'

                                % applied loading:
Mw_root = 0;                   % root bimoment
Mw_tip = 0;                    % tip bimoment
T = 0;                         % tip torque

% C11;C22;C33;C44;C55;C12;C13;C14;C15;C23;C24;C25;C34;C35;C45;
% F1a;M1a;M2a;M3a;Mwa
Cij_F1Mia = [1.59E+008
2.50E+002
1.79E+005
3.34E+005
```

```

1.88E+003
-1.19E-012
7.39E+005
1.98E-009
1.55E-011
-2.44E-014
-4.24E+002
-6.29E+001
-2.07E-011
-9.09E-013
2.40E+004
8.74E-013
-2.88E+001
-3.77E-014
3.05E+002
2.29E+001];
end % function

```

### C.1.2 Input Processing File: process\_input.m

```

function [S11,S22,S33,S44,S55,S12,S13,S14,S15,S23,S24,S25,S34,S35,S45, ...
    F1a,M1a,M2a,M3a,Mwa,F1,F2,F3,M1,M2,M3,Mw,W,S,C,length,rootBC,tipBC, ...
    T,Mw_root,Mw_tip,number_of_elements] = process_input

[Cij_F1Mia,analysis,length,rootBC,tipBC,T,Mw_root,Mw_tip, ...
    induced_actuation,number_of_elements] = beam_input;

C11    = Cij_F1Mia(1);
C22    = Cij_F1Mia(2);
C33    = Cij_F1Mia(3);
C44    = Cij_F1Mia(4);
C55    = Cij_F1Mia(5);

C12    = Cij_F1Mia(6);
C13    = Cij_F1Mia(7);
C14    = Cij_F1Mia(8);
C15    = Cij_F1Mia(9);
C23    = Cij_F1Mia(10);
C24    = Cij_F1Mia(11);
C25    = Cij_F1Mia(12);

```

```
C34 = Cij_F1Mia(13);
C35 = Cij_F1Mia(14);
C45 = Cij_F1Mia(15);

% stiffness matrix
C = [C11 C12 C13 C14 C15;
     C12 C22 C23 C24 C25;
     C13 C23 C33 C34 C35;
     C14 C24 C34 C44 C45;
     C15 C25 C35 C45 C55];

% compatibility matrix
if (C15 ~= 0) || (C25 ~= 0) || (C35 ~= 0) || (C45 ~= 0) || (C55 ~= 0)
    S = inv(C);
else
    S = inv(C(1:4,1:4));
    S(1,5) = 0;
    S(2,5) = 0;
    S(3,5) = 0;
    S(4,5) = 0;
    S(5,5) = 0;
end % if

S11 = S(1,1);
S22 = S(2,2);
S33 = S(3,3);
S44 = S(4,4);
S55 = S(5,5);

S12 = S(1,2);
S13 = S(1,3);
S14 = S(1,4);
S15 = S(1,5);
S23 = S(2,3);
S24 = S(2,4);
S25 = S(2,5);
S34 = S(3,4);
S35 = S(3,5);
S45 = S(4,5);
```

```

% initializing the active force vectors
F1a = zeros(number_of_elements+1,1);
M1a = zeros(number_of_elements+1,1);
M2a = zeros(number_of_elements+1,1);
M3a = zeros(number_of_elements+1,1);
Mwa = zeros(number_of_elements+1,1);

if strcmp(induced_actuation,'passive') % 'passive', 'uniform' or 'reversed')
    firstHalf = 0;
    secondHalf = 0;
elseif strcmp(induced_actuation,'uniform')
    firstHalf = 1;
    secondHalf = 1;
elseif strcmp(induced_actuation,'reversed')
    firstHalf = 1; % positive direction
    secondHalf = -1; % -1, reverse direction
else
    error('Not a root boundary condition. rootBC= ' 'restrained' 'or' 'freeToWarp''')
end % if

if strcmp(analysis, 'ActiveDCSTWB') || strcmp(analysis, 'GTVABS')
    b = 1;
elseif strcmp(analysis, 'UMVABS')
    b = -1;
end % if

for i = 1:(number_of_elements+1)
    if i < round(number_of_elements/2)
        polarity = firstHalf;
    else
        polarity = secondHalf;
    end % if
    F1a(i) = Cij_F1Mia(16) * b * polarity;
    M1a(i) = Cij_F1Mia(17) * b * polarity;
    M2a(i) = Cij_F1Mia(18) * polarity;
    M3a(i) = Cij_F1Mia(19) * b * polarity;
    Mwa(i) = Cij_F1Mia(20) * b * polarity;
end % for

```

```

% Assigning the initial guess nodal values
c = -40;
for j = 1:(number_of_elements+1)
    F1(j,1) = c;
    F2(j,1) = c;
    F3(j,1) = c;
    M1(j,1) = c;
    M2(j,1) = c;
    M3(j,1) = c;
    Mw(j,1) = c;
    W(j,1) = c;
end % for

end % function

```

### C.1.3 Main Analysis File: beam\_displacement\_twist.m

```

function beam_displacement_twist

clc
clear
format short e

[S11,S22,S33,S44,S55,S12,S13,S14,S15,S23,S24,S25,S34,S35,S45, ...
    F1a,M1a,M2a,M3a,Mwa,F1,F2,F3,M1,M2,M3,Mw,W,S,C,length,rootBC,tipBC, ...
    T,Mw_root,Mw_tip,number_of_elements] = process_input;

% Newton Raphson
number_of_iterations = 50; % 100
[F1, F2, F3, M1, M2, M3, Mw, W] = newton_raphson(S11, S22, ...
S33, S44, S55, S12, S13, S14, S15, S23, S24, S25, S34, S35, S45, F1a, ...
M1a, M2a, M3a, Mwa, F1, F2, F3, M1, M2, M3, Mw, W, number_of_elements, ...
number_of_iterations, T, rootBC, length, Mw_tip, tipBC, Mw_root);

% nonlinear displacement and twist recovery
% constructing the input variables
Xf = zeros(number_of_elements+1,1);
Xf(1) = W(number_of_elements+1);
for kk = 2:number_of_elements+1

```

```

Xf(8*(kk-2)+2) = F1((number_of_elements+2)-kk);
Xf(8*(kk-2)+3) = F2((number_of_elements+2)-kk);
Xf(8*(kk-2)+4) = F3((number_of_elements+2)-kk);
Xf(8*(kk-2)+5) = M1((number_of_elements+2)-kk);
Xf(8*(kk-2)+6) = M2((number_of_elements+2)-kk);
Xf(8*(kk-2)+7) = M3((number_of_elements+2)-kk);
Xf(8*(kk-2)+8) = Mw((number_of_elements+2)-kk);
Xf(8*(kk-2)+9) = W((number_of_elements+2)-kk);
end % for

delta_x = length/number_of_elements;
number_beam_elements = number_of_elements;
Flexibility_Matrix = S;
FreeTipBCs = [F1(number_of_elements+1); F2(number_of_elements+1); F3(number_of_elements
+1); M1(number_of_elements+1); M2(number_of_elements+1); M3(number_of_elements+1); Mw(
number_of_elements+1)];

y = deformation_rotations(Xf,delta_x,number_beam_elements, Flexibility_Matrix, FreeTipBCs,
    F1a,M1a,M2a,M3a,Mwa);
y.tip_twist_angle;
theta = flipud(y.tip_twist_angle');

C_deformation = y.CBb;
y = deformation_displacements(Xf,delta_x,number_beam_elements, Flexibility_Matrix,
    FreeTipBCs,F1a,M1a,M2a,M3a,Mwa,C_deformation);
for k = 1:number_of_elements+1
    U_1(k) = y{k}(1);
    U_2(k) = y{k}(2);
    U_3(k) = y{k}(3);
end % for
U1 = flipud(U_1');
U2 = flipud(U_2');
U3 = flipud(U_3');

% reducing the number of elements to 10 and arranging the forces in a column vector from
    root to tip
x = 0:length/number_of_elements:length; % x1 coordinate from tip to root
number_of_elements = 10;
xi = 0:length/number_of_elements:length;

```

```

% output
U1 = interp1(x,U1,xi)'
U2 = interp1(x,U2,xi)'
U3 = interp1(x,U3,xi)'
theta = interp1(x,theta,xi)'

end % function

```

### C.1.4 Equations Assembly File: equations.m

```

function equations = equations(S11, S22, S33, S44, S55, S12, S13, S14, ...
    S15, S23, S24, S25, S34, S35, S45, F1a, M1a, M2a, M3a, Mwa, ...
    F1, F2, F3, M1, M2, M3, Mw, W, number_of_elements, rootBC, length, T, Mw_tip,
    tipBC, Mw_root)

EquationsSize = 8*number_of_elements+8;
EquationsArray = zeros(EquationsSize,1);
dx = length/number_of_elements;

for i = 1:number_of_elements
    % first-order accurate forward difference equations
    Equations = [(F1(i+1) - F1(i)) / dx - F2(i) * (S14 * (F1(i) - F1a(i)) + S24 * (M1(i)
        - M1a(i)) + S34 * (M2(i) - M2a(i)) + S44 * (M3(i) - M3a(i)) + S45 * (Mw(i) - Mwa(i)
        ))) + F3(i) * (S13 * (F1(i) - F1a(i)) + S23 * (M1(i) - M1a(i)) + S33 * (M2(i) -
        M2a(i)) + S34 * (M3(i) - M3a(i)) + S35 * (Mw(i) - Mwa(i))) (F2(i+1) - F2(i)) / dx
        - F3(i) * (S12 * (F1(i) - F1a(i)) + S22 * (M1(i) - M1a(i)) + S23 * (M2(i) - M2a(i)
        )) + S24 * (M3(i) - M3a(i)) + S25 * (Mw(i) - Mwa(i))) + F1(i) * (S14 * (F1(i) - F1a
        (i)) + S24 * (M1(i) - M1a(i)) + S34 * (M2(i) - M2a(i)) + S44 * (M3(i) - M3a(i)) +
        S45 * (Mw(i) - Mwa(i))) (F3(i+1) - F3(i)) / dx - F1(i) * (S13 * (F1(i) - F1a(i)) +
        S23 * (M1(i) - M1a(i)) + S33 * (M2(i) - M2a(i)) + S34 * (M3(i) - M3a(i)) + S35 *
        (Mw(i) - Mwa(i))) + F2(i) * (S12 * (F1(i) - F1a(i)) + S22 * (M1(i) - M1a(i)) + S23
        * (M2(i) - M2a(i)) + S24 * (M3(i) - M3a(i)) + S25 * (Mw(i) - Mwa(i))) (M1(i+1) -
        M1(i)) / dx - M2(i) * (S14 * (F1(i) - F1a(i)) + S24 * (M1(i) - M1a(i)) + S34 * (M2
        (i) - M2a(i)) + S44 * (M3(i) - M3a(i)) + S45 * (Mw(i) - Mwa(i))) + M3(i) * (S13 *
        (F1(i) - F1a(i)) + S23 * (M1(i) - M1a(i)) + S33 * (M2(i) - M2a(i)) + S34 * (M3(i)
        - M3a(i)) + S35 * (Mw(i) - Mwa(i))) - (W(i+1) - W(i)) / dx (M2(i+1) - M2(i)) / dx
        - M3(i) * (S12 * (F1(i) - F1a(i)) + S22 * (M1(i) - M1a(i)) + S23 * (M2(i) - M2a(i)
        )) + S24 * (M3(i) - M3a(i)) + S25 * (Mw(i) - Mwa(i))) + M1(i) * (S14 * (F1(i) - F1a
        (i)) + S24 * (M1(i) - M1a(i)) + S34 * (M2(i) - M2a(i)) + S44 * (M3(i) - M3a(i)) +
        S45 * (Mw(i) - Mwa(i))) - F3(i) - W(i) * (S14 * (F1(i) - F1a(i)) + S24 * (M1(i) -

```

```

M1a(i)) + S34 * (M2(i) - M2a(i)) + S44 * (M3(i) - M3a(i)) + S45 * (Mw(i) - Mwa(i))
) (M3(i+1) - M3(i)) / dx - M1(i) * (S13 * (F1(i) - F1a(i)) + S23 * (M1(i) - M1a(i))
) + S33 * (M2(i) - M2a(i)) + S34 * (M3(i) - M3a(i)) + S35 * (Mw(i) - Mwa(i))) + M2
(i) * (S12 * (F1(i) - F1a(i)) + S22 * (M1(i) - M1a(i)) + S23 * (M2(i) - M2a(i)) +
S24 * (M3(i) - M3a(i)) + S25 * (Mw(i) - Mwa(i))) + F2(i) + W(i) * (S13 * (F1(i) -
F1a(i)) + S23 * (M1(i) - M1a(i)) + S33 * (M2(i) - M2a(i)) + S34 * (M3(i) - M3a(i))
+ S35 * (Mw(i) - Mwa(i))) S12 * (F1(i+1) - F1(i)) / dx + S22 * (M1(i+1) - M1(i))
/ dx + S23 * (M2(i+1) - M2(i)) / dx + S24 * (M3(i+1) - M3(i)) / dx + S25 * W(i) -
S15 * (F1(i) - F1a(i)) - S25 * (M1(i) - M1a(i)) - S35 * (M2(i) - M2a(i)) - S45 * (
M3(i) - M3a(i)) - S55 * (Mw(i) - Mwa(i)) W(i) - (Mw(i+1) - Mw(i)) / dx];

if i == 1 % additional root equation
    if strcmp(rootBC, 'restrained')
        EquationsArray(i) = S12*(F1(i)-F1a(i))+S22*(M1(i)-M1a(i))+S23*(M2(i)-M2a(i))+
            S24*(M3(i)-M3a(i))+S25*(Mw(i)-Mwa(i));
    elseif strcmp(rootBC, 'freeToWarp')
        EquationsArray(i) = Mw(i)-Mw_root;
    else
        error('Not a root boundary condition. rootBC = ' 'restrained' ' or ' 'freeToWarp
            ''')
    end % if
end % if

if i == number_of_elements % additional tip equation
    if strcmp(tipBC, 'free')
        EquationsArray(1+i*8+1) = F1(i+1);
        EquationsArray(1+i*8+2) = F2(i+1);
        EquationsArray(1+i*8+3) = F3(i+1);
        EquationsArray(1+i*8+4) = M1(i+1)-(W(i+1)+T);
        EquationsArray(1+i*8+5) = M2(i+1);
        EquationsArray(1+i*8+6) = M3(i+1);
        EquationsArray(1+i*8+7) = Mw(i+1)-Mw_tip;
    elseif strcmp(tipBC, 'warpingRestrained')
        EquationsArray(1+i*8+1) = F1(i+1);
        EquationsArray(1+i*8+2) = F2(i+1);
        EquationsArray(1+i*8+3) = F3(i+1);
        EquationsArray(1+i*8+4) = M1(i+1)-(W(i+1)+T);
        EquationsArray(1+i*8+5) = M2(i+1);
        EquationsArray(1+i*8+6) = M3(i+1);
    end % if
end % if

```

```

        EquationsArray(1+i*8+7) = S12*(F1(i+1)-F1a(i+1))+S22*(M1(i+1)-M1a(i+1))+S23*(
            M2(i+1)-M2a(i+1))+S24*(M3(i+1)-M3a(i+1))+S25*(Mw(i+1)-Mwa(i+1));
    else
        error('Not a tip boundary condition. tipBC= 'free' or 'warpingRestrained'
            ');
    end % if
end % if

for j = 1:8
    EquationsArray(1+(i-1)*8+j) = Equations(j);
end % for

end % for

equations = EquationsArray;
end % function

```

### C.1.5 Jacobian Assembly File: jacobian.m

```

function jacobian = jacobian(S11, S22, S33, S44, S55, S12, S13, S14, ...
    S15, S23, S24, S25, S34, S35, S45, F1a, M1a, M2a, M3a, Mwa, ...
    F1, F2, F3, M1, M2, M3, Mw, W, number_of_elements, rootBC, length, tipBC)

% Initializing the global Jacobian matrix
GlobalJacobianSize = 8*number_of_elements+8;
GlobalJacobian = zeros(GlobalJacobianSize,GlobalJacobianSize);
dx = length/number_of_elements;

for i = 1:number_of_elements
    % first-order accurate Jacobian
    LocalJacobian = [-0.1e1 / dx - F2(i) * S14 + F3(i) * S13 -S14 * (F1(i) - F1a(i)) -
        S24 * (M1(i) - M1a(i)) - S34 * (M2(i) - M2a(i)) - S44 * (M3(i) - M3a(i)) - S45 * (
        Mw(i) - Mwa(i)) S13 * (F1(i) - F1a(i)) + S23 * (M1(i) - M1a(i)) + S33 * (M2(i) -
        M2a(i)) + S34 * (M3(i) - M3a(i)) + S35 * (Mw(i) - Mwa(i)) -F2(i) * S24 + F3(i) *
        S23 -F2(i) * S34 + F3(i) * S33 -F2(i) * S44 + F3(i) * S34 -F2(i) * S45 + F3(i) *
        S35 0 0.1e1 / dx 0 0 0 0 0 0; -F3(i) * S12 + S14 * (F1(i) - F1a(i)) + S24 * (M1(
        i) - M1a(i)) + S34 * (M2(i) - M2a(i)) + S44 * (M3(i) - M3a(i)) + S45 * (Mw(i) -
        Mwa(i)) + F1(i) * S14 -0.1e1 / dx -S12 * (F1(i) - F1a(i)) - S22 * (M1(i) - M1a(i))
        - S23 * (M2(i) - M2a(i)) - S24 * (M3(i) - M3a(i)) - S25 * (Mw(i) - Mwa(i)) -F3(i)

```

```

* S22 + F1(i) * S24 -F3(i) * S23 + F1(i) * S34 -F3(i) * S24 + F1(i) * S44 -F3(i)
* S25 + F1(i) * S45 0 0 0.1e1 / dx 0 0 0 0 0 0; -S13 * (F1(i) - F1a(i)) - S23 * (
M1(i) - M1a(i)) - S33 * (M2(i) - M2a(i)) - S34 * (M3(i) - M3a(i)) - S35 * (Mw(i) -
Mwa(i)) - F1(i) * S13 + F2(i) * S12 S12 * (F1(i) - F1a(i)) + S22 * (M1(i) - M1a(i)
)) + S23 * (M2(i) - M2a(i)) + S24 * (M3(i) - M3a(i)) + S25 * (Mw(i) - Mwa(i)) -0.1
e1 / dx -F1(i) * S23 + F2(i) * S22 -F1(i) * S33 + F2(i) * S23 -F1(i) * S34 + F2(i)
* S24 -F1(i) * S35 + F2(i) * S25 0 0 0 0.1e1 / dx 0 0 0 0 0 0; -M2(i) * S14 + M3(i)
* S13 0 0 -0.1e1 / dx - M2(i) * S24 + M3(i) * S23 -S14 * (F1(i) - F1a(i)) - S24 *
(M1(i) - M1a(i)) - S34 * (M2(i) - M2a(i)) - S44 * (M3(i) - M3a(i)) - S45 * (Mw(i)
- Mwa(i)) - M2(i) * S34 + M3(i) * S33 -M2(i) * S44 + S13 * (F1(i) - F1a(i)) + S23
* (M1(i) - M1a(i)) + S33 * (M2(i) - M2a(i)) + S34 * (M3(i) - M3a(i)) + S35 * (Mw(
i) - Mwa(i)) + M3(i) * S34 -M2(i) * S45 + M3(i) * S35 0.1e1 / dx 0 0 0 0.1e1 / dx
0 0 0 -0.1e1 / dx; -M3(i) * S12 + M1(i) * S14 - W(i) * S14 0 -1 -M3(i) * S22 + S14
* (F1(i) - F1a(i)) + S24 * (M1(i) - M1a(i)) + S34 * (M2(i) - M2a(i)) + S44 * (M3(
i) - M3a(i)) + S45 * (Mw(i) - Mwa(i)) + M1(i) * S24 - W(i) * S24 -0.1e1 / dx - M3(
i) * S23 + M1(i) * S34 - W(i) * S34 -S12 * (F1(i) - F1a(i)) - S22 * (M1(i) - M1a(i)
)) - S23 * (M2(i) - M2a(i)) - S24 * (M3(i) - M3a(i)) - S25 * (Mw(i) - Mwa(i)) - M3
(i) * S24 + M1(i) * S44 - W(i) * S44 -M3(i) * S25 + M1(i) * S45 - W(i) * S45 -S14
* (F1(i) - F1a(i)) - S24 * (M1(i) - M1a(i)) - S34 * (M2(i) - M2a(i)) - S44 * (M3(i)
) - M3a(i)) - S45 * (Mw(i) - Mwa(i)) 0 0 0 0 0.1e1 / dx 0 0 0 0; -M1(i) * S13 + M2(i)
) * S12 + W(i) * S13 1 0 -S13 * (F1(i) - F1a(i)) - S23 * (M1(i) - M1a(i)) - S33 *
(M2(i) - M2a(i)) - S34 * (M3(i) - M3a(i)) - S35 * (Mw(i) - Mwa(i)) - M1(i) * S23 +
M2(i) * S22 + W(i) * S23 -M1(i) * S33 + S12 * (F1(i) - F1a(i)) + S22 * (M1(i) -
M1a(i)) + S23 * (M2(i) - M2a(i)) + S24 * (M3(i) - M3a(i)) + S25 * (Mw(i) - Mwa(i))
+ M2(i) * S23 + W(i) * S33 -0.1e1 / dx - M1(i) * S34 + M2(i) * S24 + W(i) * S34 -
M1(i) * S35 + M2(i) * S25 + W(i) * S35 S13 * (F1(i) - F1a(i)) + S23 * (M1(i) - M1a
(i)) + S33 * (M2(i) - M2a(i)) + S34 * (M3(i) - M3a(i)) + S35 * (Mw(i) - Mwa(i)) 0
0 0 0 0 0.1e1 / dx 0 0 0; -S12 / dx - S15 0 0 -S22 / dx - S25 -S23 / dx - S35 -S24 /
dx - S45 -S55 S25 S12 / dx 0 0 S22 / dx S23 / dx S24 / dx 0 0 0 0 0 0 0.1e1
/ dx 1 0 0 0 0 0 -0.1e1 / dx 0];

```

```

if i == 1 % additional row at top

```

```

    if strcmp(rootBC,'restrained')

```

```

        GlobalJacobian(i,1:8) = [S12 0 0 S22 S23 S24 S25 0];

```

```

    elseif strcmp(rootBC,'freeToWarp')

```

```

        GlobalJacobian(i,1:8) = [0 0 0 0 0 0 1 0];

```

```

    else

```

```

        error('Not a root boundary condition. rootBC = 'rootBC' or 'freeToWarp'
        ');

```

```

end % if

for j = 1:8
    for k = 1:16
        GlobalJacobian(1+(i-1)*8+j, (i-1)*8+k) = LocalJacobian(j,k);
    end % for
end % for

elseif i == number_of_elements % tip element

if strcmp(tipBC,'free')
    % last column: node i+1, element i
    GlobalJacobian(GlobalJacobianSize-8, GlobalJacobianSize) = S22/dx; % S22/dx
    --- differentiation w.r.t. W
    GlobalJacobian((GlobalJacobianSize-6):GlobalJacobianSize, (GlobalJacobianSize
    -7):GlobalJacobianSize) = ...
    [1 0 0 0 0 0 0 0; % F1
    0 1 0 0 0 0 0 0; % F2
    0 0 1 0 0 0 0 0; % F3
    0 0 0 1 0 0 0 -1; % M1
    0 0 0 0 1 0 0 0; % M2
    0 0 0 0 0 1 0 0; % M3
    0 0 0 0 0 0 1 0]; % Mw
elseif strcmp(tipBC,'warpingRestrained')
    % last column: node i+1, element i
    GlobalJacobian(GlobalJacobianSize-8, GlobalJacobianSize) = S22/dx; % S22/dx
    --- differentiation w.r.t. W
    GlobalJacobian(GlobalJacobianSize-7, GlobalJacobianSize-1) = -1/dx; % -1/dx
    --- differentiation w.r.t. Mw
    GlobalJacobian((GlobalJacobianSize-6):GlobalJacobianSize, (GlobalJacobianSize
    -7):GlobalJacobianSize) = ...
    [1 0 0 0 0 0 0 0; % F1
    0 1 0 0 0 0 0 0; % F2
    0 0 1 0 0 0 0 0; % F3
    0 0 0 1 0 0 0 -1; % M1
    0 0 0 0 1 0 0 0; % M2
    0 0 0 0 0 1 0 0; % M3
    S12 0 0 S22 S23 S24 S25 0]; % Mw
else

```

```

        error('Not a tip boundary condition. tipBC= ' 'free' 'or' 'warpingRestrained'
            ''')
    end % if

    % node i, element i
    for j = 1:8
        for k = 1:8
            GlobalJacobian(1+(i-1)*8+j, (i-1)*8+k) = LocalJacobian(j,k);
        end % for
    end % for

else
    for j = 1:8
        for k = 1:16
            GlobalJacobian(1+(i-1)*8+j, (i-1)*8+k) = LocalJacobian(j,k);
        end % for
    end % for
end % if

end % for

jacobian = GlobalJacobian;
end % function

```

### C.1.6 Newton-Raphson Equation Solver File: newton\_raphson.m

```

function [F1, F2, F3, M1, M2, M3, Mw, W] = newton_raphson(S11, S22, ...
    S33, S44, S55, S12, S13, S14, S15, S23, S24, S25, S34, S35, S45, F1a, ...
    M1a, M2a, M3a, Mwa, F1, F2, F3, M1, M2, M3, Mw, W, number_of_elements, ...
    number_of_iterations, T, rootBC, length, Mw_tip, tipBC, Mw_root)

% Solving for the nodal values using the Newton-Raphson method
for k = 1:number_of_iterations

    J = jacobian(S11, S22, S33, S44, S55, S12, S13, S14, ...
        S15, S23, S24, S25, S34, S35, S45, F1a, M1a, M2a, M3a, Mwa, ...
        F1, F2, F3, M1, M2, M3, Mw, W, number_of_elements, rootBC, length, tipBC);

    f = equations(S11, S22, S33, S44, S55, S12, S13, S14, ...
        S15, S23, S24, S25, S34, S35, S45, F1a, M1a, M2a, M3a, Mwa, ...

```

```

    F1, F2, F3, M1, M2, M3, Mw, W, number_of_elements, rootBC, length, T, Mw_tip,
        tipBC, Mw_root);

dx = -J\f;

% check
if (k == 1) || (mod(k,20) == 0)
    IterationNumber = k
    sizeJ = size(J)
    rankJ = rank(J)
end % if
gFiniteDiffNewton = norm(f)^2
deltaX = norm(dx);

% Updating estimated nodal values (Xnew = Xold + dx)
for j = 1:(number_of_elements+1)
    F1(j) = F1(j) + dx((j-1)*8+1);
    F2(j) = F2(j) + dx((j-1)*8+2);
    F3(j) = F3(j) + dx((j-1)*8+3);
    M1(j) = M1(j) + dx((j-1)*8+4);
    M2(j) = M2(j) + dx((j-1)*8+5);
    M3(j) = M3(j) + dx((j-1)*8+6);
    Mw(j) = Mw(j) + dx((j-1)*8+7);
    W(j) = W(j) + dx((j-1)*8+8);
end % for

if gFiniteDiffNewton < 1e-10
    F1;
    F2;
    F3;
    M1;
    M2;
    M3;
    Mw;
    W;
    f = equations(S11, S22, S33, S44, S55, S12, S13, S14, ...
        S15, S23, S24, S25, S34, S35, S45, F1a, M1a, M2a, M3a, Mwa, ...
        F1, F2, F3, M1, M2, M3, Mw, W, number_of_elements, rootBC, length, T, Mw_tip,
            tipBC, Mw_root);

```

```

        return
    end % if

end % for
end % function

```

## C.2 3-D FEA Displacement and Twist Post-processing

### Code

#### C.2.1 Read 3-D FEA Output File: read\_ansys\_results.m

```

function node_coord_displ = read_ANSYS_results

% reading the two ANSYS nodal coordinates and displacement output text files into matrices
NCoord = txt2mat('bimomentibeamNodalCoordinates',0,-1); % 0 header lines, no text
        wrapping; empty positions replaced with 'NaN'
NDispl = txt2mat('bimomentibeamNodalDisplacements',0,-1);

lengthNCoord = length(NCoord);
lengthNDispl = length(NDispl);

% removing the empty rows and the fifth column of NDispl
NCoordReduced = intersect(NCoord,NCoord,'rows');
NDisplReduced = intersect(NDispl,NDispl,'rows');
NDisplReduced = NDisplReduced(:,1:4);

NCoordNodes = NCoordReduced(:,1);
NDisplNodes = NDisplReduced(:,1);

[Nodes, iCoord, iDispl] = intersect(NCoordNodes, NDisplNodes);

NResults = zeros(length(Nodes),7);

% assembling the node numbers, nodal coordinates and nodal displacements into a single
matrix
for i = 1:length(Nodes)
    NResults(i,1:4) = NCoordReduced(iCoord(i),1:4);
    NResults(i,5:7) = NDisplReduced(iDispl(i),2:4);

```

```

end % for

node_coord_displ = NResults;

end % function

```

## C.2.2 Main Analysis File: beam\_displ\_rot.m

```

function beam_displ_rot(node_coord_displ)

% beam length
length = 1; % 1 m or 200

beam_station = length:-length/20:0;

% initial guess values at tip
x0 = [0,0,0]; % [U2,U3,theta] [m,m,rad]

% initializing the unknown variables
U2 = zeros(1,length(beam_station));
U3 = zeros(1,length(beam_station));
theta = zeros(1,length(beam_station));
min_function = zeros(length(beam_station),1);

for j = 1:length(beam_station)
    % initializing the cross-sectional variables
    k = 0;
    % finding the closest X value to the beam_station
    smallestDiff = length;
    closestX = 0;
    for i = 1:length(node_coord_displ)
        diff = abs(node_coord_displ(i,2)-beam_station(j));
        if diff < smallestDiff
            smallestDiff = diff;
            closestX = node_coord_displ(i,2);
        end % if
    end % for
    % finding the number of nodes in the cross section closest to the beam_station
    for i = 1:length(node_coord_displ)
        if node_coord_displ(i,2) == closestX

```

```

        k = k+1;
    end % if
end % for

number_of_nodes = k; % number of nodes in each cross-section
X = zeros(number_of_nodes,1);
Y = zeros(number_of_nodes,1);
Z = zeros(number_of_nodes,1);
UX = zeros(number_of_nodes,1);
UY = zeros(number_of_nodes,1);
UZ = zeros(number_of_nodes,1);

% assigning the known data to the cross-sectional variables
k = 0;
for i = 1:length(node_coord_displ)
    if node_coord_displ(i,2) == closestX
        k = k+1;
        X(k) = node_coord_displ(i,2);
        Y(k) = node_coord_displ(i,3);
        Z(k) = node_coord_displ(i,4);
        UX(k) = node_coord_displ(i,5);
        UY(k) = node_coord_displ(i,6);
        UZ(k) = node_coord_displ(i,7);
    end % if
end % for

lb = [-length/20,-length/20,-length/2]; % lower bound
ub = [length/20,length/20,length/2]; % upper bound
options = optimset('Display','off');
[x,resnorm] = lsqnonlin(@rigid_body_minimization,x0,lb,ub,options,Y,Z,UY,UZ,
    number_of_nodes);

f = rigid_body_minimization(x,Y,Z,UY,UZ,number_of_nodes);
min_function(j) = norm(f);

% calculating the average axial displacement, ignoring bending effects
SumUX = 0;
for k = 1:number_of_nodes
    SumUX = SumUX + UX(k);
end % for

```

```

U1(j) = SumUX/number_of_nodes;

U2(j) = x(1);
U3(j) = x(2);
theta(j) = x(3);

% solved values at current cross-section are used as the initial guess values for the
% next cross-section
x0 = x;

end % for

% output
U1 = flipud(U1')
U2 = flipud(U2')
U3 = flipud(U3')
theta = flipud(theta'*180/pi)
min_function;

end % function

```

### C.2.3 Minimization Function File: rigid\_body\_minimization.m

```

function f = rigid_body_minimization(x,Y,Z,UY,UZ,number_of_nodes)
k = 1:number_of_nodes;
f1 = UY(k)-x(1)-Y(k)*(cos(x(3))-1)+Z(k)*sin(x(3));
f2 = UZ(k)-x(2)-Z(k)*(cos(x(3))-1)-Y(k)*sin(x(3));
f = [f1;f2];
end % function

```